

FATIGUE AND STATIC BEHAVIOR OF CURVED COMPOSITE LAMINATES

A THESIS SUBMITTED TO
THE GRADUATE SCHOOL OF NATURAL AND APPLIED SCIENCES
OF
MIDDLE EAST TECHNICAL UNIVERSITY

BY

BURCU TAŞDEMİR

IN PARTIAL FULFILLMENT OF THE REQUIREMENTS
FOR
THE DEGREE OF MASTER OF SCIENCE
IN
AEROSPACE ENGINEERING

MAY 2018

Approval of the thesis:

**FATIGUE AND STATIC BEHAVIOR OF CURVED COMPOSITE
LAMINATES**

Submitted by **BURCU TAŞDEMİR** in partial fulfillment of the requirements for the degree of **Master of Science in Aerospace Engineering Department, Middle East Technical University** by,

Prof. Dr. Halil Kalıpçilar
Dean, Graduate School of **Natural and Applied Sciences**

Prof. Dr. Ozan Tekinalp
Head of Department, **Aerospace Engineering**

Assoc. Prof. Dr. Demirkhan Çöker
Supervisor, **Aerospace Engineering**

Examining Committee Members:

Prof. Dr. Altan Kayran
Aerospace Engineering Dept., METU

Assoc. Prof. Dr. Demirkhan Çöker
Aerospace Engineering Dept., METU

Prof. Dr. Kemal Levend Parnas
Mechanical Engineering Dept., TEDU

Prof. Dr. Mehmet Ali Güler
Mechanical Engineering Dept., TOBB ETU

Assoc. Prof. Dr. Ercan Gürses
Aerospace Engineering Dept., METU

Date: 21.05.2018

I hereby declare that all information in this document has been obtained and presented in accordance with academic rules and ethical conduct. I also declare that, as required by these rules and conduct, I have fully cited and referenced all material and results that are not original to this work.

Name, Last name : Burcu Taşdemir

Signature :

ABSTRACT

FATIGUE AND STATIC BEHAVIOR OF CURVED COMPOSITE LAMINATES

Taşdemir, Burcu

MSc., Department of Aerospace Engineering
Supervisor: Assoc. Prof. Dr. Demirkhan Çöker

May 2018, 136 pages

By virtue of the fact that curved composite laminates which are utilized as load carrying subcomponents in aircraft and wind turbine structures are subjected to cyclic loading during their operating time, it is crucial to understand fatigue failure mechanisms at least as much as static failure mechanisms. With the intention of understanding fatigue failure mechanisms and thus improving fatigue life of structures, these curved laminates are investigated experimentally under static and fatigue loadings. The failure mechanisms observed in the tests are supported by analytical and numerical methods.

CFRP laminates with four different ply architectures (UD, cross-ply with two different thicknesses and fabric) are examined. A new test fixture is designed to apply moment/axial combined loading to curved specimens properly. Static and fatigue experiments are conducted using servo-hydraulic testing machine and in-situ photographs are taken. In addition, DIC method is used to obtain strain distribution in the curved region just before the failure. The stress state at the curved region for each specimen configuration is analytically calculated using the multilayer curved beam solution.

In the experimental results of UD and fabric laminates, it is observed that both static and fatigue failures initiate at roughly the maximum radial stress location (approximately 35% of the thickness from inner radius). For UD laminates, there is no visible difference between the failure mechanisms under static and fatigue loadings. For fabric laminates, fatigue failure is observed to occur as a single major crack at the maximum radial stress location just as in UD laminates, whereas static failure is observed to occur as multiple diffusive cracks at the maximum radial stress location.

In contrast to UD and fabric laminates, different failure locations and mechanisms are observed in the fatigue and static experiments of cross-ply specimens. Fatigue failure is observed to form at the maximum radial stress location whereas the static failure is observed to form in the region where the combined radial, tangential and shear stresses attain a maximum value, in the form of Tsai-Wu failure criterion. For fatigue failure, micro-cracks existing in the maximum radial stress location grow more rapidly under cyclic loading compared to cracks in other regions and coalesce into one major matrix crack which reaches the 0/90 interface gradually and continues to propagate as a delamination. As for the static failure, failure initiates as a matrix crack in the group of 90° layers and jumps to the upper 0/90 interface by an abrupt 40-50° angle and propagates as a delamination. Against the common belief in the literature, according to our observations, we conclude that static and fatigue failure mechanisms are not always the same.

Keywords: composite, fatigue, curved, delamination, failure

ÖZ

BÜKÜMLÜ KOMPOZİT LAMİNATLARIN YORULMA VE STATİK DAVRANIŞI

Taşdemir, Burcu

Yüksek Lisans, Havacılık ve Uzay Mühendisliği Bölümü

Tez Yöneticisi: Doç. Dr. Demirkan Çöker

Mayıs 2018, 136 sayfa

Hava taşıtları ve rüzgar türbin yapılarında yük taşıyıcı alt komponent olarak kullanılan bükümlü kompozit laminatların çalışma süreleri boyunca periyodik yüklemeye maruz kalmaları sebebiyle yorulmadan kaynaklı kırılma mekanizmalarının en az statik kırılma mekanizmaları kadar iyi anlaşılması önemlidir. Yorulmadan kaynaklı kırılma mekanizmalarının anlaşılması ve bu sayede yapıların yorulma ömrlerinin arttırılması amacıyla bu bükümlü kompozit laminatlar statik ve yorulma yüklemeleri altında deneysel olarak incelenmiştir. Testlerde gözlemlenen kırılma mekanizmaları analitik ve sayısal analiz metodlarıyla desteklenmiştir.

Dört farklı katman yapısına sahip (Tek yönlü, iki farklı kalınlıkta çapraz serimli ve örgü kumaş) karbon fiber takviyeli polimer laminatlar test edilmiştir. Moment/eksenel kombine yüklemesini bükümlü numunelere tam anlamıyla uygulayabilmek için yeni bir bağlantı düzeneği tasarlanmıştır. Statik ve yorulma deneyleri servo-hidrolik test makinası kullanılarak gerçekleştirılmıştır ve deney esnasında gerçek zamanlı fotoğraflar çekilmiştir. Ek olarak, kırılmanın hemen öncesinde bükümlü bölgedeki gerinim dağılımını elde etmek için Dijital Görüntü Korelasyon methodu kullanılmıştır. Her bir numune konfigürasyonu için bükümlü bölgedeki gerilim durumu çok katmanlı bükümlü kiriş çözümü kullanılarak analitik olarak hesaplanmıştır.

Tek yönlü ve örgü kumaş laminatların deneysel sonuçlarında, statik ve yorulmadan kaynaklı kırılmaların her ikisinin de kabaca maksimum radyal gerilim lokasyonundan (iç yarıçapтан itibaren kalınlığın yaklaşık % 35'i) başladığı gözlemlenmiştir. Tek yönlü laminatlar için statik ve yorulma yüklemeleri altında kırılma mekanizmalarında gözle görülür fark bulunmamaktadır. Örgü kumaş laminatlar için yorulmadan kaynaklı kırılmanın tipki tek yönlü laminatlarda olduğu gibi maksimum radyal gerilim lokasyonunda tek bir kırık şeklindeoluştuğu gözlenirken statik yüklemeden kaynaklı kırılmanın çoklu dağınık çatlak şeklinde meydana geldiği gözlemlenmiştir.

Tek yönlü ve kumaş laminatların aksine çapraz serimli laminatların yorulma ve statik deneylerinde farklı kırılma lokasyonları ve mekanizmaları gözlemlenmiştir. Yorulmadan kaynaklı kırılmanın maksimum radyal gerilim lokasyonunda oluştuğu gözlenirken statik yüklemeden kaynaklı kırılmanın radyal, teğetsel ve kesme gerilmelerinin kombinasyonlarının Tsai-Wu kırılma kriterine göre maksimum değere ulaşlığı bölgede oluştuğu gözlemlenmiştir. Yorulmadan kaynaklı kırılma olayında maksimum radyal gerilim lokasyonunda bulunan mikro çatlaklar, diğer bölgelerde bulunan çatlaklara göre tekrarlı yük altında daha hızlı büyür ve 0/90 ara yüzüne kademeli olarak ulaşan bir büyük matris çatlağına dönüşerek delaminasyon olarak yayılmaya devam eder. Statik yüklemeden kaynaklı kırılmada ise, kırılma 90° dizilime sahip tabaka grubunda bir matris çatlağı olarak başlar ve 40-50°lik keskin açıyla bir üst 0/90 ara yüzüne atlayarak delaminasyon olarak yayılmaya devam eder. Gözlemlerimiz doğrultusunda, literatürdeki genel kanının aksine statik ve yorulmadan kaynaklı kırılma mekanizmalarının her zaman aynı olmadığı sonucuna vardık.

Anahtar Kelimeler: kompozit, yorulma, bükümlü, delaminasyon, kırılma

To My Family...

ACKNOWLEDGMENTS

I would first like to express my deepest gratitude to my advisor, Assoc. Prof. Dr. Demirkan Çöker, for his guidance during two years of undergraduate research period and three years of M.Sc. study.

I would like to acknowledge Assoc. Prof. Dr. Oğuz Uzol for offering me peaceful working area and opportunity to use RUZGEM (METU Center for Wind Energy) facilities. I would also like to thank Prof. Dr. Altan Kayran for his support in RUZGEM structural labs and lectures that I enjoyed to attend. I would also like to acknowledge to Assoc. Prof. Dr. Ercan Gürses for all his supports and advices. I would also like to thank to Prof. Dr. Levend Parnas and Prof. Dr. Mehmet Ali Güler for their precious comments in my thesis committee.

I would like to thank best colleagues ever Miraç Onur Bozkurt and Ahmet Çevik for their endless support and friendship. Also thanks to rest of the group, Can Muyan, Aydın Amireghbali, Touraj Farsadi and Tuğrul Akpolat.

My special thanks waiting for the ladies growing with me, my honey Elif Alavanda and my tiny Buket İkizoğlu for 14 years of endless support.

Finally, I must express my very profound gratitude to my family. My daddy, Adnan Taşdemir, you are the real hero of the world. You are the inspiration of all my success. Mommy, Menşure Taşdemir, you are the reason of goodness inside me. Without you, I could have not succeeded any one of these. And my little princess Büşra Taşdemir, thanks for being with me all the time. And my friend, colleague and everything, Tamer Tahir Ata, thank you for endless support and everlasting love for all the time.

TABLE OF CONTENTS

ABSTRACT	v
ÖZ	vii
ACKNOWLEDGMENTS	x
TABLE OF CONTENTS	xi
LIST OF TABLES	xiv
LIST OF FIGURES	xv
LIST OF SYMBOLS	xxi
LIST OF ABBREVIATIONS	xxiv
CHAPTERS	
1 INTRODUCTION	1
2 LITERATURE REVIEW.....	9
3 METHOD.....	21
3.1 Experimental Method	21
3.1.1 Material	21
3.1.2 Manufacturing Process	23
3.1.3 Geometry and Laminate Properties	25
3.1.4 Specimen Preparation.....	35
3.1.5 Fixture and Experimental Setup	37
3.1.6 Experimental Procedure	41
3.1.7 Digital Image Correlation Method	43
3.2 Analytical Method	44

3.2.1	Calculation of Stresses due to Mechanical Load.....	44
3.2.2	Calculation of Stresses due to Thermal Load.....	47
3.3	Finite Element Method	48
4	UD LAMINATES	51
4.1	Experimental Results of UD Curved Laminates.....	51
4.1.1	Static Tensile Tests of UD Curved Laminates	51
4.1.2	Fatigue Tests of UD Curved Laminates	56
4.2	Analytical Results of UD Curved Laminates.....	60
4.3	Finite Element Results of UD Curved Laminates.....	62
5	CROSS-PLY LAMINATES	65
5.1	Experimental Results of Cross-Ply Curved Laminates.....	65
5.1.1	Static Tensile Tests of Cross-Ply Curved Laminates	65
5.1.2	Fatigue Tests of Cross-Ply Curved Laminates	79
5.2	Analytical Results of Cross-Ply Curved Laminates.....	87
5.2.1	Thin Cross-Ply Curved Laminates	87
5.2.2	Thick Cross-Ply Curved Laminates.....	90
5.3	Finite Element Results of Cross-Ply Curved Laminates.....	93
5.3.1	Thin Cross-Ply Curved Laminates	93
5.3.2	Thick Cross-Ply Curved Laminates.....	95
6	FABRIC LAMINATES	97
6.1	Experimental Results of Fabric Curved Laminates	97
6.1.1	Static Tensile Tests of Fabric Curved Laminates	97
6.1.2	Fatigue Tests of Fabric Curved Laminates.....	100
6.2	Analytical Results of Fabric Curved Laminates	102
6.3	Finite Element Results of Fabric Curved Laminates	104

7 DISCUSSION	107
7.1 Damage Mechanisms in UD and Fabric Curved Composite Laminates under Static and Fatigue Loading	107
7.2 Damage Mechanisms in Cross-ply Curved Composite Laminates under Static and Fatigue Loading.....	110
8 CONCLUSIONS.....	119
8.1 Conclusions on Damage Mechanisms in UD and Fabric Curved Composite Laminates under Static and Fatigue Loading.....	119
8.2 Conclusions on Damage Mechanisms in Cross-ply Curved Composite Laminates under Static and Fatigue Loading.....	119
REFERENCES.....	121
APPENDICES	
A. BEAM BENDING FEA.....	127
B. TSAI-WU FAILURE CRITERIA	131
C. TECHNICAL DRAWING OF THE TEST FIXTURE.....	132
D. USED MACHINES AND FUNCTIONS	133

LIST OF TABLES

Table 1. Lamina properties [44]-[46].....	22
Table 2. Dimensions of the specimens.....	26
Table 3. Calculated laminate properties.....	34
Table 4. Summary of the experiments.	42
Table 5. Summary table for static experiments of UD specimens.	54
Table 6. Summary table for static experiments of thin cross-ply specimens.	67
Table 7. Summary table for static experiments of thick cross-ply specimens.	75
Table 8. Summary table for static experiments of fabric specimens.	99

LIST OF FIGURES

Figure 1. Change in material usage percentage in Boeing airplanes [9]......	3
Figure 2. Size comparison of 5MW turbine blade and Airbus A340 [10]......	3
Figure 3. Usage schematic of curved laminated composites in wind turbine blades and aircraft wings [14]	4
Figure 4. Subcomponents of the wing structure [15]......	5
Figure 5. Main elements of a wind turbine blade [14]......	5
Figure 6. Damage types of composite laminate [17].	6
Figure 7. Comparison of fatigue strength of boron, graphite and glass fibers [18].	10
Figure 8. Stress strain curve of (a) metal matrix, (b) polymer matrix composites [20].	10
Figure 9. Stress strain curve of (a) low stiffness (glass) fibers, (b) high stiffness (graphite) fibers [5].	11
Figure 10. Change of strength with fiber volume fraction [20].	12
Figure 11. Comparison of delamination initiation and propagation for numerical and experimental results [26]......	13
Figure 12. (a) Radial (b) tangential (c) shear stress through the thickness [29].	14
Figure 13. Prediction of interlaminar tension failure between 0° plies [29]......	15
Figure 14. (a)Correction applied to ASTM standard, (b) radial stress distribution for corrected and uncorrected calculations [31].	16
Figure 15. (a) Delamination coupon, (b) flatwise tension test, (c) diametrical compression disk specimen [32] and (d) curved beam test specimen [36]......	17
Figure 16. Curved beam test specimen types [32], [36] - [38].	17
Figure 17. FEA bending and radial stress distributions of specimen [90/0 ₃ /90 ₂ /0 ₃ /90] at θ=25° [16].	18
Figure 18. (a) Moment, (b) end load case [36].	18

Figure 19. Loading mechanism of (a) Martin and Jackson [40] (b) Shivakumar et al. [38].	19
Figure 20. Schematic of test configurations (a) 4-pt bending, (b) hinged loading Mechanism (HLM) and (c) comparison of strengths for the two test methods [41].	19
Figure 21. (a) Interlaminar stresses (b) tangential stress through the thickness and (c) radial stress around curved region [42].	20
Figure 22. Unidirectional and woven laminas [43].	21
Figure 23: Manufacturing process.....	24
Figure 24. Geometry of the specimen.	25
Figure 25. Stacking details of the UD [0]30 specimen.....	27
Figure 26. Stacking details of the thick cross-ply [0 ₃ /90 ₃ /0 ₃ /90 ₃ /0 ₃] _s specimen.	27
Figure 27. Stacking details of the thin cross-ply [0 ₃ /90 ₃ /0 ₃] _s specimen.....	28
Figure 28. Stacking details of the fabric [(45/0) ₇ ,45/45/0/45] specimen.	28
Figure 29. Stacking sequence of specimens in micrographs.....	34
Figure 30. Holes on the arms.	35
Figure 31. Polishing machine.....	35
Figure 32. Digital microscope.....	36
Figure 33. (a) Unpainted, (b) painted and (c) painted close-up photograph of the specimen.....	36
Figure 34. Free body diagram of the specimen.	37
Figure 35. Loading fixture (a) photograph and (b) CAD drawing.....	38
Figure 36. Comparison of results for old fixture [48] and the new fixture.	39
Figure 37. Experimental set-up.	40
Figure 38. Undeformed and deformed images [49].	43
Figure 39. FEM geometry visualization.....	48
Figure 40. Load application and boundary condition.	49
Figure 41. Mesh visualization on FEM.	50
Figure 42. Difference between the analyses with 2 and 4 elements for each ply.	50
Figure 43. (a) Load-displacement curves, pictures of the specimens (b) before failure and (c) after failure.	52

Figure 44. Crack occurred at mounting the specimen.....	53
Figure 45. Change of Tresca strain distribution in the specimen (0t5s2) with time up to failure	55
Figure 46. Representation of change in Tresca strain in the specimen (0t5s2) on load-displacement curve.....	55
Figure 47. Tresca strain distribution just before the failure and its representation on the specimen picture just after the failure.	56
Figure 48. (a) Load-displacement curves, (b) load-cycle-displacement curves and (c) pictures of the specimens after the failure.....	57
Figure 49. Maximum and minimum loads during the fatigue loading and the differences for specimen 0t5s3.....	58
Figure 50. Change in stiffness with cycles.....	58
Figure 51. Load and temperature change with time for the specimen 0t5s5 and the close-up view.	59
Figure 52. Representation of directions and sections used for stress distribution calculations on [0]30 curved specimen.....	60
Figure 53. Radial, tangential and shear stress distributions through the thickness direction.....	61
Figure 54. Radial, tangential and shear stress distributions on the curved region respectively for [0]30 UD lay-up.	62
Figure 55. Comparison of FEA and analytical solution for radial and tangential stress distributions through the thickness at the center of the curve for [0]30 UD lay-up....	63
Figure 56. Load-displacement graph for experiments and FEA.	63
Figure 57. (a) Load-displacement curves, pictures of the specimens (b) before failure and (c) after failure.....	66
Figure 58. Representation of examination sections on the curved region.	68
Figure 59. Detailed examination of the failure on micrographs for specimen 90t3s4 tested under static loading.....	69
Figure 60. Representation of change in Tresca strain in the specimen (90t3s2) on the load-displacement curve.....	70

Figure 61. Change of Tresca strain distribution in the specimen (90t3s2) with time up to failure.....	71
Figure 62. Tresca strain distribution just before the failure and its representation on the specimen image just after the failure.....	71
Figure 63. Close-up views of Tresca strain field and failure pattern of the specimen.	72
Figure 64. Detailed examination of the failure on micrographs of the thin curved cross-ply specimen tested under static loading using DIC method.	73
Figure 65. (a) Load-displacement curves, pictures of the specimens (b) before failure and (c) after failure.....	74
Figure 66. Representation of change in Tresca strain in the specimen (90t5s3) on the load-displacement curve.....	75
Figure 67. Change of Tresca strain distribution in the specimen (90t5s3) with time up to failure.....	76
Figure 68. Tresca strain distribution just before the failure and its representation on the specimen picture just after the failure.	77
Figure 69. Closer look to Tresca strain field and failure pattern of the specimen.	77
Figure 70. Detailed examination of the failure on micrographs of the thick curved cross-ply specimen tested under static loading and using DIC method.	78
Figure 71. (a) Load-displacement curves, (b) load-cycle-displacement curves and (c) pictures of the specimens after the failure.....	80
Figure 72. Maximum and minimum loads during the fatigue loading and the differences (stiffness) for specimen 90t3s8.....	81
Figure 73. Change in stiffness with cycles.....	81
Figure 74. Load-displacement change in load and temperature for specimen 90t3s10.	82
Figure 75. Maximum and minimum experimental loads and the thermal effect free loads during the fatigue loading and the difference graph for specimen 90t3s10.....	82
Figure 76. Detailed examination of the failure on micrographs of specimen 90t3s5 tested under fatigue loading.	83

Figure 77. (a) Load-displacement curves, (b) load-cycle-displacement curves and (c) images of the specimens after the failure.....	85
Figure 78. Maximum and minimum loads during the fatigue loading and the differences for specimen 90t5s7 and 90t5s10.....	86
Figure 79. Change in stiffness with cycles.....	86
Figure 80. Representation of directions and sections used for stress distribution calculations on thin cross-ply curved specimen.....	87
Figure 81. Radial, tangential and shear stress distribution through the curve direction.	88
Figure 82. Radial, tangential and shear stress distributions through the thickness direction.....	89
Figure 83. Representation of directions and sections used for stress distribution calculations on thick cross-ply curved specimen.....	90
Figure 84. Radial, tangential and shear stress distributions through the curve direction at 4 th , 5 th , 6 th and 10 th , 11 th , 12 th layers.....	91
Figure 85. Radial, tangential and shear stress distributions through the thickness direction.....	92
Figure 86. Radial, tangential and shear stress distributions on the curved region respectively for thin cross-ply lay-up.....	93
Figure 87. Comparison of FEA and analytical solution for radial and tangential stress distributions through the thickness at the center of the curve for thin cross-ply lay-up.	94
Figure 88. Load-displacement curve for thin cross-ply lay-up.....	94
Figure 89. Radial, tangential and shear stress distributions on the curved region respectively for thick cross-ply lay-up.....	95
Figure 90. Comparison of FEA and analytical solution for radial and tangential stress distributions through the thickness at the center of the curve for thick cross-ply lay-up.	96
Figure 91. Load-displacement curve for thick cross-ply lay-up.....	96
Figure 92. (a) Load-displacement curves, pictures of the specimens (b) before failure and (c) after failure.....	98

Figure 93. Tresca strain distribution just before the failure and its representation on the specimen picture just after the failure.....	100
Figure 94. (a) Load-displacement curves, (b) load-cycle-displacement curves and (c) pictures of the specimens after the failure.....	101
Figure 95. Change in stiffness with cycles.....	101
Figure 96. Representation of directions and sections used for stress distribution calculations on fabric curved specimen.	102
Figure 97. Radial, tangential and shear stress distributions through the thickness direction.....	103
Figure 98. Radial, tangential and shear stress distributions on the curved region respectively for fabric lay-up.	104
Figure 99. Comparison of FEA and analytical solution for radial and tangential stress distributions through the thickness at the center of the curve for fabric lay-up.....	105
Figure 100. Load-displacement curve for fabric lay-up.....	105
Figure 101. (a) Static and (b) fatigue failure images for [0] ₃₀ specimens.....	107
Figure 102. Radial, tangential and shear stress distributions through the thickness direction.....	108
Figure 103. (a) Static and (b) fatigue failure images for fabric specimens.....	109
Figure 104. Radial, tangential and shear stress distributions through the thickness direction.....	110
Figure 105. (a) Static and (b) fatigue failure differences for thin specimens.....	111
Figure 106. Radial, tangential and shear stress distributions through the thickness direction.....	112
Figure 107. Failure index distribution through the thickness using Tsai-Wu failure criterion.	112
Figure 108. (a) Static and (b) fatigue failure differences for thick specimens.....	113
Figure 109. Radial, tangential and shear stress distributions through the thickness direction in thick composite at 800 N.	114
Figure 110. Failure index distribution through the thickness for thick specimen using Tsai-Wu failure criterion.....	115
Figure 111. Defect sensitivity of fatigue experiments by micrographs.	116

LIST OF SYMBOLS

D	Diameter
E₁₁, E₂₂, E₃₃	Elastic modulus in material axis
E_r	Modulus of elasticity in radial direction
E_θ	Modulus of elasticity in tangential (hoop) direction
E_{xx}, E_{yy}, E_{zz}	Elastic modulus in problem axis
F	Airy stress function
G₁₂, G₁₃, G₂₃	Shear modulus in material axis
G_{rθ}	Radial shear modulus
G_{xy}, G_{xz}, G_{yz}	Shear modulus in problem axis
h_k	Thickness of the k th layer
L	Distance from load point to curve region
L₁	Arm length - 1
L₂	Arm length - 2
N_x, N_y, N_{xy}	Resultant laminate forces
M	Moment load
M_x, M_y, M_{xy}	Resultant laminate moments
P	End force
P_c	Critical end force
P_{max}	Maximum end force
P_r	Residual end force
Q	Stiffness matrix of lamina
r	Radius
R_i	Inner radius
R_m	Mean radius
R_o	Outer radius

S₁₁	Tangential stress for 2D FEA
S₂₂	Radial stress for 2D FEA
S₁₂	Shear stress for 2D FEA
t	Thickness
t_{ply}	Ply thickness
w	Width of the specimen
α_x, α_y, α_{xy}	Thermal expansion coefficients
β	Anisotropic parameter for end force case
δ_c	Critical displacement corresponding to critical end force (P _c)
δ_r	Residual displacement
ε	Strain
ε_x⁰, ε_y⁰, γ_{xy}⁰	Middle surface strains
ε_{xx}, ε_{xy}, ε_{xz}	Normal strain in x-axis, shear strain in y-axis, shear strain in z axis on yz-plane, respectively
ε_{yy}, ε_{yx}, ε_{yz}	Normal strain in y-axis, shear strain in x-axis, shear strain in z axis on xz-plane, respectively
ε_{zz}, ε_{zy}, ε<subzx< sub=""></subzx<>	Normal strain in z-axis, shear strain in y-axis, shear strain in x axis on xy-plane, respectively
ε_x^T, ε_y^T, γ_{xy}^T	Thermal strains
k	Anisotropic parameter for moment case
θ	Tangential coordinate
σ	Stress
σ₁₁	Normal stress in fiber direction
σ₂₂	Normal stress in transverse fiber direction
σ₃₃	Normal stress in thickness direction
σ_r	Radial stress
σ_θ	Tangential (hoop) stress
τ_{rθ}	Shear stress

$\sigma_{xx}, \sigma_{xy}, \sigma_{xz}$	Normal stress in x-axis, shear stress in y-axis, shear stress in z axis on yz-plane, respectively
$\sigma_{yy}, \sigma_{yx}, \sigma_{yz}$	Normal stress in y-axis, shear stress in x-axis, shear stress in z axis on xz-plane, respectively
$\sigma_{zz}, \sigma_{zy}, \sigma_{zx}$	Normal stress in z-axis, shear stress in y-axis, shear stress in x axis on xy-plane, respectively
v_{13}	Poisson's ratio for transverse strain in the 3-direction when stressed in the 1-direction
v_{12}	Poisson's ratio for transverse strain in the 2-direction when stressed in the 1-direction
v_{23}	Poisson's ratio for transverse strain in the 3-direction when stressed in the 2-direction
$v_{\theta r}$	Poisson's ratio for transverse strain in the radial-direction when stressed in the tangential (hoop)-direction
$u_r, u_\theta,$	Displacements in radial and tangential (hoop) directions, respectively
K_x, K_y, K_{xy}	Middle surface curvatures
ρ	Density
ω	Angle defining direction of end load
ω_0	Bending displacement

LIST OF ABBREVIATIONS

2D	Two-Dimensional
3D	Three-Dimensional
5 HS	Five Harness Satin
ASTM	American Society for Testing and Materials
CAD	Computer Aided Drawing
CFRP	Carbon Fiber Reinforced Polymer
DCB	Double Cantilever Beam
DTW	Digital Torque Wrench
DIC	Digital Image Correlation
FEA	Finite Element Analysis
FEM	Finite Element Method
FI	Failure Index
FPS	Frame per Second
GFRP	Glass Fiber Reinforced Polymer
HLM	Hinge Loading Mechanism
ILTS	Interlaminar Tensile Strength
LCD	Liquid Crystal Display
MP	Megapixel
SN	Stress versus the number of cycles
UD	Unidirectional Ply

CHAPTER 1

INTRODUCTION

An inevitable circumstance for structures is the applied load and the corresponding deformation which leads to generation of stresses on the load carrying members. The main structure is exposed to a loading according to its area of utilization. Load carrying members are designed to withstand maximum loading condition and corresponding stresses. Material selection and geometrical properties are the main design concerns. These designed members generally do not experience a loading as large as ultimate tensile strength of the material. Therefore, a failure due to static loading is not very common for a well-designed structure without any initial damage. However, repeated loads may lead to failure before reaching the ultimate strength of the material. This mechanism of failure is called fatigue failure and represented by a loss of resistance with cycles and time. Fatigue failure is very common, critical and hazardous failure type for structures. Several researches show that approximately 60% or 80% of the structural failures are caused by fatigue mechanisms [1], [2].

Fatigue failure is caused by cyclic loading leads to a stress distribution whose maximum is lower than the ultimate strength of the material. While a low amount of load for a single application does not affect the structure, same amount of load may lead to failure if it is repeated. Fatigue failure basically starts with initiation of microscopic cracking and followed by propagation of the microscopic cracks to macroscopic ones with each load cycle for unwelded metals and alloys. As the crack grows, impaired area to the cross section decreases and this leads to failure at an instant. For the case of welded components, existing impurities cause initial cracks and leads to premature fatigue deformation and corresponding fatigue failure [3], [4].

For composite materials fatigue failure mechanism is more complicated than metallic fatigue failure [5]. Composite materials are anisotropic and inhomogeneous while metals are isotropic and homogeneous. This effects the behavior of fatigue failure of the material. Under cyclic loading, composite materials accumulate damage and failure which may not be caused by only a single macroscopic crack. Microstructural mechanisms of damage accumulation such as fiber breakage, matrix cracking, delamination and interfacial debonding may happen independently or in tandem [6].

Generally, aerospace and wind turbine structures operate under specific loading conditions. These loadings are repeated continuously on the structures during whole operating times. Fatigue behavior of these structures are crucial for durability of the design. Usage of metallic components which have well defined fatigue behavior have been decreased for aerospace and wind turbine structures by reason of their low specific stiffness and strength compared to composite materials. Since reduction of mass is the most important requirement for both aerospace and wind turbine industries, composite materials which provide high strength, high stiffness with low density [7] are generally used.

For complex designs of the aircraft structures, necessity of strong and stiff reinforcement, like carbon fiber with high performance resin, is supplied using carbon fiber reinforced polymer, CFRP, composites. Rising generation commercial aircraft have approximately at least 33% of the structural weight of the aircraft inbuilt advanced CFRP composites [8]. Usage of composite materials in aircraft is increasing day by day. In Figure 1, the increase in proportion of composite parts in airplanes of Boeing given as an example of the rise in utilization of composite materials in aircraft. Within the 40-year process, usage of composite materials visibly increases from 1% to 50%.

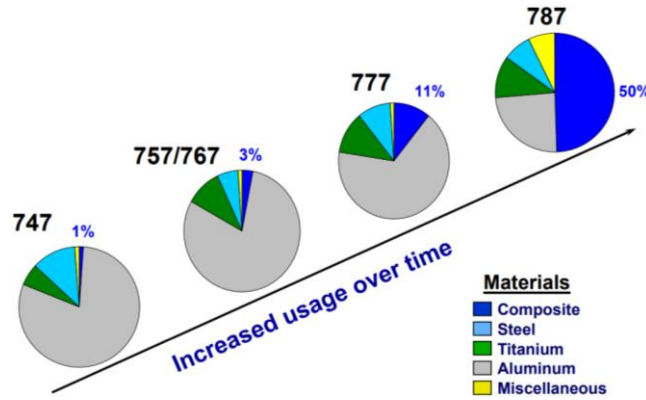


Figure 1. Change in material usage percentage in Boeing airplanes [9].

Most of wind turbine blades are made of glass fiber reinforced polymer, GFRP, composite. Wind energy industry is growing very fast and for higher efficiency, size and capacity of wind turbine blades are also enlarged very rapidly [10]. To gain an impression about the size of mentioned huge wind turbine blades, comparison photograph of a 5MW wind turbine blade and Airbus A340 commercial airplane is given in Figure 2. Increase in size of the blades leads to more deflection at the tip and increase in weight. This situation creates the necessity in pursuit of new materials with stiffer and lighter reinforcement like CFRP [11]. Investigation of CFRP composite material usage for wind turbine blades have recently started [12], [13]. Griffin investigates the performance tradeoffs for carbon fiber in wind turbine blades.



Figure 2. Size comparison of 5MW turbine blade and Airbus A340 [10].

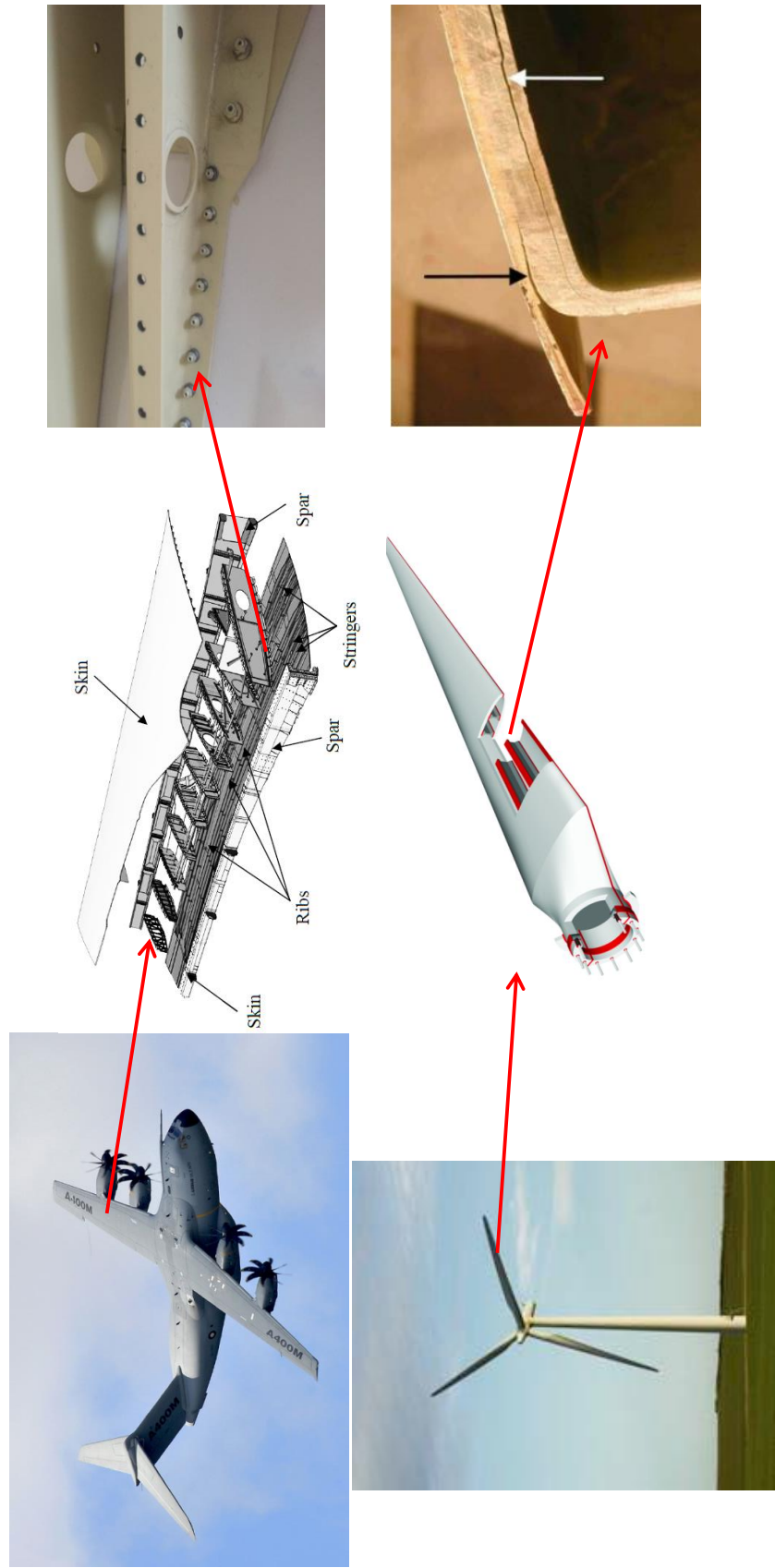


Figure 3. Usage schematic of curved laminated composites in wind turbine blades and aircraft wings [14]

Most of load carrying sub structures contain angle brackets or frames which have curved parts. Increase in usage of composite material in structures leads to increase in usage of composite material for these curved substructures. As seen in Figure 3, curved composite structures are commonly used in ribs and spars of airplane wings and wind turbine blades. Spars are the principal structural members of a wing and support all distributed loads. Skin attached to the wing structure and supports part of loads applies on wing structure during operation and transfers the stresses to the ribs. The ribs transfer the stresses to the spars [15]. Subcomponents of the wing structure are as shown in Figure 4 and main elements of a wind turbine blade are as shown in Figure 5.

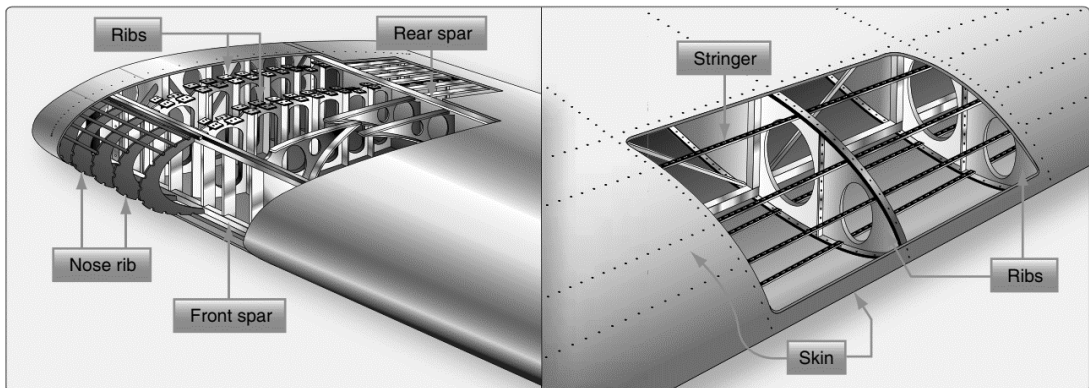


Figure 4. Subcomponents of the wing structure [15].

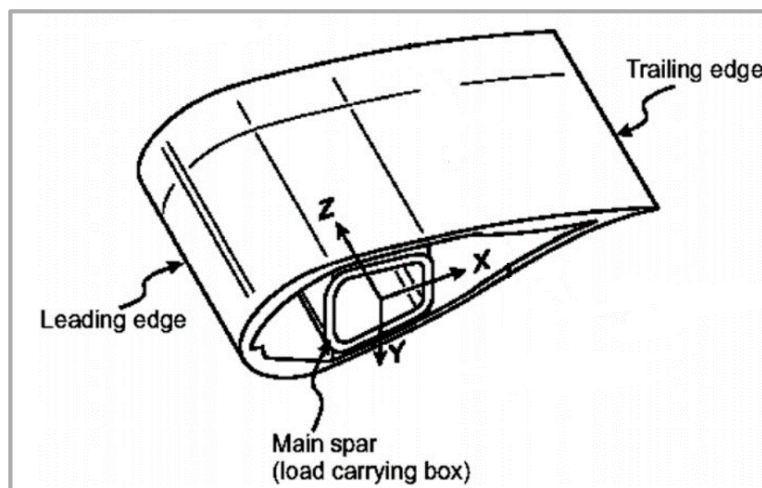


Figure 5. Main elements of a wind turbine blade [14].

Ribs and spars of the airplane wings and wind turbine blades undergo cyclic loading during their operating time. Fatigue behavior of these composite components is a vital phenomenon for a safe design and durability of the structure. One of the main requirements of a safe design is gaining detailed knowledge about failure mechanism of used composite material. Failure analysis of composite materials is complicated by virtue of their nonhomogeneous and orthotropic behaviors [16]. Composite fatigue is considered very complicated but if it is examined systematically by changing every parameter and obtaining knowledge about each one of the parameters, it is possible to understand the fatigue behavior of composite materials.

Composite laminates experience failure types different from metals such as delamination, fiber breakage, debonding and matrix cracking as seen in Figure 6. Dominant failure mechanisms which is encountered in curved composite laminates are delamination and matrix cracking. Matrix cracking is the crack which initiates and propagates in the matrix (intralaminar cracks) and delamination is the crack which propagates between the layers (interlaminar cracks). Due to dominant opening stresses in curved region, delamination is inevitable most dominant failure mechanism. Matrix cracking is observed only for cross-ply laminates from side view of the specimens. Fiber breakage is never observed in curved laminates due to very high strength in the fiber direction in comparison with the out of plane transverse direction.

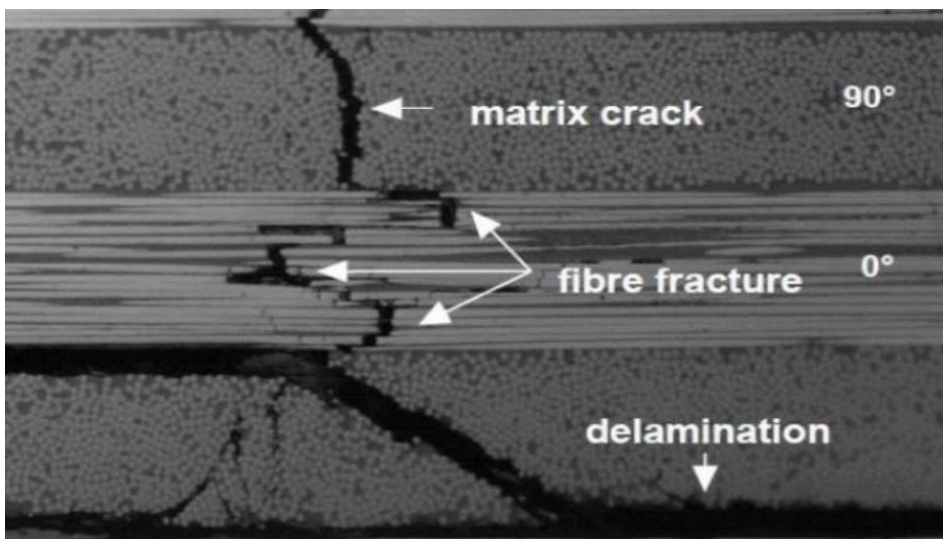


Figure 6. Damage types of composite laminate [17].

In the last few decades, extensive researches have been conducted on the static failure of curved laminated beams, however, study of the fatigue behavior is lacking. In this thesis, investigation of the fatigue and static behavior of curved composite laminates that are commonly used in ribs, shear webs and spar flanges of airplane wings and wind turbine blades due to their light weight and strength advantages, is carried out. In order to clarify fatigue and static failure mechanisms seen in curved laminated composites, combined moment/axial loading experiments are conducted for four different specimen configurations (UD, cross-ply with two different thicknesses and fabric). Observed failure mechanisms in the experiments are explained by analytical and numerical methods. Well understood failure mechanisms under fatigue loading may provide reinforcement methods to increase fatigue life and durability of these structures.

CHAPTER 2

LITERATURE REVIEW

Survey of the literature starts with the fatigue behavior of composite laminates and then, specifically focuses on fatigue behavior of curved composite laminates. The review is continued with static behavior of curved composite laminates and the analytical solution methods. In the literature, there are very valuable static studies on curved laminates and fatigue behavior of flat composite laminates. However, there are very few studies on fatigue behavior of curved composite laminates.

Fatigue of Composite Laminates

In 1960s, primary studies on fatigue behavior and life prediction of laminated composites have been started [18], [19]. Glass fiber reinforced polymer composite materials are tested under fatigue loading. Resin and fiber roles on fatigue behavior of the composite material are investigated. It is concluded that effect of fiber orientation is complex but rapid crack growth is observed in the matrix parallel to the fibers in unidirectional materials [19]. Composite materials having higher modulus such as graphite and boron are examined and it is concluded that they have higher fatigue strength than glass fiber composites as seen in Figure 7 [18]. It is alleged that this may be caused by the less strain due to higher modulus at the same cyclic stress level.

In early 1980s, investigation of static and fatigue behavior of laminated composites have been increased. Statistical life prediction methods are mentioned [20] and based on fatigue damage mechanisms in composite laminates a pattern in fatigue-life diagrams is proposed [5].

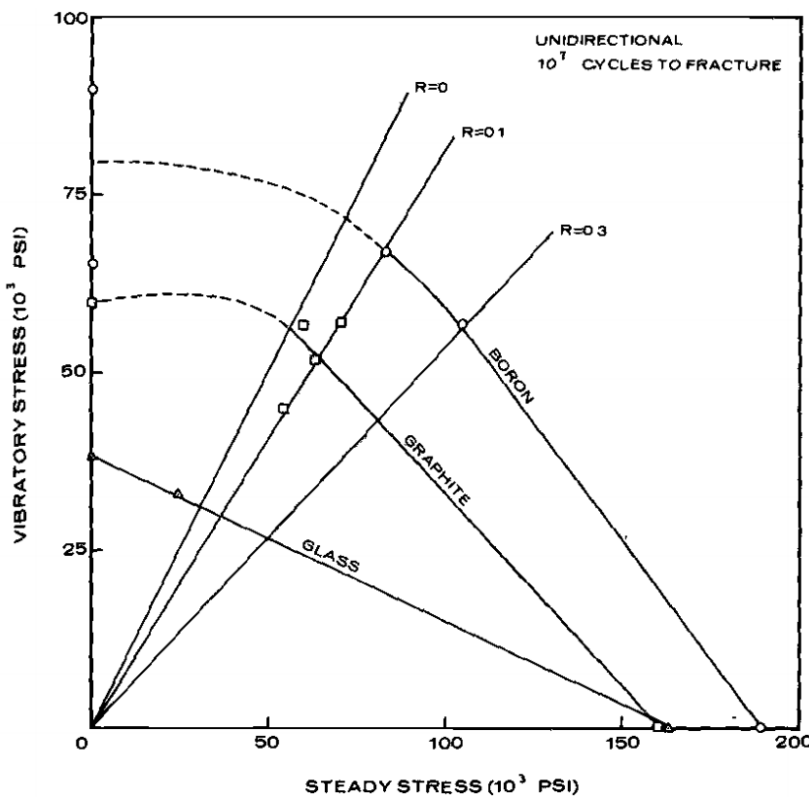


Figure 7. Comparison of fatigue strength of boron, graphite and glass fibers [18].

The matrix and fiber behavior under fatigue loading is investigated [20]. In Figure 8, stress strain curves of three composite materials are compared which are reinforced with the fibers as (a) metal matrix and (b) polymer matrix with boron or graphite fibers. It is observed from the stress strain graphs that the polymer matrix has low ductility.

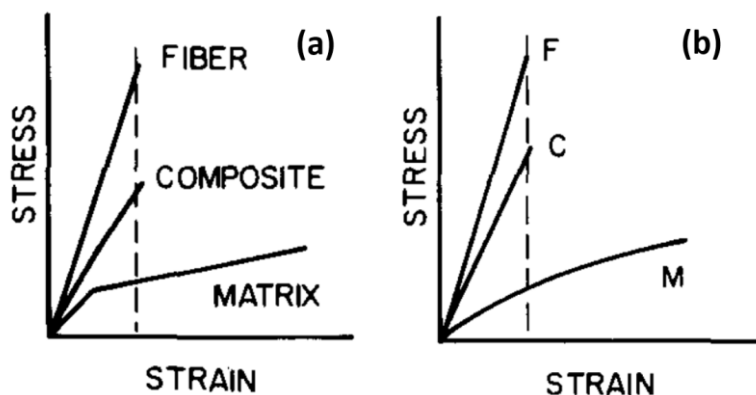


Figure 8. Stress strain curve of (a) metal matrix, (b) polymer matrix composites [20].

Matrix stiffness is very important for the fatigue fracture behavior of composite materials [7]. However, fracture strain of a composite material is dependent also on fiber stiffness. For low stiffness fibers such as glass-epoxy, fracture strain of composite material is much higher than that of matrix as seen in Figure 9 while the difference is not that much for the case of high stiffness fibers such as graphite-epoxy [5].

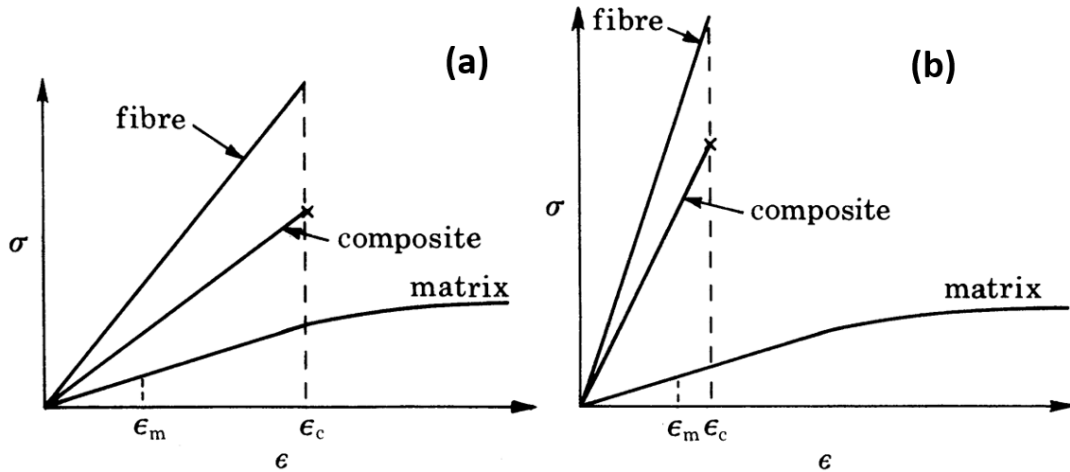


Figure 9. Stress strain curve of (a) low stiffness (glass) fibers, (b) high stiffness (graphite) fibers [5].

Fatigue strength and static strength of the composite materials are investigated with changing fiber volume fractions in Figure 10. Initiation of the fatigue cracks are expected from the weakest region of the material such as initial damages, free surfaces, fiber breaks or fiber ends [20], [21]. High fiber volume fraction leads to more fiber breaks and more corresponding crack initiations but on the other hand it obstructs the crack propagation of the crack due to more fibers. From these observations it is concluded that composite fatigue limit stress is dependent to fiber volume fraction while composite fatigue limit strain is not. While the fibers are effective on static strength, the matrix is effective on fatigue strength [20].

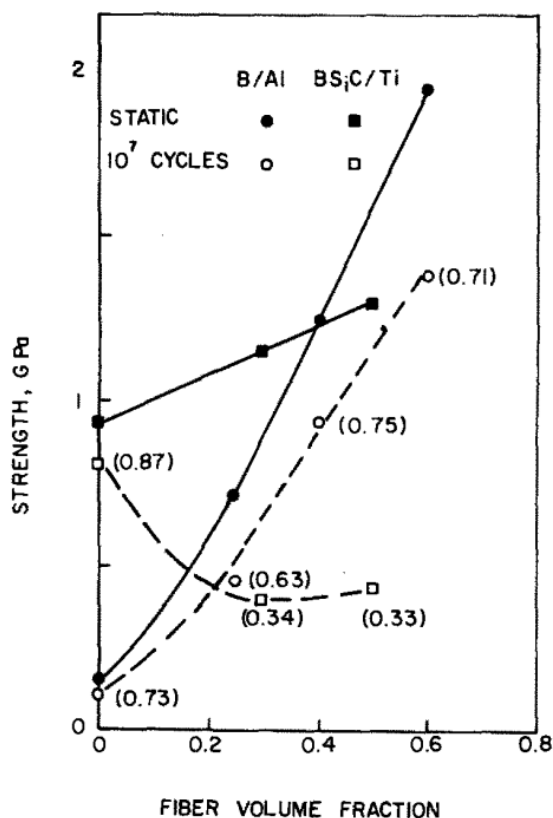


Figure 10. Change of strength with fiber volume fraction [20].

Curved Composite Laminates-Static

Increase in the percentage of use of laminated composites in aerospace and wind turbine structures brings the necessity of gaining knowledge about design of complex laminated composites. The first studies about failure of complex composite laminates are published in 1980s [22]. Springer and Chang proposed the first study on delamination in curved laminated composites. Then, at the beginning of 2000s, detailed observations about different failure types and improvements about FEMs are proposed. More recently, detailed experimental and numerical work was conducted in Coker group [21]-[28]. Gozlu and Coker conducted first dynamic simulation for unstable delamination during load drop. Dynamic process was seen first numerically. They also showed the first known experimental evidence of intersonic delamination in composite laminates [26]. In Figure 11, delamination initiation and propagation of in curved region for experimental and numerical results which are in good correlation is shown.

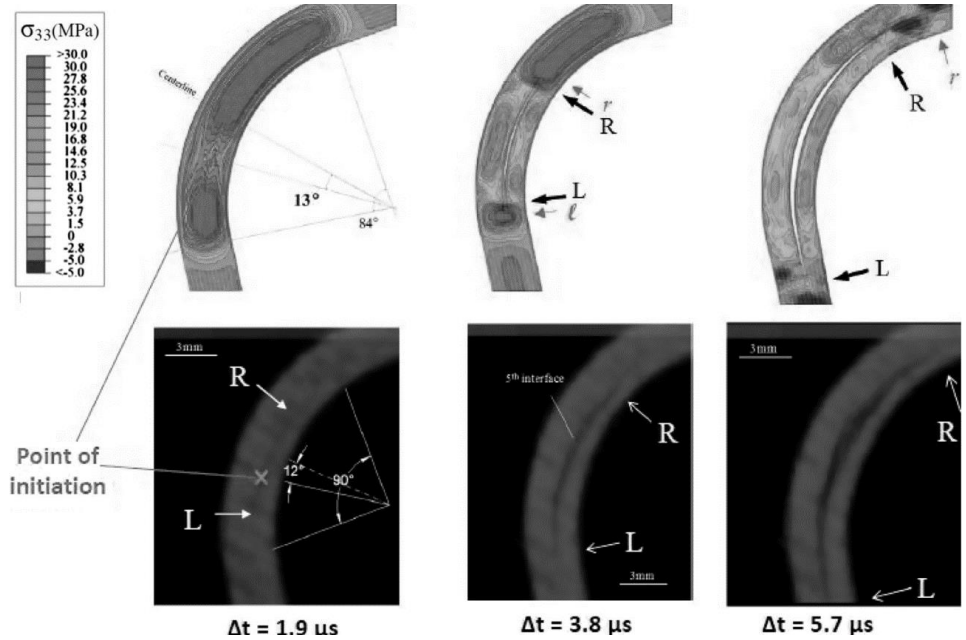


Figure 11. Comparison of delamination initiation and propagation for numerical and experimental results [26].

Curved Composite Laminates-Fatigue

In literature there are very few studies on fatigue behavior of curved composite laminates. Early and very valuable research about fatigue of curved laminated composites belongs to Martin and Jackson [29]. They carried out analytical, experimental and numerical studies to predict delamination onset and growth in cross-plyed curved composite laminates under static and fatigue loadings. Material was graphite/epoxy laminated composite. In order to determine stress distribution in the curved region, closed form elasticity solution and both 2D and 3D finite element analyses are conducted. Radial, tangential and shear stress distributions through the thickness direction are compared for elasticity solution, 2D and 3D FEA results as shown in Figure 12. For the case of radial stress while closed form solution, 2D and 3D at center line cases are agreed well, 3D FEA at free edge does not behave like them. However, in the case of radial stress all results give similar patterns. In shear stress distribution, 3D FEA at center line does not follow the pattern that followed by all other solutions. For all stress distributions, 2D FEA and closed form solutions give very close results.

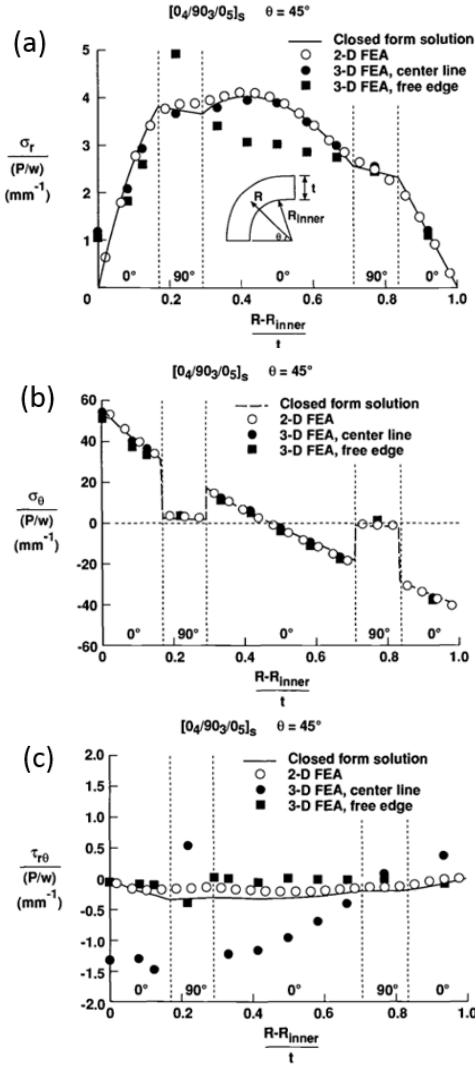


Figure 12. (a) Radial (b) tangential (c) shear stress through the thickness [29].

In further parts of the study, transverse tensile strength and fatigue life are determined from flat 90° coupons and interlaminar tensile strength and fatigue life are determined from UD curved laminates experimentally. Mode-I fatigue and fracture toughness data are determined from DCB experiments. Damage onset predictions are also performed. The prediction for interlaminar tension delamination in the 0° plies was in reasonable agreement with the experimental results for the curved laminate as shown in Figure 13. The predictions at the free edge were conservative, and the predictions at the center were in agreement with the experimental data. This prediction does not include the number of cycles to form the matrix crack and hence will generally be a conservative prediction.

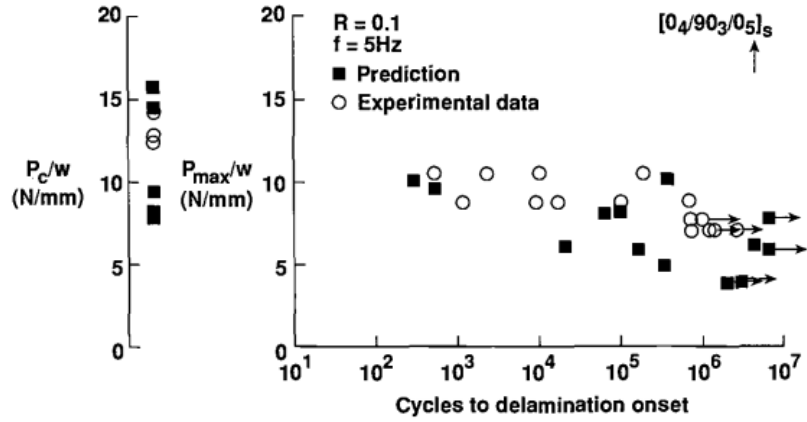


Figure 13. Prediction of interlaminar tension failure between 0° plies [29].

In another study, computational model of two-layer composite laminate is subjected to cyclic loading and thermal fatigue delamination is examined [30]. SN data for damage initiation in a carbon fiber laminate under pure interlaminar tensile cyclic loading is generated.

Blanchfield and Allegri [31] investigated delamination initiation due to interlaminar tension in fiber reinforced plastics using curved beam method. They mentioned two main methods to measure interlaminar tensile strength; flatwise tension specimen test and curved beam under bending test. They applied ASTM standard test methods. Analytical study is also applied for the curved region to calculate radial stress distribution through the thickness by Lekhnitskii solution. 2D Finite element analyses are also performed and compared with analytical results.

There was a mismatch between experimental results and FEA. By applying a correction to ASTM standard calculations, FEA and experimental results became in good agreement. The author states that ASTM standard assumes stiff specimens and does not account for deflection of specimen arms. This correction is simply adding increased angle of the deflected arm to calculations. To find correct angle an algorithm is created and implemented to Matlab. As can be seen in Figure 14, after the correction radial stress values of ASTM standard calculation results become closer to FEA result line.

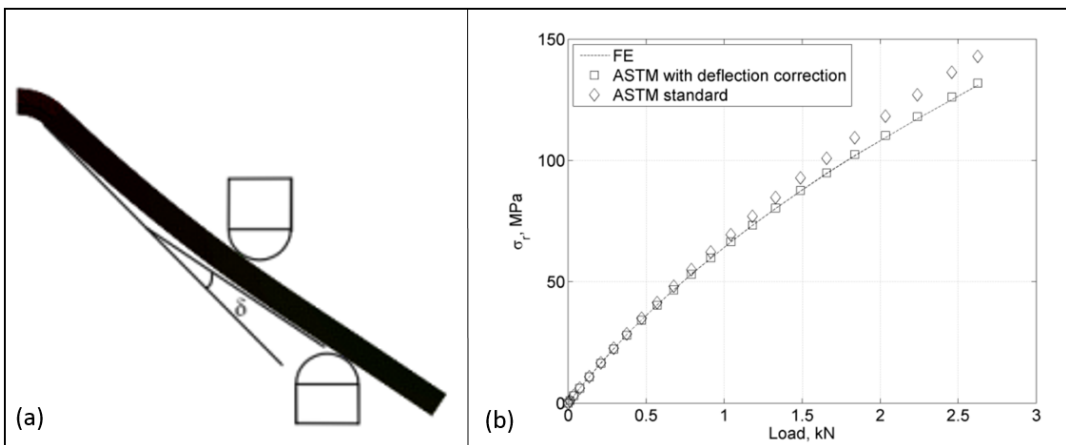


Figure 14. (a) Correction applied to ASTM standard, (b) radial stress distribution for corrected and uncorrected calculations [31].

Stress Field in Curved Laminates

Failure mechanisms of laminated composites have been investigated for years. Curved beams have been examined both to calculate interlaminar properties of the laminated composites and to understand failure problem itself caused by structural complexity. In literature, there are many studies about curved laminated composite corners starting from 1960s to today.

In 1996, methods of interlaminar tensile strength (ILTS) measurement for composite laminates were reviewed [32]. Four different methods shown in Figure 15 are discussed. The first type is delamination coupon specimen [33]. It was concluded that this type of specimen is inadequate to determine ILTS. Second type is variations of flatwise tension test specimens. This method used for the purpose of measurement of ILTS of glass-reinforced composites [34] while other researchers were using this method to measure ILTS of graphite/epoxy specimen [35]. Disadvantage of this method is that it requires relatively thick specimens, which may not be sufficiently representative of a particular composite structure. The third type is diametrical compression specimen [32]. Similar results are obtained as second type specimens and results showed variations with specimen thickness and diameter. The fourth type is curved beam test specimens.

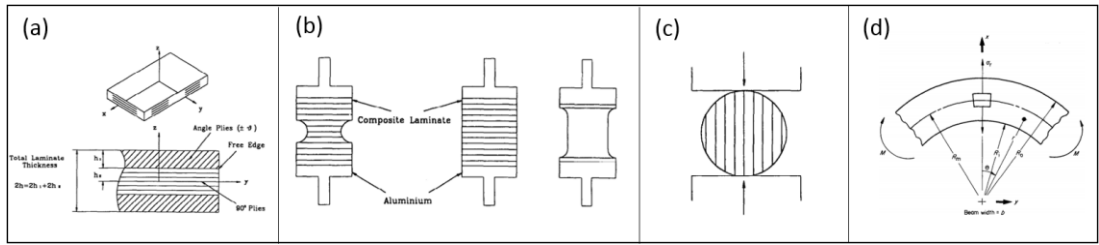


Figure 15. (a) Delamination coupon, (b) flatwise tension test, (c) diametrical compression disk specimen [32] and (d) curved beam test specimen [36].

There are lots of different applications of curved beams to determine ILTS in the literature. Some of them can be listed as in Figure 16(a) [36], (b) [37],(c) [32] (d) [32] (e) [32] and (f) [38]. To avoid combined effect of interlaminar tensile and shear stresses and to determine the exact ILTS, fixture in Figure 16(d) is created to apply pure bending moment [32].

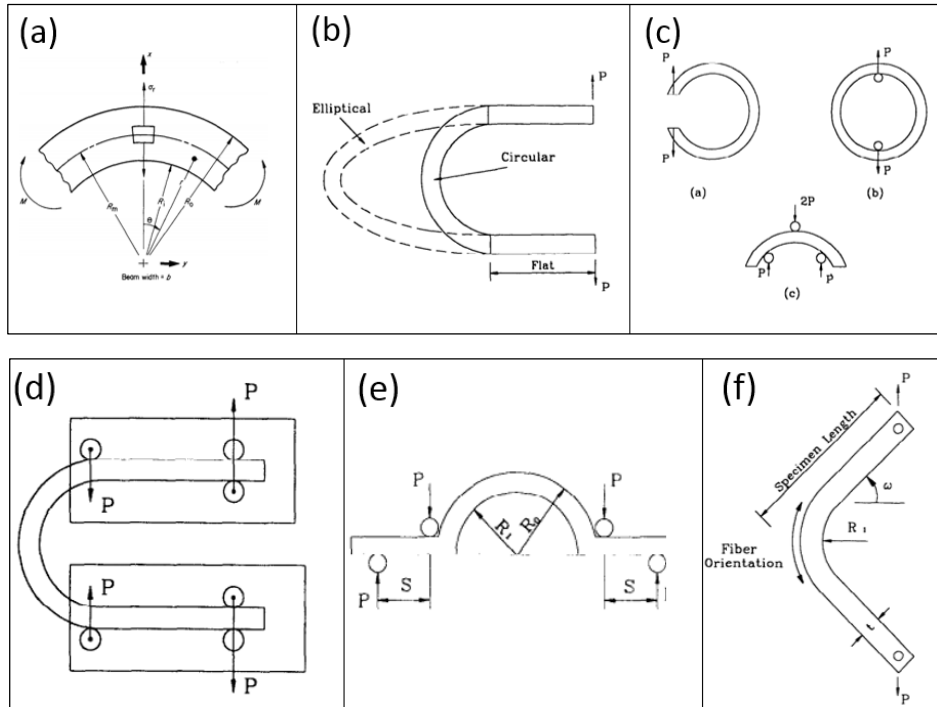


Figure 16. Curved beam test specimen types [32], [36] - [38].

Sun and Kelly [16] investigated failure of composite angle structures. Their research includes both experimental and numerical studies. They examined difference of bending and radial stress distributions in different angle plies as seen in Figure 17. Hill and Hill-Tsai failure criteria are used for the analyses. They discussed two possible

failure modes seen in laminated curved composites, i.e., matrix cracking caused by bending stress and delamination caused by radial stress in curved region. They used 3D hill failure criteria and stated that this criterion is good for predicting failure of curved composite structures.

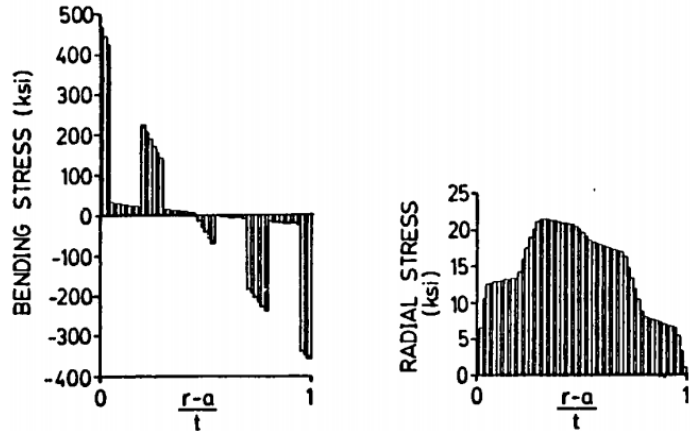


Figure 17. FEA bending and radial stress distributions of specimen [90/0₃/90₂/0₃/90] at $\theta=25^\circ$ [16].

As mentioned previously, several specimens and fixtures have been applied to measure ILTS by using curved beam method [32], [33]. Kedward [36] provide general analytical methods for curved beams under moment and end loading conditions separately as shown in Figure 18. Both isotropic and anisotropic solutions are provided in the paper. Anisotropic solutions are based on The Classical Elasticity Theory and derived by Lekhnitskii [39].

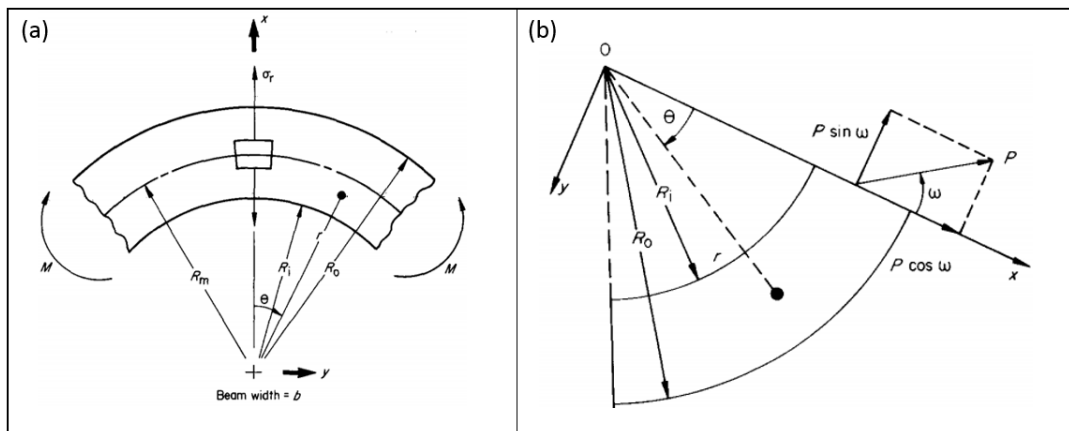


Figure 18. (a) Moment, (b) end load case [36].

Martin and Jackson [40] and Shivakumar et al. [38] used curved beam method under axial loading by hinges to measure interlaminar tensile strength. In both studies, loading mechanisms were very similar as shown in Figure 19. The only difference was type of hinges. The authors corrected the effect of their fixture offsets and they used corrected Lekhnitskii solution to calculate radial and tangential stresses through the thickness.

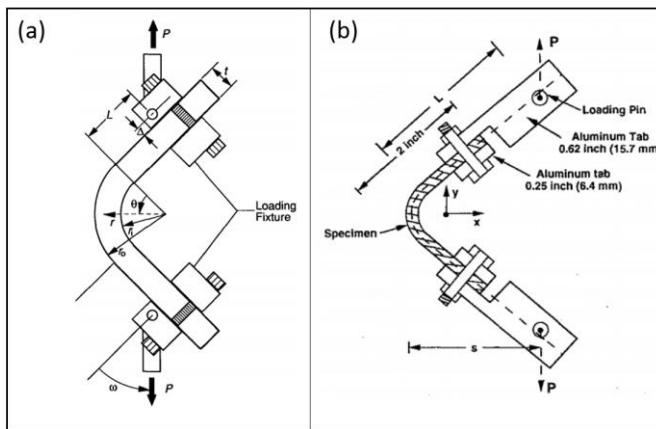


Figure 19. Loading mechanism of (a) Martin and Jackson [40] (b) Shivakumar et al. [38].

Four-point bending is a common method for curved beam testing. Jackson and Ifju [41] compared hinged loading mechanism and 4-point bending mechanism as shown in Figure 20. The comparison graph gives not only comparison of two different interlaminar tensile strength measurement testing methods but also gives comparison of different prepreg tape and textile RTM systems. General trend of the bar graph shows there are not any significant difference between 4-pt bending and HLM.

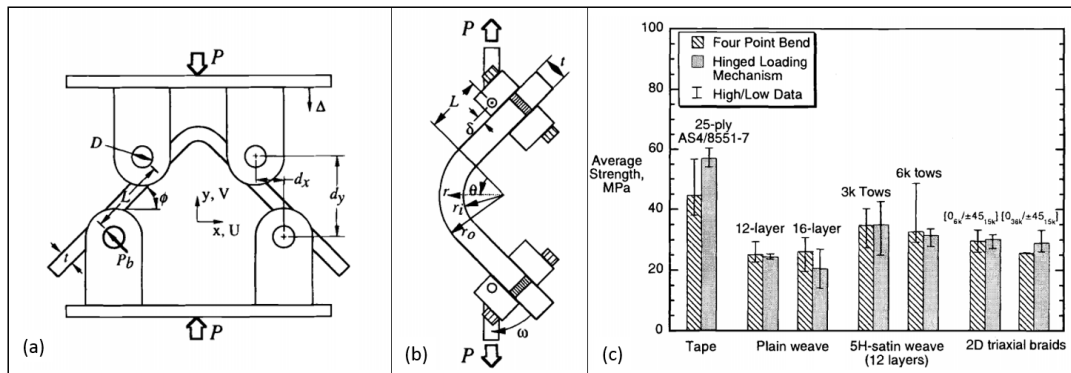


Figure 20. Schematic of test configurations (a) 4-pt bending, (b) hinged loading Mechanism (HLM) and (c) comparison of strengths for the two test methods [41].

Martin [42] investigated delamination failure occurred at curved region of UD curved composite laminates under static shear loading experimentally, analytically and numerically. Delamination initiation location is assumed as highest radial stress location. To predict delamination initiation location, curved beam elasticity solution is applied to define maximum radial stress location and compared with 2D finite element analysis. Stress distributions on the curved region are as seen in the Figure 21. At $\theta = 25^\circ$, normalized radial stress reaches the maximum value at a distance of approximately 40% of the thickness from the inner surface while the tangential stress reaches the value zero at 50%. In a certain θ value, FEA and analytical solutions are also in good agreement through the thickness. Elasticity solution can predict radial stresses between 20° and 60° around curved region.

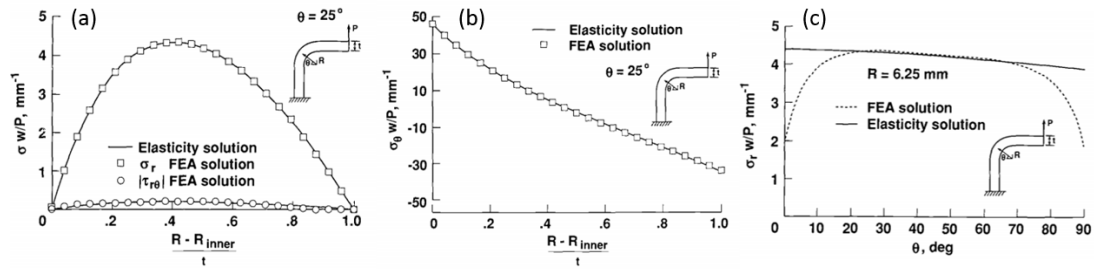


Figure 21. (a) Interlaminar stresses (b) tangential stress through the thickness and (c) radial stress around curved region [42].

CHAPTER 3

METHOD

In this chapter, experimental, analytical and finite element methods that are used in this investigation are explained in detail. In the experimental method section, the material and its manufacturing details, experimental set-up and procedure are explained. The section is followed by the analytical method and a presentation of the finite element model of the specimen.

3.1 Experimental Method

3.1.1 Material

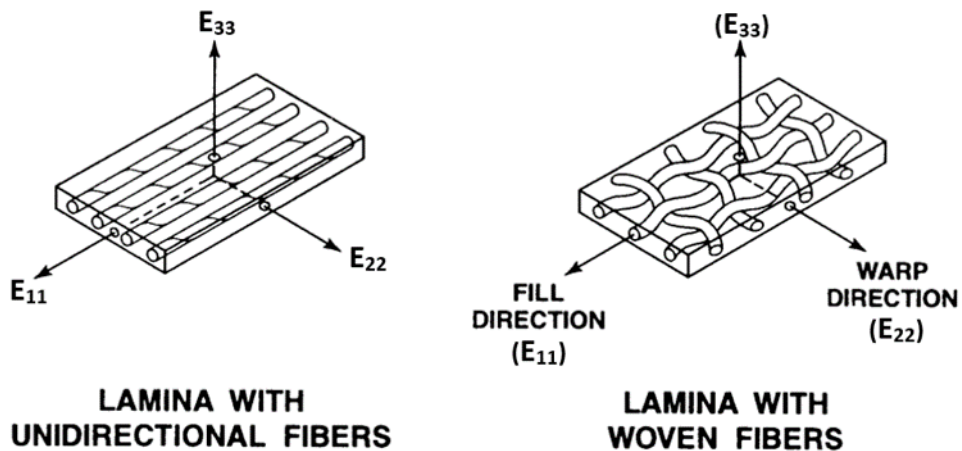
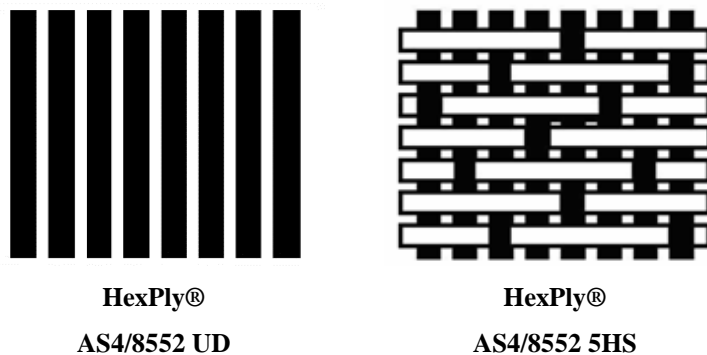


Figure 22. Unidirectional and woven laminas [43].

In aerospace applications and advanced wind turbine blades carbon fiber reinforced polymer (CFRP) composites are very commonly used. HexPly 8552 epoxy resin is one of the common matrix material used in these applications due to its good impact and damage tolerance behavior. In our study, laminated CFRP composite specimens are

manufactured from the prepgs which are composed of HexPly 8552 epoxy resin and carbon fibers from AS4 family by hand lay-up technique. Both unidirectional (UD) and woven laminates are manufactured for this investigation as shown in Figure 22. Fabric weave style used is 5-harness-stain (5HS). Lamina properties of the materials are tabulated in Table 1 [44]-[46].

Table 1. Lamina properties [44]-[46].



	HexPly® AS4/8552 UD	HexPly® AS4/8552 5HS
E_{11} (GPa)	135	55.7
E_{22} (GPa)	9.6	55.7
E_{33} (GPa)	9.6	8.5
v_{13}	0.32	0.30
v_{12}	0.32	0.05
v_{23}	0.487	0.30
G_{12} (GPa)	5.3	4.9
G_{13} (GPa)	5.3	3.7
G_{23} (GPa)	3.4	3.7
ρ (g/cm ³)	1.59	1.57
t_{ply} (mm)	0.184	0.280

3.1.2 Manufacturing Process

CFRP composite specimens are manufactured by hand lay-up technique. Manufacturing process of the specimens is as summarized in Figure 23.

- (a) An L-shape 1-m male aluminum tool with inner radius of 5mm is manufactured.
- (b) Carbon fiber-epoxy resin prepgs are laid according to the ply sequence by hand lay-up technique.
- (c) The lay-up is sealed in a vacuum bag.
- (d) After vacuum bagging part, the composite batch is put into autoclave for curing.
- (e) After curing process, composite batch is cut into 25-mm width pieces and final L shaped specimens are obtained.

This process is repeated for four different lay-up configurations:

- 1) $[0]_{30}$,
- 2) $[0_3/90_3/0_3/90_3/0_3]_s$,
- 3) $[0_3/90_3/0_3]_s$,
- 4) $[(45/0)_7, 45/45/0/45]$.

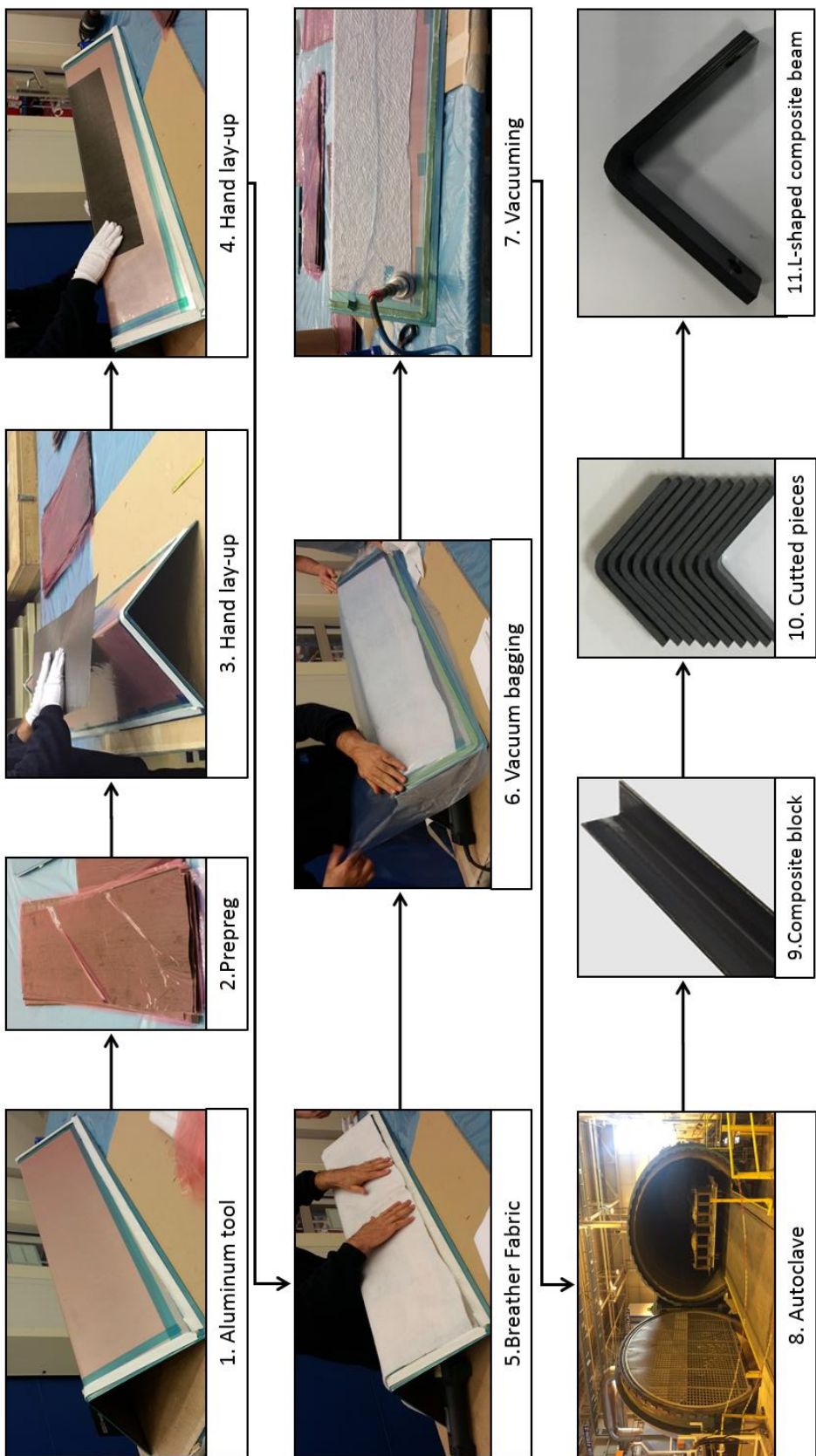


Figure 23: Manufacturing process.

3.1.3 Geometry and Laminate Properties

3.1.3.1 Geometry of L shaped beams

The geometry of the L-shaped specimen is shown schematically in Figure 24. The arm lengths, L_1 and L_2 , of the specimen are the same and equal to 90 mm and the width, w , is 25 mm. The inner radius, R_i , is 5mm. The thickness, t , is changing according to ply sequence as shown in Table 2.

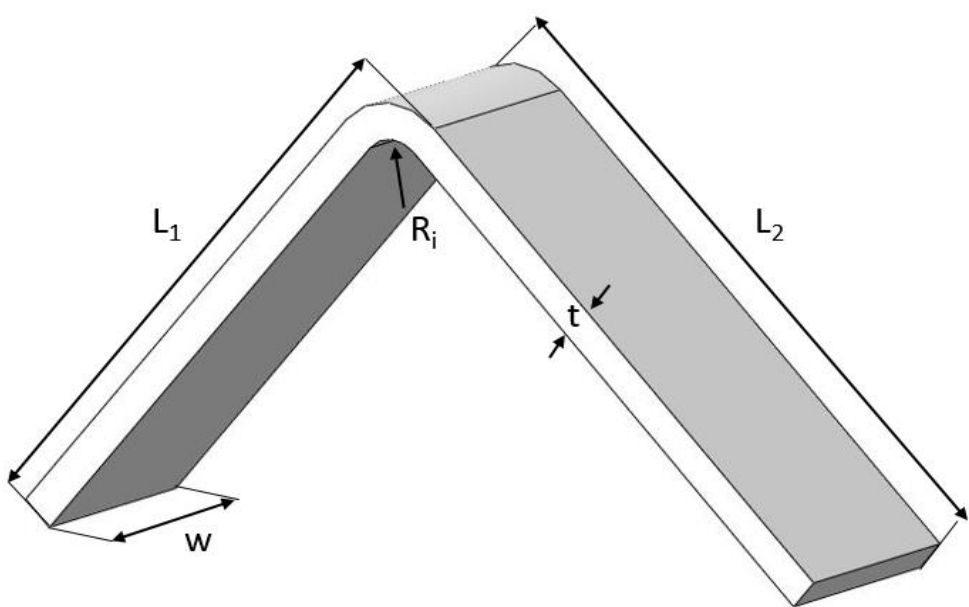


Figure 24. Geometry of the specimen.

Four different stacking sequences are chosen for experimental investigation as three UD and one fabric configuration. First specimen type is composed of fully UD layers of $[0]_{30}$. A batch of 11 $[0]_{30}$ specimens cut from the same plate are shown in Figure 23. All manufactured specimens and micrograph of the curved region are shown in Figure 25 and layer details are also shown on the micrograph. The other UD specimens are composed of 0 and 90° plies as $[0_3 / 90_3 / 0_3 / 90_3 / 0_3]_s$ and $[0_3 / 90_3 / 0_3]_s$. These configurations are created by grouping three layers of 0° and 90° layers. The layers are grouped to create thicker layers to be able to examine the failure of different angle plies in detail. The last configuration is composed of 0° and 45° fabric layers as $[(45/0)_7, 45/45/0/45]$. This stacking sequence is chosen according to lay-up configurations used in wing structures. Manufactured specimens and micrographs with

layer details of the curved region are shown between Figure 25 and Figure 28 for the specimens $[0]_{30}$, $[0_3/90_3/0_3/90_3/0_3]_s$, $[0_3/90_3/0_3]_s$ and $[(45/0)_7,45/45/0/45]$, respectively.

Dimensions of four specimens with only different thicknesses are listed in Table 2. Specimens are designed to have similar thickness values and same number of layers except the third type. The thickness of UD preps is 0.184 mm and woven preps is 0.280 mm. The total thickness of specimens is not exactly the number of plies times thickness of one prep layer due to manufacturing tolerances and imperfections. In some regions excessive resin may add some extra thickness.

Table 2. Dimensions of the specimens.

#	Lay-up	# of Plies	t (mm)	R_i (mm)	L_1 (mm)	L_2 (mm)	w (mm)
1	$[0]_{30}$	30	5.9	5	90	90	25
2	$[0_3/90_3/0_3/90_3/0_3]_s$	30	5.8	5	90	90	25
3	$[0_3/90_3/0_3]_s$	18	3.5	5	90	90	25
4	$[(45/0)_7,45/45/0/45]$	18	5.3	5	90	90	25

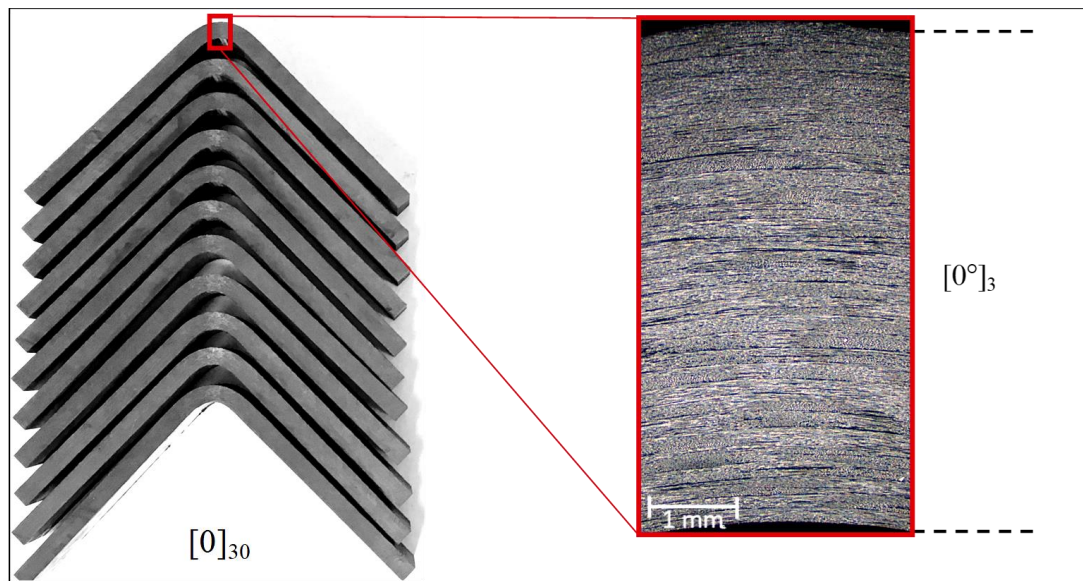


Figure 25. Stacking details of the UD $[0]_{30}$ specimen.

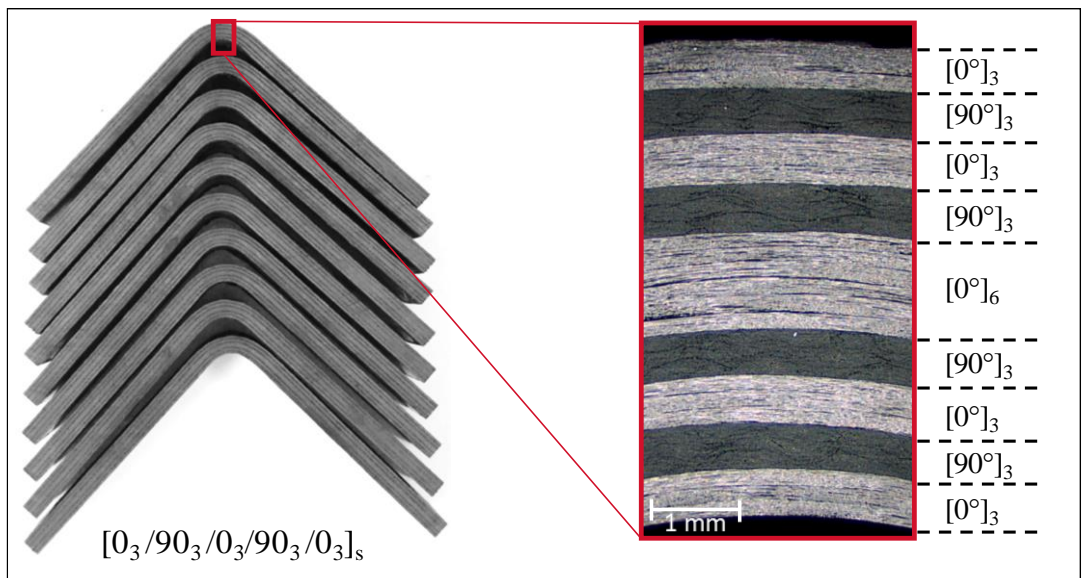


Figure 26. Stacking details of the thick cross-ply $[0_3/90_3/0_3/90_3/0_3]_s$ specimen.

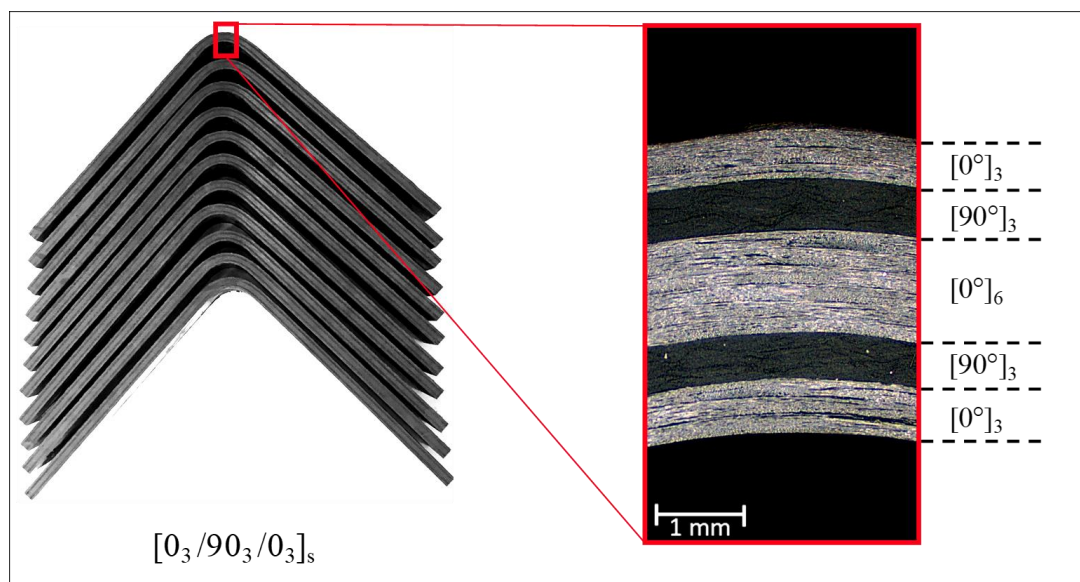


Figure 27. Stacking details of the thin cross-ply $[0_3/90_3/0_3]_s$ specimen.

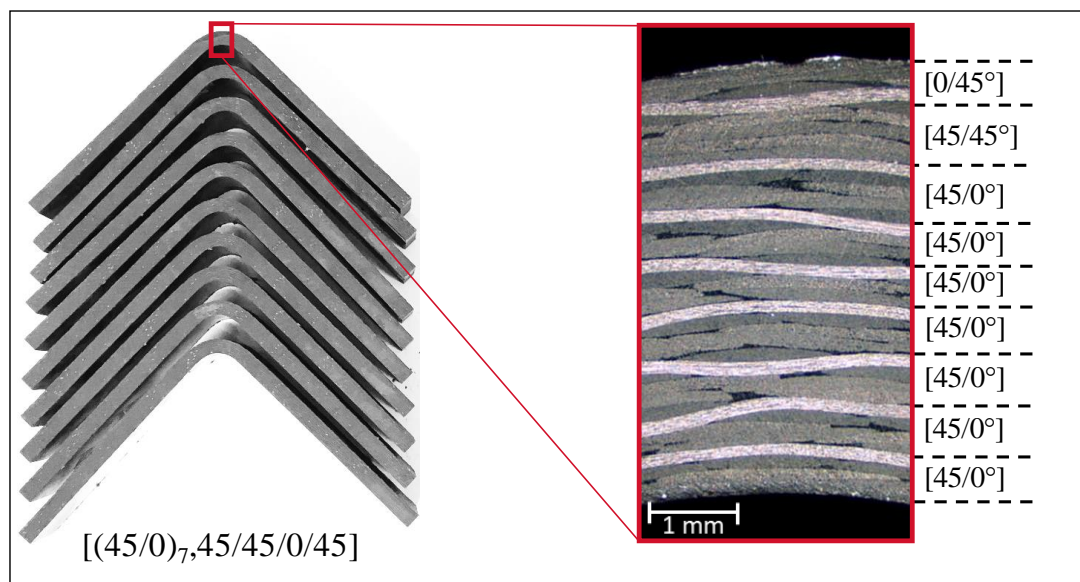


Figure 28. Stacking details of the fabric $[(45/0)_7,45/45/0/45]$ specimen.

3.1.3.2 Calculation of Laminate Properties

Laminate properties of the specimens are calculated according to classical lamination theory. Calculation method is applied according to Nettles [47] and calculation steps are explained in details. The generalized Hooke's law relating stresses and strains is written in contracted notation as follows:

$$\sigma_i = C_{ij}\varepsilon_j$$

Considering the isotropic materials, the stiffness matrix has only two independent constants due to infinite number of material property symmetry:

$$\begin{bmatrix} \sigma_1 \\ \sigma_2 \\ \sigma_3 \\ \tau_{23} \\ \tau_{31} \\ \tau_{12} \end{bmatrix} = \begin{bmatrix} C_{11} & C_{12} & C_{12} & 0 & 0 & 0 \\ C_{12} & C_{11} & C_{12} & 0 & 0 & 0 \\ C_{12} & C_{12} & C_{11} & 0 & 0 & 0 \\ 0 & 0 & 0 & (C_{11} - C_{12})/2 & 0 & 0 \\ 0 & 0 & 0 & 0 & (C_{11} - C_{12})/2 & 0 \\ 0 & 0 & 0 & 0 & 0 & (C_{11} - C_{12})/2 \end{bmatrix} \begin{bmatrix} \varepsilon_1 \\ \varepsilon_2 \\ \varepsilon_3 \\ \gamma_{23} \\ \gamma_{31} \\ \gamma_{12} \end{bmatrix}$$

For the case of anisotropic materials direction is an important concern and must be considered. For laminated composite materials this relationship becomes:

$$\{\sigma\}_k = [\bar{Q}]_k \{\varepsilon\}_k$$

In which, \bar{Q} is stiffness matrix of oriented lamina. Strains at any point in the laminate can be related to the reference (mid) plane strains and the laminate curvatures as follows:

$$\begin{Bmatrix} \varepsilon_x \\ \varepsilon_y \\ \gamma_{xy} \end{Bmatrix} = \begin{Bmatrix} \varepsilon_x^0 \\ \varepsilon_x^0 \\ \gamma_{xy}^0 \end{Bmatrix} + z \begin{Bmatrix} \kappa_x \\ \kappa_y \\ \kappa_{xy} \end{Bmatrix}$$

Where, plate curvatures are:

$$\kappa_x = -\frac{\partial^2 \omega_0}{\partial x^2}, \kappa_y = -\frac{\partial^2 \omega_0}{\partial y^2}, \kappa_z = -\frac{\partial^2 \omega_0}{\partial x \partial y}$$

and ω is bending displacement.

Global stresses are integrated in each lamina to obtain resultant laminate forces and moments per unit length in the x-y plane through the laminate thickness;

$$\begin{aligned} N_x &= \int_{-h/2}^{h/2} \sigma_x dz \quad \text{and} \quad M_x = \int_{-h/2}^{h/2} \sigma_x z dz \\ N_y &= \int_{-h/2}^{h/2} \sigma_y dz \quad \text{and} \quad M_x = \int_{-h/2}^{h/2} \sigma_y z dz \\ N_{xy} &= \int_{-h/2}^{h/2} \tau_{xy} dz \quad \text{and} \quad M_x = \int_{-h/2}^{h/2} \tau_{xy} z dz \end{aligned}$$

Plugging strain relation at any point into stress-strain equation of an oriented lamina gives:

$$\begin{Bmatrix} N_x \\ N_y \\ N_{xy} \end{Bmatrix} = [A]\{\varepsilon_0\} + [B]\{\kappa\}$$

$$\begin{Bmatrix} M_x \\ M_y \\ M_{xy} \end{Bmatrix} = [B]\{\varepsilon_0\} + [D]\{\kappa\}$$

In which [A], [B] and [D] matrices are defined as,

$$A_{ij} = \sum_{k=1}^n (\bar{Q}_{ij})_k \cdot (h_k - h_{k-1})$$

$$B_{ij} = \frac{1}{2} \sum_{k=1}^n (\bar{Q}_{ij})_k \cdot (h_k^2 - h_{k-1}^2)$$

$$D_{ij} = \frac{1}{3} \sum_{k=1}^n (\bar{Q}_{ij})_k \cdot (h_k^3 - h_{k-1}^3)$$

The constitutive equations can be written in matrix and contracted form as follows,

$$\begin{bmatrix} N_x \\ N_y \\ N_{xy} \\ M_x \\ M_y \\ M_{xy} \end{bmatrix} = \begin{bmatrix} A_{11} & A_{12} & A_{16} & B_{11} & B_{12} & B_{16} \\ A_{12} & A_{22} & A_{26} & B_{12} & B_{22} & B_{26} \\ A_{16} & A_{26} & A_{66} & B_{16} & B_{26} & B_{66} \\ B_{11} & B_{12} & B_{16} & D_{11} & D_{12} & D_{16} \\ B_{12} & B_{22} & B_{26} & D_{12} & D_{22} & D_{26} \\ B_{16} & B_{26} & B_{66} & D_{16} & D_{26} & D_{66} \end{bmatrix} \begin{bmatrix} \varepsilon_x^0 \\ \varepsilon_y^0 \\ \gamma_{xy}^0 \\ \kappa_x \\ \kappa_y \\ \kappa_{xy} \end{bmatrix}$$

$$\begin{bmatrix} N \\ M \end{bmatrix} = \begin{bmatrix} A & B \\ B & D \end{bmatrix} \begin{bmatrix} \varepsilon^0 \\ \kappa \end{bmatrix}$$

In order to find E_x , only x-direction in-plane load is applied. Hence the constitutive equation becomes:

$$\begin{bmatrix} N_x \\ 0 \\ 0 \\ 0 \\ 0 \\ 0 \end{bmatrix} = \begin{bmatrix} A_{11} & A_{12} & A_{16} & B_{11} & B_{12} & B_{16} \\ A_{12} & A_{22} & A_{26} & B_{12} & B_{22} & B_{26} \\ A_{16} & A_{26} & A_{66} & B_{16} & B_{26} & B_{66} \\ B_{11} & B_{12} & B_{16} & D_{11} & D_{12} & D_{16} \\ B_{12} & B_{22} & B_{26} & D_{12} & D_{22} & D_{26} \\ B_{16} & B_{26} & B_{66} & D_{16} & D_{26} & D_{66} \end{bmatrix} \begin{bmatrix} \varepsilon_x^0 \\ \varepsilon_y^0 \\ \gamma_{xy}^0 \\ \kappa_x \\ \kappa_y \\ \kappa_{xy} \end{bmatrix}$$

Above equation is solved by using Cramer's rule to obtain ε_x^0 :

$$\varepsilon_x^0 = \frac{\begin{vmatrix} N_x & A_{12} & A_{16} & B_{11} & B_{12} & B_{16} \\ 0 & A_{22} & A_{26} & B_{12} & B_{22} & B_{26} \\ 0 & A_{26} & A_{66} & B_{16} & B_{26} & B_{66} \\ 0 & B_{12} & B_{16} & D_{11} & D_{12} & D_{16} \\ 0 & B_{22} & B_{26} & D_{12} & D_{22} & D_{26} \\ 0 & B_{26} & B_{66} & D_{16} & D_{26} & D_{66} \end{vmatrix}}{\begin{vmatrix} A_{11} & A_{12} & A_{16} & B_{11} & B_{12} & B_{16} \\ A_{12} & A_{22} & A_{26} & B_{12} & B_{22} & B_{26} \\ A_{16} & A_{26} & A_{66} & B_{16} & B_{26} & B_{66} \\ B_{11} & B_{12} & B_{16} & D_{11} & D_{12} & D_{16} \\ B_{12} & B_{22} & B_{26} & D_{12} & D_{22} & D_{26} \\ B_{16} & B_{26} & B_{66} & D_{16} & D_{26} & D_{66} \end{vmatrix}}$$

Previous equation is simplified by using cofactor expansion:

$$\varepsilon_x^0 = \frac{N_x}{\varepsilon_x^0} = \frac{\begin{vmatrix} A_{22} & A_{26} & B_{12} & B_{22} & B_{26} \\ A_{26} & A_{66} & B_{16} & B_{26} & B_{66} \\ B_{12} & B_{16} & D_{11} & D_{12} & D_{16} \\ B_{22} & B_{26} & D_{12} & D_{22} & D_{26} \\ B_{26} & B_{66} & D_{16} & D_{26} & D_{66} \end{vmatrix}}{\begin{vmatrix} A_{11} & A_{12} & A_{16} & B_{11} & B_{12} & B_{16} \\ A_{12} & A_{22} & A_{26} & B_{12} & B_{22} & B_{26} \\ A_{16} & A_{26} & A_{66} & B_{16} & B_{26} & B_{66} \\ B_{11} & B_{12} & B_{16} & D_{11} & D_{12} & D_{16} \\ B_{12} & B_{22} & B_{26} & D_{12} & D_{22} & D_{26} \\ B_{16} & B_{26} & B_{66} & D_{16} & D_{26} & D_{66} \end{vmatrix}}$$

And E_x can be found by evaluating:

$$E_x = \frac{\sigma}{\varepsilon_x^0} = \frac{N_x/h}{\varepsilon_x^0} = \frac{\begin{vmatrix} A_{11} & A_{12} & A_{16} & B_{11} & B_{12} & B_{16} \\ A_{12} & A_{22} & A_{26} & B_{12} & B_{22} & B_{26} \\ A_{16} & A_{26} & A_{66} & B_{16} & B_{26} & B_{66} \\ B_{11} & B_{12} & B_{16} & D_{11} & D_{12} & D_{16} \\ B_{12} & B_{22} & B_{26} & D_{12} & D_{22} & D_{26} \\ B_{16} & B_{26} & B_{66} & D_{16} & D_{26} & D_{66} \end{vmatrix}}{\begin{vmatrix} A_{22} & A_{26} & B_{12} & B_{22} & B_{26} \\ A_{26} & A_{66} & B_{16} & B_{26} & B_{66} \\ B_{12} & B_{16} & D_{11} & D_{12} & D_{16} \\ B_{22} & B_{26} & D_{12} & D_{22} & D_{26} \\ B_{26} & B_{66} & D_{16} & D_{26} & D_{66} \end{vmatrix}} \frac{1}{h}$$

Similar steps are followed for E_y and it is found as follows:

$$E_y = \frac{N_y/h}{\varepsilon_y^0} = \frac{\begin{vmatrix} A_{11} & A_{12} & A_{16} & B_{11} & B_{12} & B_{16} \\ A_{12} & A_{22} & A_{26} & B_{12} & B_{22} & B_{26} \\ A_{16} & A_{26} & A_{66} & B_{16} & B_{26} & B_{66} \\ B_{11} & B_{12} & B_{16} & D_{11} & D_{12} & D_{16} \\ B_{12} & B_{22} & B_{26} & D_{12} & D_{22} & D_{26} \\ B_{16} & B_{26} & B_{66} & D_{16} & D_{26} & D_{66} \end{vmatrix}}{\begin{vmatrix} A_{11} & A_{16} & B_{11} & B_{12} & B_{16} \\ A_{16} & A_{66} & B_{16} & B_{26} & B_{66} \\ B_{11} & B_{16} & D_{11} & D_{12} & D_{16} \\ B_{12} & B_{26} & D_{12} & D_{22} & D_{26} \\ B_{16} & B_{66} & D_{16} & D_{26} & D_{66} \end{vmatrix}} \frac{1}{h}$$

G_{xy} will be given by:

$$G_{xy} = \frac{N_{xy}/h}{\gamma_{xy}^0} = \frac{\begin{vmatrix} A_{11} & A_{12} & A_{16} & B_{11} & B_{12} & B_{16} \\ A_{12} & A_{22} & A_{26} & B_{12} & B_{22} & B_{26} \\ A_{16} & A_{26} & A_{66} & B_{16} & B_{26} & B_{66} \\ B_{11} & B_{12} & B_{16} & D_{11} & D_{12} & D_{16} \\ B_{12} & B_{22} & B_{26} & D_{12} & D_{22} & D_{26} \\ B_{16} & B_{26} & B_{66} & D_{16} & D_{26} & D_{66} \end{vmatrix}}{\begin{vmatrix} A_{11} & A_{12} & B_{11} & B_{12} & B_{16} \\ A_{12} & A_{22} & B_{12} & B_{22} & B_{26} \\ B_{11} & B_{12} & D_{11} & D_{12} & D_{16} \\ B_{12} & B_{22} & D_{12} & D_{22} & D_{26} \\ B_{16} & B_{26} & D_{16} & D_{26} & D_{66} \end{vmatrix}} \frac{1}{h}$$

For v_{xy} , ε_y^0 is obtained by:

$$\varepsilon_y^0 = \frac{-N_x \begin{vmatrix} A_{12} & A_{26} & B_{12} & B_{22} & B_{26} \\ A_{16} & A_{66} & B_{16} & B_{26} & B_{66} \\ B_{11} & B_{16} & D_{11} & D_{12} & D_{16} \\ B_{12} & B_{26} & D_{12} & D_{22} & D_{26} \\ B_{16} & B_{66} & D_{16} & D_{26} & D_{66} \end{vmatrix}}{\begin{vmatrix} A_{11} & A_{12} & A_{16} & B_{11} & B_{12} & B_{16} \\ A_{12} & A_{22} & A_{26} & B_{12} & B_{22} & B_{26} \\ A_{16} & A_{26} & A_{66} & B_{16} & B_{26} & B_{66} \\ B_{11} & B_{12} & B_{16} & D_{11} & D_{12} & D_{16} \\ B_{12} & B_{22} & B_{26} & D_{12} & D_{22} & D_{26} \\ B_{16} & B_{26} & B_{66} & D_{16} & D_{26} & D_{66} \end{vmatrix}}$$

Thus, v_{xy} will be given by:

$$v_{xy} = \frac{-\varepsilon_y^0}{\varepsilon_x^0} = \frac{-\begin{vmatrix} A_{12} & A_{26} & B_{12} & B_{22} & B_{26} \\ A_{16} & A_{66} & B_{16} & B_{26} & B_{66} \\ B_{11} & B_{16} & D_{11} & D_{12} & D_{16} \\ B_{12} & B_{26} & D_{12} & D_{22} & D_{26} \\ B_{16} & B_{66} & D_{16} & D_{26} & D_{66} \end{vmatrix}}{\begin{vmatrix} A_{22} & A_{26} & B_{12} & B_{22} & B_{26} \\ A_{26} & A_{66} & B_{16} & B_{26} & B_{66} \\ B_{12} & B_{16} & D_{11} & D_{12} & D_{16} \\ B_{22} & B_{26} & D_{12} & D_{22} & D_{26} \\ B_{26} & B_{66} & D_{16} & D_{26} & D_{66} \end{vmatrix}}$$

By using the presented method above, laminate properties are calculated for four stacking sequences and given in Table 3. Micrographs which represent the stacking sequence of the specimens are given in Figure 29.

Table 3. Calculated laminate properties.

#	Orientation	E_x (GPa)	E_y (GPa)	G_{xy} (GPa)	v_{xy}
1	$[0]_{30}$	135.00	9.60	5.30	0.320
2	$[0_3/90_3/0_3/90_3/0_3]_s$	85.30	60.09	5.30	0.051
3	$[0_3/90_3/0_3]_s$	93.70	51.68	5.30	0.060
4	$[(45/0)_7, 45/45/0/45]$	38.05	38.05	16.57	0.350

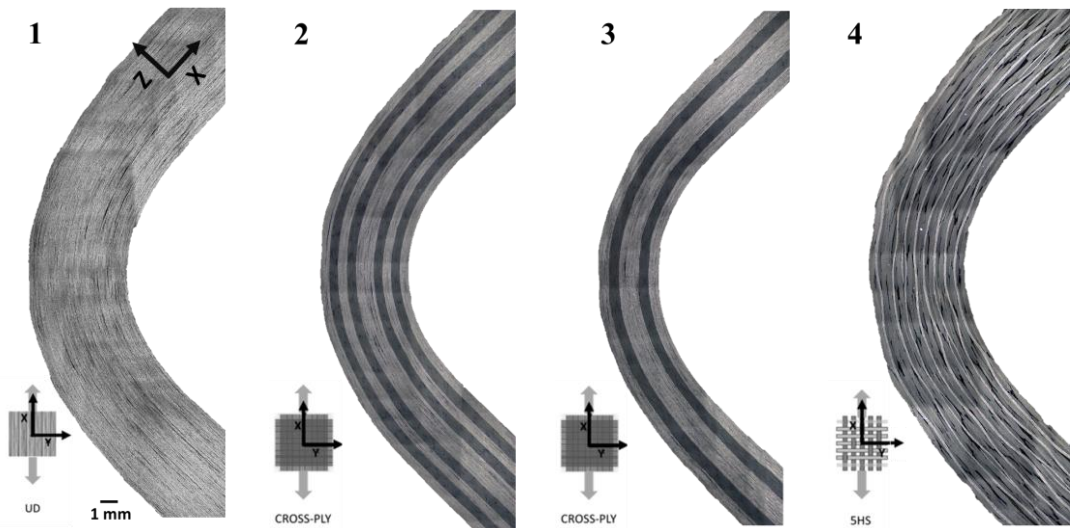


Figure 29. Stacking sequence of specimens in micrographs.

3.1.4 Specimen Preparation

3.1.4.1 Drilling Holes

8-mm diameter holes are opened at both arms of the L-shaped specimens 75 mm away from the outside line of the curved region as seen in Figure 30 to mount the specimen to the fixture. 8 mm bolts and nuts are used to fasten the arms of the specimens to the fixture.

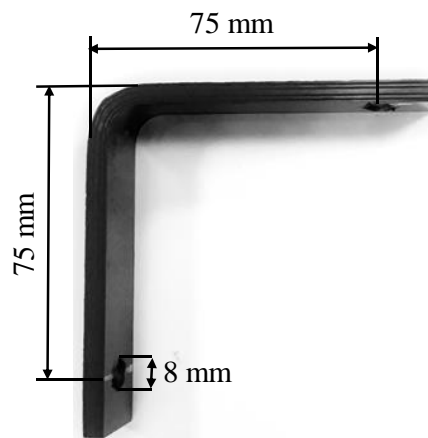


Figure 30. Holes on the arms.

3.1.4.2 Polishing the Surface

Before the experiments, surface of every specimen is polished to visualize the cracks on the surface clearly. Presi Minitech 233 polishing machine seen in Figure 31 is used to polish the CFRP composite specimen surfaces. Polishing steps are followed according to carbon fiber composite material polishing prescription.



Figure 31. Polishing machine.

3.1.4.3 Microscope

For each specimen before and after experiment micrographs are captured by a Huvitz digital microscope shown in Figure 32. Before the experiments, specimens are examined to avoid an initial defect on the side surface. After the experiments, delamination and matrix cracks can be observed in details by micrographs.



Figure 32. Digital microscope.

3.1.4.4 Painting the Surface

For the case of high speed camera and DIC experiments, specimen surface is painted by a white spray paint. For the high speed tests, with 500,000 fps, provided external lights are insufficient to lighten the dark surfaces due to increased aperture. To make the cracks visible, the side surface is painted to white. For the DIC experiments black speckles must be spread on the white paint as seen in Figure 33 (c). Speckle pattern and size should be adjusted according to the captured area.

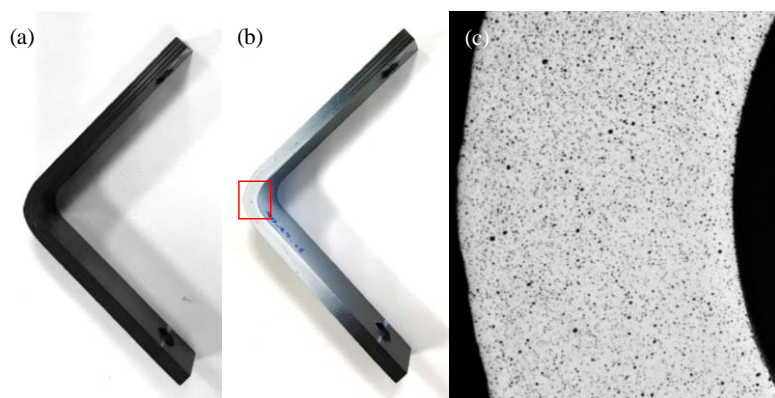


Figure 33. (a) Unpainted, (b) painted and (c) painted close-up photograph of the specimen.

3.1.5 Fixture and Experimental Setup

3.1.5.1 Fixture Design and Loading Condition

In order to examine the effect of combined loading to failure mechanisms in the curved laminates, vertical load (in y-direction) is applied at the ends of the arms of the L-shaped geometry (75 mm away from the curved region) as seen in Figure 34. Applied vertical force at the ends of the arms leads to moment loading at the curved region due to moment arm.

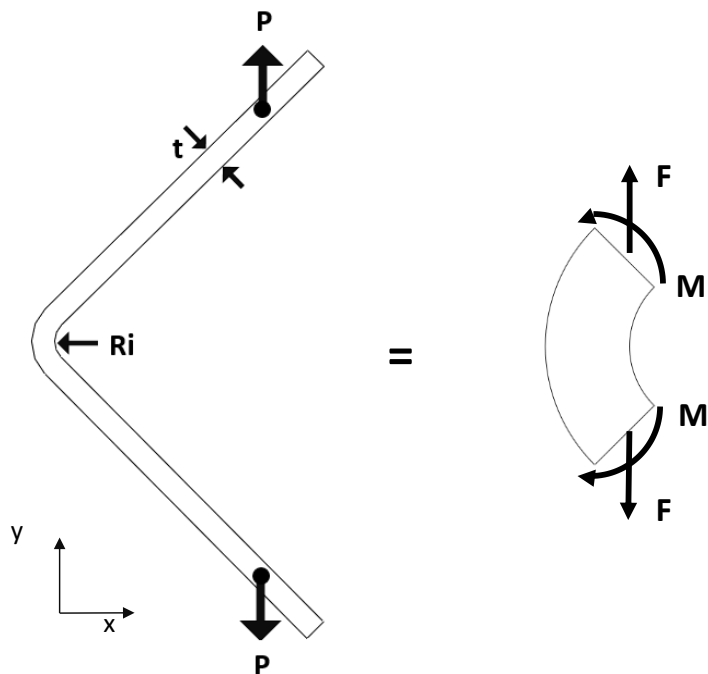


Figure 34. Free body diagram of the specimen.

Loading fixture is designed to create combined moment/axial loading as shown in the free-body diagram in Figure 34. The specimen is bolted to freely rotating pin and loading is applied in the vertical direction as seen in Figure 35. Except rotating pin part the loading fixture is in a single piece in order to avoid compliance effects of bolted or welded parts on the experiments. 60 mm support parts are added to the top of the gripped parts of the fixtures to support the fixture and the grips to avoid any compression on the fixtures and noise in experimental data due to the fixture effects.

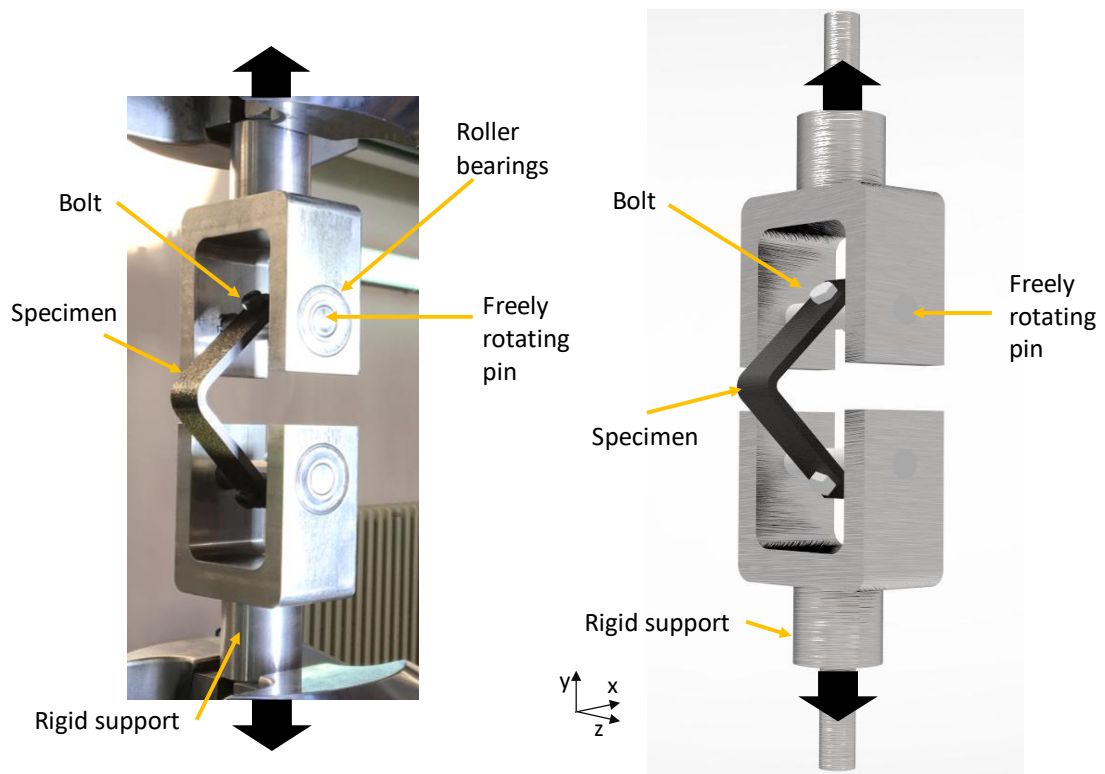


Figure 35. Loading fixture (a) photograph and (b) CAD drawing.

Old fixture:

The old fixture shown in Figure 36 (a) had too many connections. It was clamped to the grips with nuts and bolts. These connections leads to a nonlinear behavior on the load-displacement curve at the elastic region as seen in Figure 36 (a). It was clear that it cannot be the behavior of the specimen itself. It was probably due to the connections on the fixture.

To overcome this problem, the new fixture is manufactured in one piece with rigid supports. Only additional piece is freely rotating pin. As seen in Figure 36 (b), the nonlinearity problem in the load-displacement curve is removed with the new fixture.

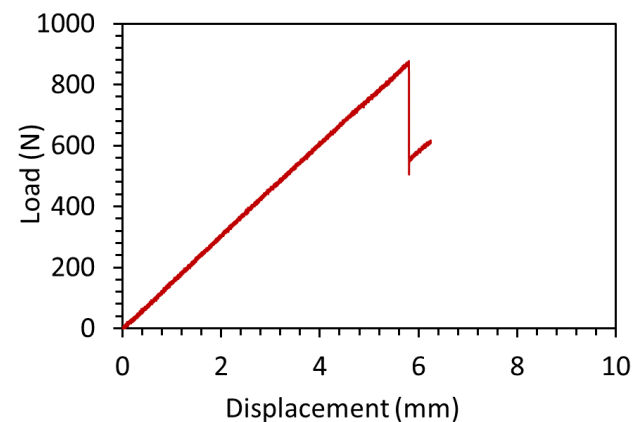
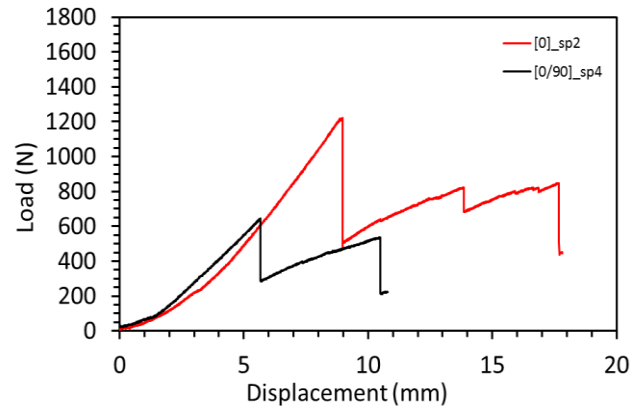
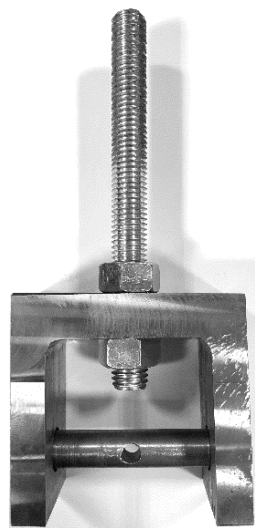


Figure 36. Comparison of results for old fixture [48] and the new fixture.

3.1.5.2 Experimental Setup

The specimen is mounted on the freely rotating pin on the loading fixture and the fixture is clamped to the servo-hydraulic 250 kN static/fatigue testing machine as shown in Figure 37. Loading is applied in the vertical direction. Upper cross head is fixed and lower cross head is moving axially according to given loading. Application direction of load is vertical but applied load on the curved region of the specimen is combined axial and moment load due to shape of the specimen itself.

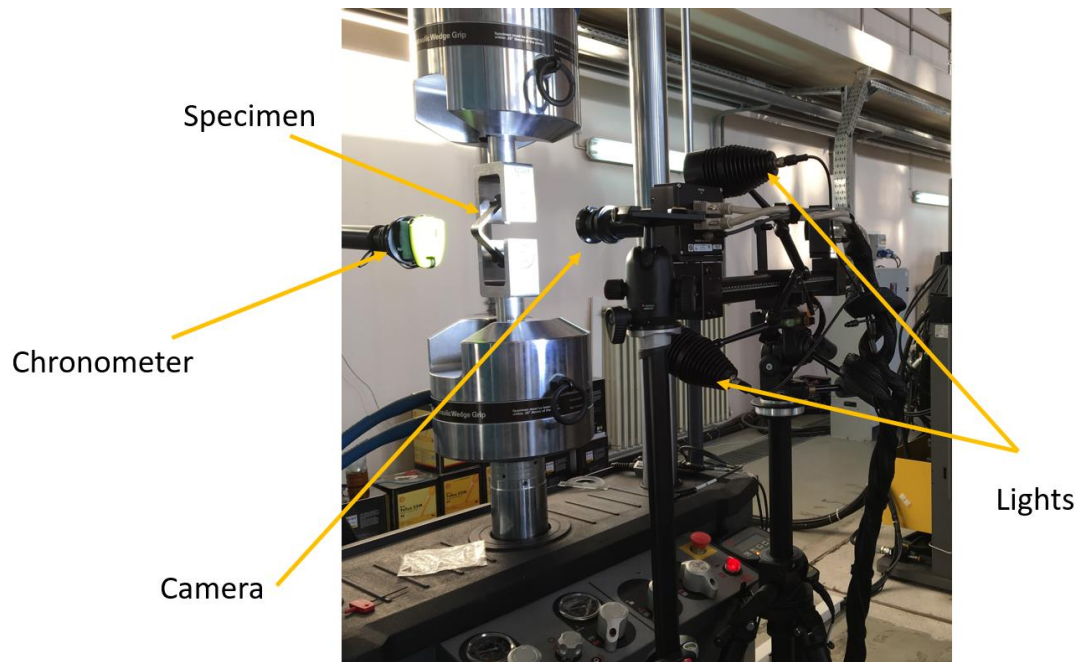


Figure 37. Experimental set-up.

In this study, experiments can be mentioned into two parts as static and fatigue experiments. Both fatigue and static experiments are performed in the same test machine and using the same loading fixture. Only difference is either static loading or cyclic loading. All experiments followed by imaging techniques. High speed camera or high resolution camera is used to follow the procedure. Each details of the experimental procedure will be explained in details in the next section.

3.1.6 Experimental Procedure

3.1.6.1 Fatigue Experiments

Fatigue experiments are performed under displacement control. Sinusoidal wave type cyclic loading is given at 2 Hz. R ratio is generally 0.5 but there are some exceptions. Details of the all experiments will be given in the results chapter. Fatigue experiments are performed up to cracking and corresponding stiffness degradation. If there is no cracking, experiment continued up to 1,000,000 cycle.

3.1.6.2 Static Experiments

All static experiments are conducted under displacement control at loading rate 1 mm/min. Specimens are loaded quasi-statically and images are captured according to experiment type at the cracking instant or at a constant time interval. Static experiments can be mentioned into three types. The first type is fast imaging experiments. In this type, experimental images are captured by high speed camera at rate 150,000 fps. These images are captured at cracking instant. At that moment when the cracking sound was heard images are captured by pushing trigger. The second type is high resolution images at 1 fps. 4-megapixel camera is settled at imaging rate 1 fps and capturing is started with the experiment at the same time. When the experiment is stopped, the image capturing is also stopped simultaneously. The third type is DIC experiments. Capturing the images are same as second type. Only difference is DIC paint with speckles on the specimen surface. Images are captured from the beginning of the experiment to the end. After the capturing is finished DIC post-process starts.

3.1.6.3 Summary of the Experiments

For four stacking sequences, $[0]_{30}$ UD, $[0_3/90_3/0_3/90_3/0_3]_s$ cross-ply, $[0_3/90_3/0_3]_s$ cross-ply and $[(45/0)_7, 45/45/0/45]$ fabric, static and fatigue experiments are conducted. List of the experiments is given in Table 4. Specimen names are created according to their specimen type. For example, $[0]_{30}$ specimens, 0 represents it has 0° stacking, t5 represents roughly the thickness of the specimen is equal to 5mm and final part represents the specimen number such as specimen 1 is s1 and it continues up to s10. For $[0_3/90_3/0_3/90_3/0_3]_s$ specimens they start with 90 and thickness 5mm and the specimen number. For $[0_3/90_3/0_3]_s$ the difference is thickness and it is roughly equal to

3 mm. For fabric specimens they start with first letter of fabric, f, and continued with thickness 5mm and specimen number. Totally 29 experiments are conducted. 15 of them are static and 14 of them are fatigue experiments.

Table 4. Summary of the experiments.

#	Micrograph	Stacking	Static exp.	Fatigue exp.	Static after fatigue exp.
1		[0]30 UD	0t5s2 0t5s4 0t5s6 0t5s8	0t5s3 0t5s5	-
2		[03/903/03/903/03]s UD	90t5s3 90t5s5	90t5s7 90t5s8 90t5s9 90t5s10	-
3		[03/903/03]s UD	90t3s2 90t3s3 90t3s4 90t3s7	90t3s5 90t3s6 90t3s8 90t3s9 90t3s10	90t3s8 90t3s10
4		[(45/0)7,45/45/0/45] fabric	ft5s2 ft5s3 ft5s4	ft5s5 ft5s6 ft5s7	-

3.1.7 Digital Image Correlation Method

Digital image correlation is an optical measurement technique to obtain the motion and deformation on an object surface. In this method, stochastic speckle patterns define discrete image areas called subsets and the grey value pattern in the subsets (marked in red in Figure 38) is followed during the deformation.

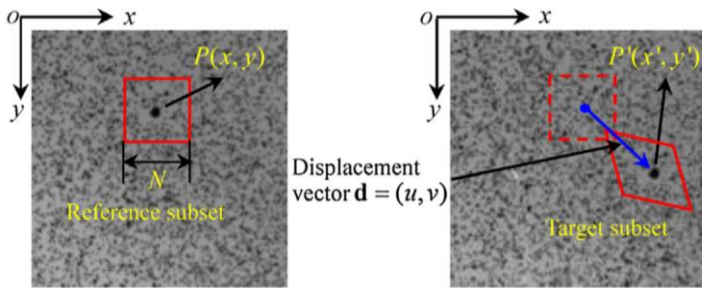


Figure 38. Undeformed and deformed images [49].

The principle of the DIC method is to track the same point in undeformed subset and the deformed subset. A ($N \times N$ pixels) square subset encloses the physical point in the undeformed image and is utilized to find the position of the same point in the deformed image by calculating the maximum correlation coefficient. The in-plane displacement vector is defined as the vector between the undefined subset center and the deformed subset center at a certain point $P(x,y)$. By moving the deformed subset via the searching subset and calculating correlation coefficient at each location, the correlation coefficient distribution is obtained [50].

In this research, DIC method is used to obtain strain field in the curved region before the failure. Two dimensional DIC experiments are conducted for four specimen types. Speckle pattern on the specimen surface is formed according to measured area. To obtain 25×18 mm measuring volume, 100 mm lens is used with 100 mm distance ring and the camera is positioned 435 mm away from the specimen. Shutter time is set to 5.638 ms. In the experiments, the specimens are loaded at a rate of 1mm/min and the images are captured. After the experiment, captured DIC images are analyzed by GOM DIC software ARAMIS. Analyses are performed at many subsets called as facets by the software. Facet size is determined as 15x15 pixel facets in accordance with the speckle pattern with a facet step of 12 pixels corresponds to a 3 pixel overlapping area.

3.2 Analytical Method

3.2.1 Calculation of Stresses due to Mechanical Load

Analytical stress analysis is applied to explain the crack initiation and growth mechanisms observed in the experiments by discussing the stress state in the curved region. The stress state is analytically calculated in the curved region using the multilayer curved beam solution. Lekhnitskii [39] and Ko & Jackson [51] solutions are examined and multilayer curved beam solution is applied to the present case.

Airy stress function is written for end forces P and for end moment.

For end load:

$$F = [Ar^{1+\beta} + Br^{1-\beta} + Cr + Drlnr]sin\theta + [A'r^{1+\beta} + B'r^{1-\beta} + C'r + D'rlnr]cos\theta$$

For end moment:

$$F = A' + B'r^2 + C'r^{1+k} + D'r^{1-k}$$

Stresses:

$$\sigma_r = \frac{1}{r} \frac{\partial F}{\partial r} + \frac{1}{r^2} \frac{\partial^2 F}{\partial \theta^2}$$

$$\sigma_\theta = \frac{\partial^2 F}{\partial r^2}$$

$$\tau_{r\theta} = - \frac{\partial^2}{\partial r \partial \theta} \left(\frac{F}{r} \right)$$

Stress-strain relations:

$$\varepsilon_r = \frac{1}{E_r} \sigma_r - \frac{v_{\theta r}}{E_\theta} \sigma_\theta$$

$$\varepsilon_\theta = - \frac{v_{r\theta}}{E_r} \sigma_r + \frac{1}{E_\theta} \sigma_\theta$$

$$\gamma_{r\theta} = \frac{1}{G_{r\theta}} \tau_{r\theta}$$

For plane strain E_r , E_θ , $v_{\theta r}$ and $v_{r\theta}$ should be replaced by the following expressions:

$$E'_r = \frac{E_r}{1 - v_{rz}v_{rz}}$$

$$E'_\theta = \frac{E_\theta}{1 - v_{z\theta}v_{\theta z}}$$

$$v'_{\theta r} = \frac{v_{\theta r}}{1 - v_{z\theta}v_{\theta z}} \left(1 + \frac{v_{rz}v_{\theta z}}{v_{\theta r}} \right)$$

$$v'_{r\theta} = \frac{v_{r\theta}}{1 - v_{zr}v_{rz}} \left(1 + \frac{v_{z\theta}v_{rz}}{v_{r\theta}} \right)$$

Strain-displacement relations:

$$\varepsilon_r = \frac{\partial u_r}{\partial r}$$

$$\varepsilon_\theta = \frac{1}{r} \frac{\partial u_\theta}{\partial \theta} + \frac{u_r}{r}$$

$$\gamma_{r\theta} = \frac{1}{2} \left(\frac{1}{r} \frac{\partial u_r}{\partial \theta} + \frac{\partial u_\theta}{\partial r} - \frac{u_\theta}{r} \right)$$

Stresses for end load case:

$$\sigma_r(r, \theta) = [A\beta r^{\beta-1} - B\beta r^{-\beta-1} + D/r] \sin\theta$$

$$\sigma_\theta(r, \theta) = [A\beta(1+\beta)r^{\beta-1} - B\beta(1-\beta)r^{-\beta-1} + D/r] \sin\theta$$

$$\tau_{r\theta} = -[A\beta r^{\beta-1} - B\beta r^{-\beta-1} + D/r] \cos\theta$$

Anisotropic parameter:

$$\beta = \sqrt{1 + \frac{E_\theta}{E_r} + (1 - 2v_{r\theta}) + \frac{E_\theta}{G_{r\theta}}}$$

Stresses for moment case:

$$\sigma_r(r, \theta) = 2B' + C'(1+k)r^{k-1} + D'(1-k)r^{-k-1}$$

$$\sigma_\theta(r, \theta) = 2B' + C'k(1+k)r^{k-1} - D'k(1-k)r^{-k-1}$$

$$\tau_{r\theta} = 0$$

Anisotropic parameter:

$$k = \sqrt{E_\theta/E_r}$$

Displacements:

For end force:

$$u_r(r, \theta) = \left\{ Ar^\beta \left[\frac{1}{E_r} - (1+\beta) \frac{v_{\theta r}}{E_\theta} \right] + Br^{-\beta} \left[\frac{1}{E_r} - (1-\beta) \frac{v_{\theta r}}{E_\theta} \right] + D(lnr) \left(\frac{1}{E_r} - \frac{v_{\theta r}}{E_\theta} \right) \right\} \sin\theta$$

$$u_\theta(r, \theta) = \left\{ Ar^\beta \left[\frac{1}{E_r} - \beta(1+\beta) \frac{1}{E_\theta} - \frac{v_{\theta r}}{E_\theta} \right] + Br^{-\beta} \left[\frac{1}{E_r} + \beta(1-\beta) \frac{1}{E_\theta} - \frac{v_{\theta r}}{E_\theta} \right] + D \left[(lnr) \left(\frac{1}{E_r} - \frac{v_{\theta r}}{E_\theta} \right) - \left(\frac{1}{E_\theta} - \frac{v_{\theta r}}{E_\theta} \right) \right] \right\} \cos\theta$$

For moment:

$$u_r(r) = B' \left\{ 2r \left(\frac{1}{E_r} - \frac{v_{\theta r}}{E_\theta} \right) \right\} + C' \left\{ (1+k)r^k \left(\frac{1}{k} \frac{1}{E_r} - \frac{v_{\theta r}}{E_\theta} \right) \right\} - D' \left\{ (1-k)r^{-k} \left(\frac{1}{k} \frac{1}{E_r} - \frac{v_{\theta r}}{E_\theta} \right) \right\}$$

To find out arbitrary constants boundary conditions are used. Two anisotropy constants k and β are as follows. After stresses are written in terms of arbitrary constants, boundary conditions are applied and final solution equations are obtained for each layer of the curved beam. Stress functions have 3 unknowns for the end moment and the end force cases. For N layer curved composite beam, $3N$ unknowns must be determined. By using boundary conditions at inner, outer and interlaminar surfaces and load application location, stress matrix is solved and all arbitrary constants are figured out.

Boundary conditions: at each interface continuities of stresses and displacements must be satisfied as follows:

$$\sigma_r^i(a_i, \theta) = \sigma_r^{i+1}(a_i, \theta)$$

$$\tau_{r\theta}^i(a_i, \theta) = \tau_{r\theta}^{i+1}(a_i, \theta)$$

$$u_r^i(a_i, \theta) = u_r^{i+1}(a_i, \theta)$$

$$u_\theta^i(a_i, \theta) = u_\theta^{i+1}(a_i, \theta)$$

At inner ($i = 1$) and outer($i = N$) free surfaces σ_r and $\tau_{r\theta}$ equal to zero.

Force equality for end force:

$$-P = \sum_{i=1}^N \int_{a_{i-1}}^{a_i} \tau_{r\theta}^i(r, 0) dr$$

Force equality for moment:

$$-M = \sum_{i=1}^N \int_{a_{i-1}}^{a_i} (r - r_0) \sigma_\theta(r) dr$$

3.2.2 Calculation of Stresses due to Thermal Load

Change in temperature leads to change in strain for materials. Fiber reinforced composite materials also show this change. Strain created by change in temperature is defined by the coefficient of thermal expansion. Thermal expansion coefficient is a material constant and defined for each principal material direction. For laminated composites two constant coefficients are defined as, α_1 coefficient of thermal expansion in the fiber direction and α_2 coefficient of thermal expansion in the perpendicular direction to the fibers.

Calculation of thermal stress resultants is explained below step by step.

Transformation of thermal coefficients to laminate coordinate system is as follows:

$$\begin{bmatrix} \alpha_x \\ \alpha_y \\ \alpha_{xy} \end{bmatrix} = \begin{bmatrix} \cos^2 \theta & \sin^2 \theta & -2\sin\theta\cos\theta \\ \sin^2 \theta & \cos^2 \theta & 2\sin\theta\cos\theta \\ \sin\theta\cos\theta & -\sin\theta\cos\theta & \cos^2 \theta - \sin^2 \theta \end{bmatrix} \begin{bmatrix} \alpha_1 \\ \alpha_2 \\ 0 \end{bmatrix}$$

Thermal strains for each lamina are:

$$\varepsilon_x^T = \alpha_x \Delta T$$

$$\varepsilon_y^T = \alpha_y \Delta T$$

$$\varepsilon_{xy}^T = \frac{\gamma_{xy}^T}{2} = \alpha_{xy} \Delta T$$

Thermal stress resultants are calculated just like mechanical calculations:

$$\begin{bmatrix} N_x^T \\ N_y^T \\ N_{xy}^T \end{bmatrix} = \sum_{k=1}^n \begin{bmatrix} \overline{Q_{11}} & \overline{Q_{12}} & \overline{Q_{16}} \\ \overline{Q_{12}} & \overline{Q_{22}} & \overline{Q_{26}} \\ \overline{Q_{16}} & \overline{Q_{26}} & \overline{Q_{66}} \end{bmatrix}_k \begin{bmatrix} \varepsilon_x^T \\ \varepsilon_y^T \\ \gamma_{xy}^T \end{bmatrix}_k (h_k - h_{k-1})$$

Thermal strains are combined for each layer of the laminate. Typical thermal expansion coefficients for carbon/epoxy is given in [47] as, $\alpha_1 = -0.072 * 10^{-6} 1/^{\circ}F$ and $\alpha_2 = 32.4 * 10^{-6} 1/^{\circ}F$. These coefficient values are used for thermal calculations in this thesis.

3.3 Finite Element Method

Finite element model is generated to validate the analytical results. 2D Non-linear static finite element analyses are performed in ABAQUS/Standard. Composite model is divided to sections as number of plies and steel bolts are added to the end of the arms as in the test fixture as seen in Figure 39. For four cases (UD [0]₃₀, cross-ply [0₃/90₃/0₃/90₃/0₃]_s, cross-ply [0₃/90₃/0₃]_s and woven [(45/0)₇,45/45/0/45]) finite element models are created and stress results at the curved section are compared with analytical results.

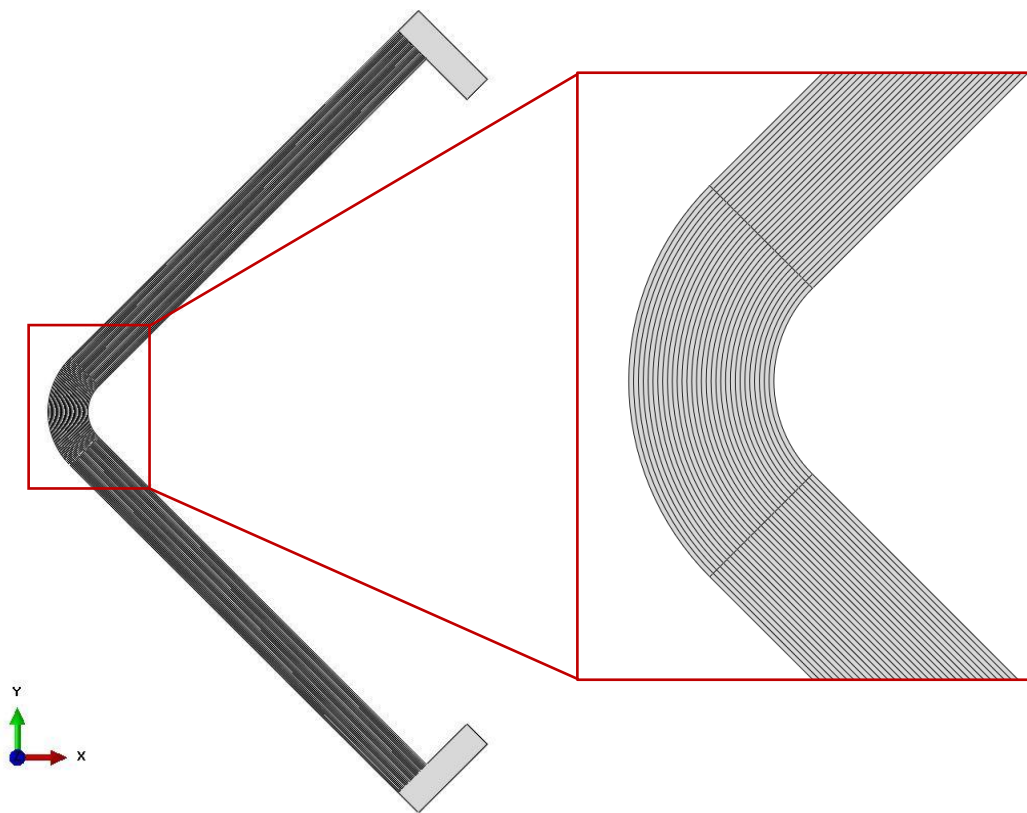


Figure 39. FEM geometry visualization.

The load is applied vertically (y-axis) at the upper arm to the mid-node in the edge. For four cases (UD [0]₃₀, cross-ply [0₃/90₃/0₃/90₃/0₃]_s, cross-ply [0₃/90₃/0₃]_s and woven [(45/0)₇,45/45/0/45]) applied loads are different and equal to 1200 N, 800 N, 400 N and 800 N respectively. The loads are chosen from the experiments as failure loads and also used in the analytical solution. The boundary condition is applied at the

lower arm by considering the experimental setup. Displacements are fixed to zero in both directions and rotation is free. Constraints are applied to one node as shown in Figure 40.

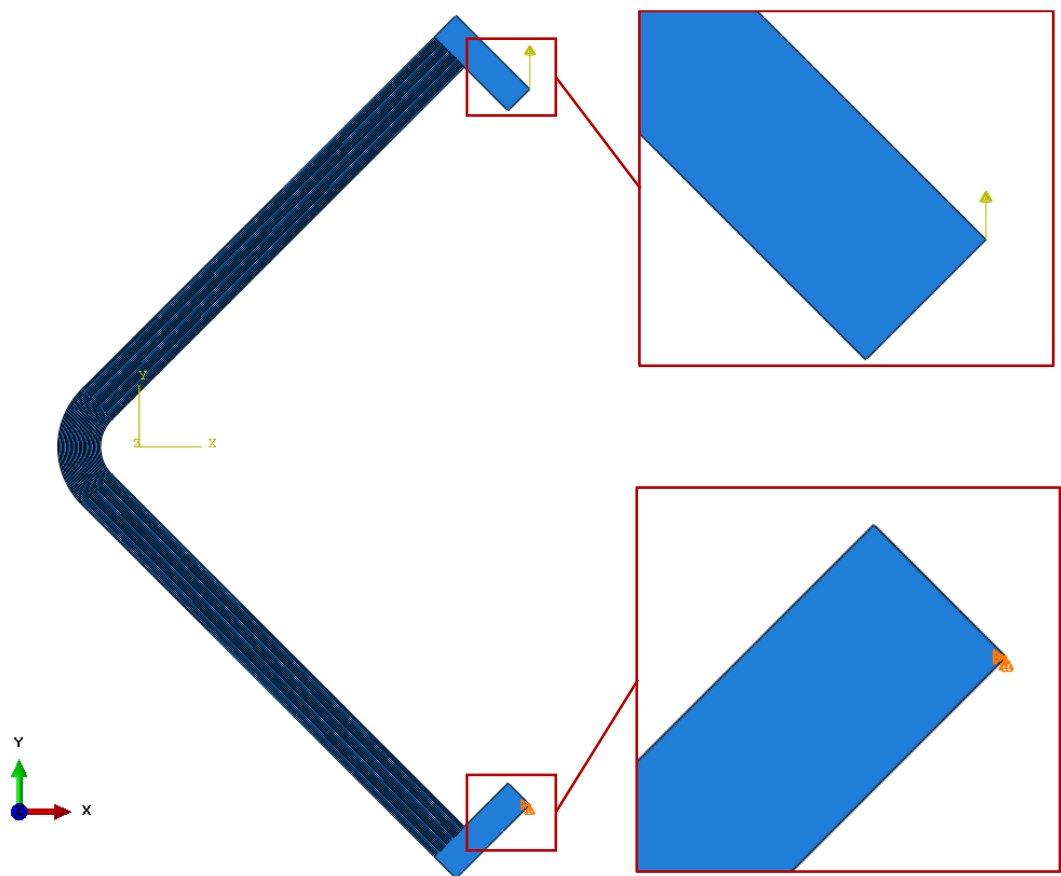


Figure 40. Load application and boundary condition.

In the analyses 4-node bilinear plane strain quadrilateral elements are used with reduced integration. Analyses are performed with 2 and 4 elements in each layer as seen in Figure 41 and radial stress results are extracted. There is a slight difference between 2 and 4 element cases as seen in Figure 42. Therefore, all analyses are performed with 2 elements in each layer.

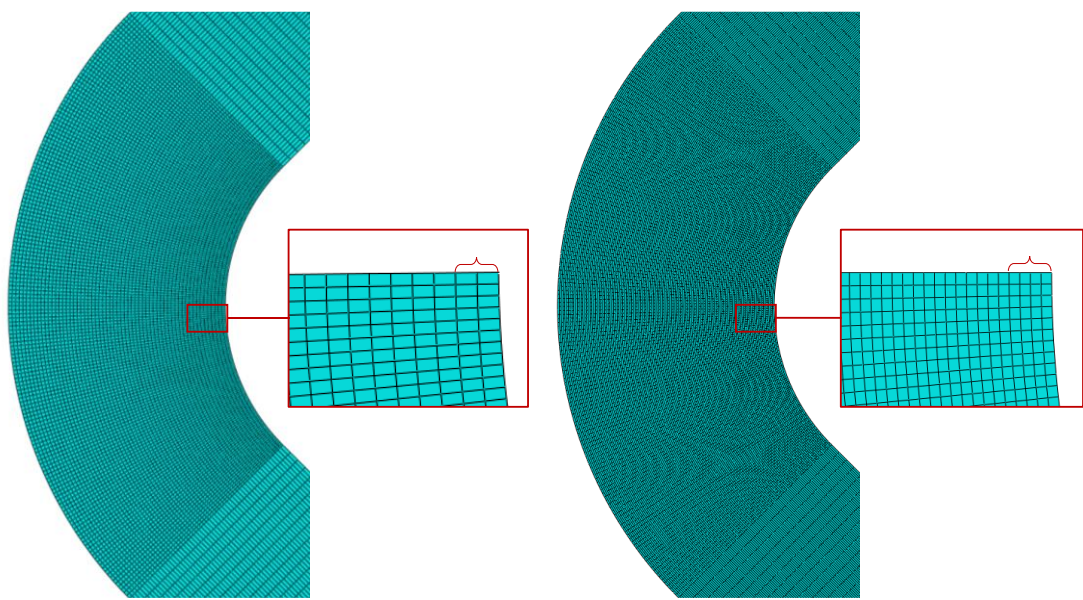


Figure 41. Mesh visualization on FEM.

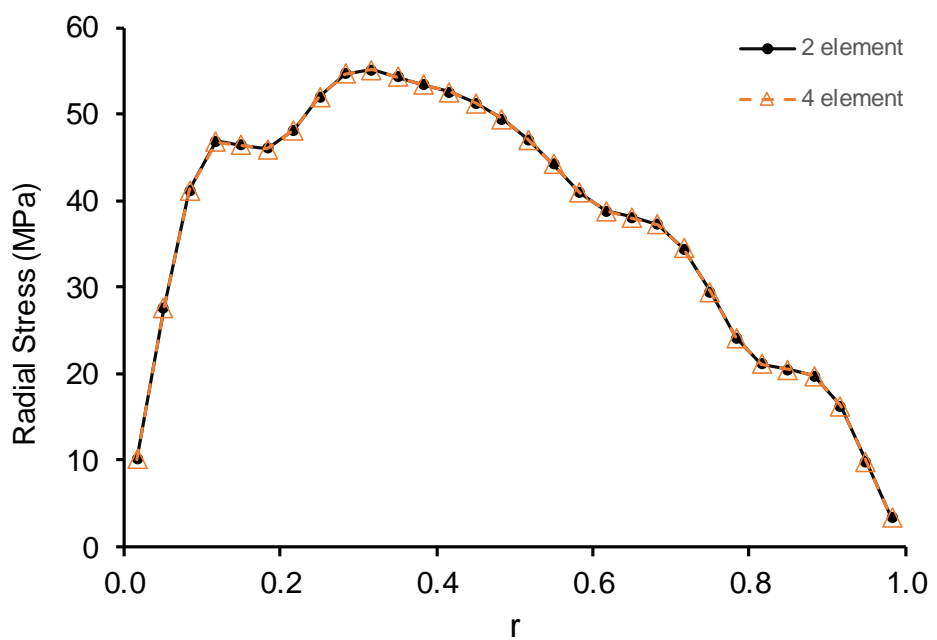


Figure 42. Difference between the analyses with 2 and 4 elements for each ply.

CHAPTER 4

UD LAMINATES

In this chapter, experimental results of curved UD laminates under static loading (Section 4.1.1) and under fatigue loading (Section 4.1.2) are presented. Experimental results sections are followed by analytical and finite element results sections. For each case; load-displacement curves including failure, post-failure images and micrographs of the failed specimen are presented. For the static experiments, DIC results showing the strain distributions in the curved region are also presented.

4.1 Experimental Results of UD Curved Laminates

4.1.1 Static Tensile Tests of UD Curved Laminates

Static experiments are conducted on four [0]₃₀ UD specimens cut from the same composite batch. One specimen (0t5s2) is used to conduct DIC experiment and three specimens (0t5s4, s6 and s8) are used in experiments recorded with a high resolution camera. All specimens are loaded quasi-statically under displacement control at a displacement rate of 1 mm/min and images are captured at 1fps. Experiments are conducted at approximately 25°C laboratory temperature.

Load-displacement curves of four [0]₃₀ specimens under static loading are given below in Figure 43 (a). Slopes of the curves are very close to each other approximately up to 4-5 mm displacement. A nonlinearity in the load-displacement curve before failure is observed which is a problem common to UD laminates. During the drilling operation, cracks are formed around holes due to inappropriate drilling conditions. These cracks propagated to the end of the specimen arm while mounting the specimen to the test fixture due to the lack of fibers in the transverse direction as shown in Figure 44.

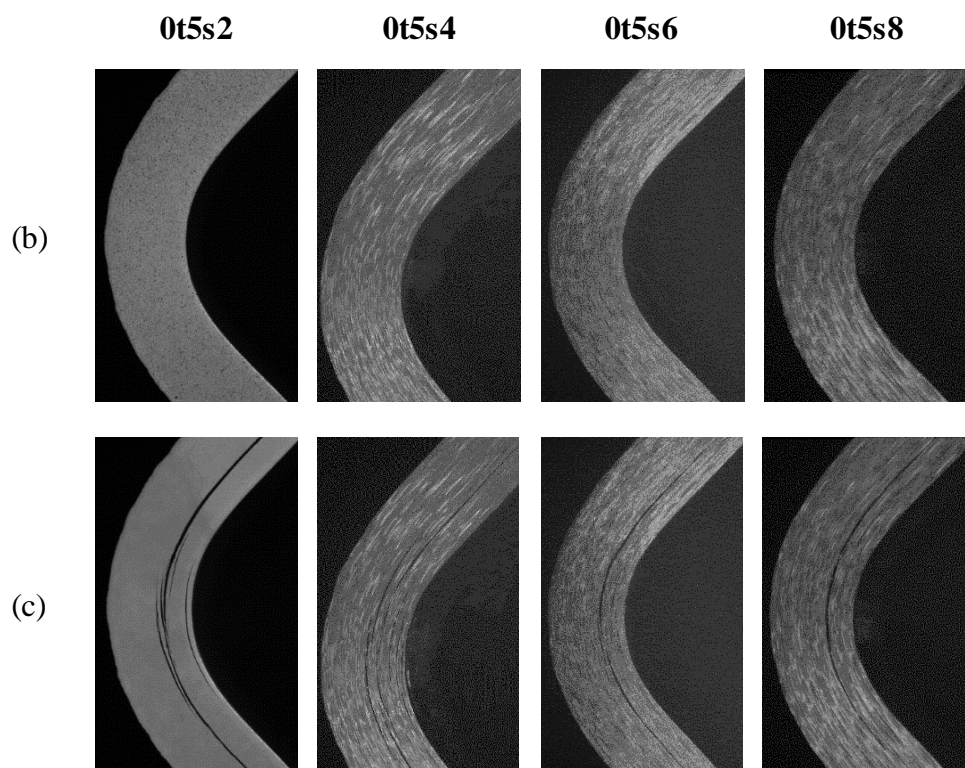
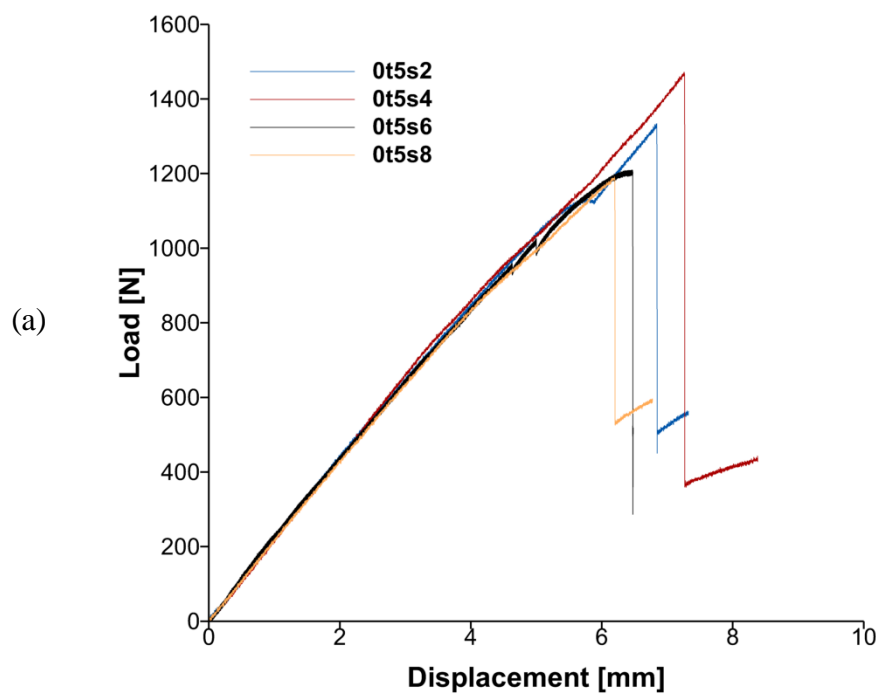


Figure 43. (a) Load-displacement curves, pictures of the specimens (b) before failure and (c) after failure.



Figure 44. Crack occurred at mounting the specimen.

We decided to continue the test since these conditions do not affect our boundary conditions and this region is far away from the curved region which is the main consideration of this thesis. However, the cracks between the hole and the end of the specimen arm cause non-linear behavior as the load is increased. This non-linear behavior before failure is only observed in UD laminates due to the lack of fibers in the transverse direction.

Captured pre and post failure images of the specimens are presented in Figure 43 (b) and (c). Single cracks are observed in all specimen except s2 and s4 where multiple cracks are formed. Failure locations of the major cracks are very close and approximately at 35% of the thickness from inner radius. In Table 5, details of static experiments are listed; the number of cracks, location of the major crack, critical load and displacement, the stiffness before and after the failure and the residual load and displacement. Stiffness values are very close to each other in elastic region and stiffness values after the failure shows that multiple cracks leads to larger stiffness reduction as expected from beams with smaller thicknesses.

Table 5. Summary table for static experiments of UD specimens.

Spc Name	# of cracks	Location of major crack	P _c (N)	δ _c (mm)	Stiffness (N/mm)	P _r (N)	2 nd stiffness (N/mm)	δ _r at P=0 (mm)
0t5s2	2	0.34R	1334	6.8	221	450	116	1.16
0t5s4	4	0.44R	1467	7.26	220	359	59	1.62
0t5s6	1	0.34R	1200	6.47	219	498	102	-
0t5s8	1	0.34R	1184	6.2	214	529	106	1.17

DIC method is used to attain stress distribution in the specimen just before the failure. The specimen, 0t5s2, is loaded at a rate of 1mm/min. As seen in Figure 43 (a), the failure occurs at 6.8 mm displacement which corresponds to a load of 1334 N. The failure type is delamination seen in Figure 43 (c) and leads to a significant load drop to 450 N.

Failure occurs very fast in micro seconds level so 1fps imaging does not provide delamination initiation and propagation steps. In this experiment, two different delamination are observed in the specimen. Major delamination is observed at 33% of the thickness from the inner radius which is roughly maximum radial stress location and minor delamination is observed at the interface between 1st and 2nd layers. This minor delamination is not expected usually. It may be caused by an initial defect in the specimen due to manufacturing imperfections.

The change in Tresca strain field, effective shear strain, in the curved specimen during the DIC experiment is shown in Figure 45. In the figure, DIC images are taken once every minute and the last two images are at the cracking instant just before and after the failure.

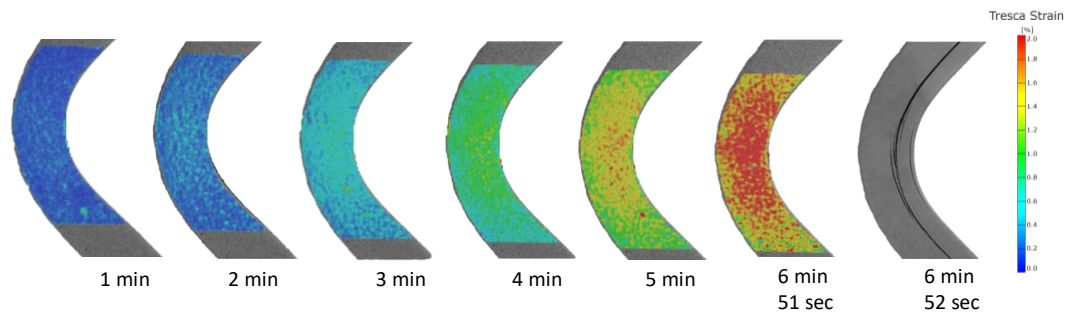


Figure 45. Change of Tresca strain distribution in the specimen (0t5s2) with time up to failure.

In Figure 46, the Tresca strain fields in the specimen are represented in conjunction with the load-displacement curve. Strain concentrations in the middle section of the curve start to become visible at 6 mm displacement.

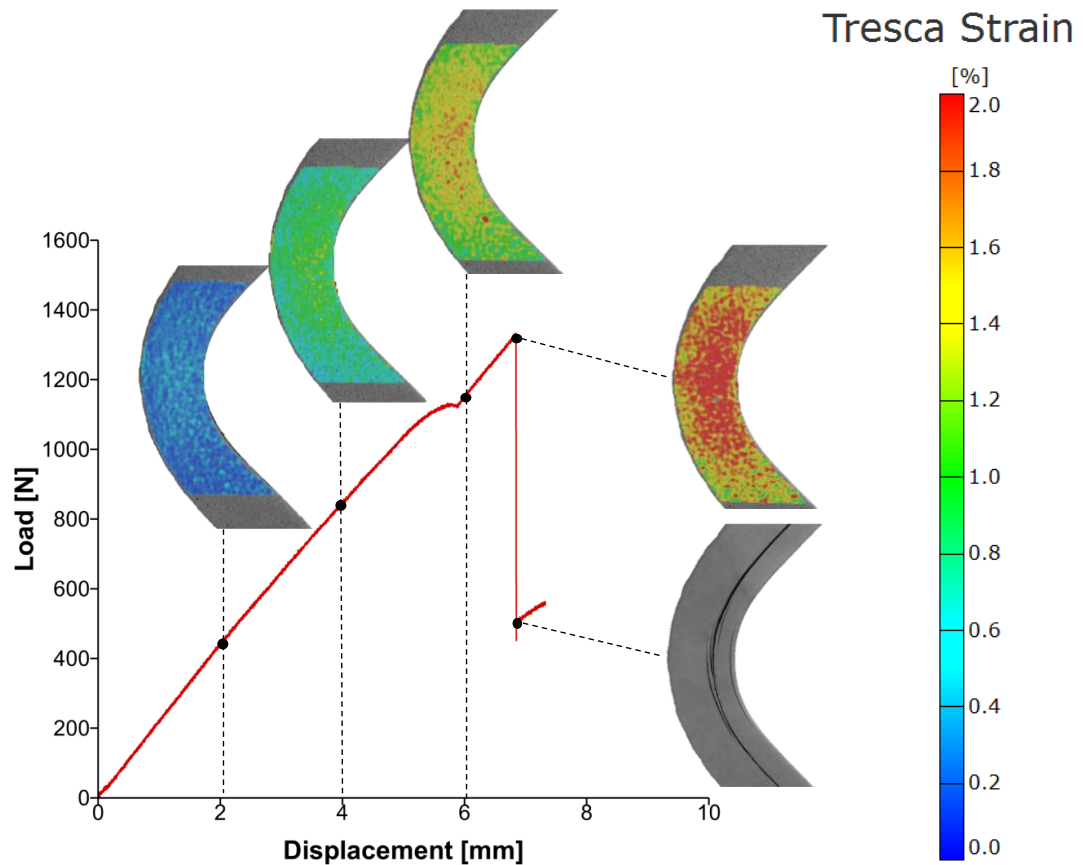


Figure 46. Representation of change in Tresca strain in the specimen (0t5s2) on load-displacement curve.

Detailed examination of the Tresca strain distribution in the specimen just before the failure is as shown in Figure 47. The pre-failure strain field is fitted on the post-failure image at the right hand side of the figure. The delamination failure occurs in the region of the strain concentrations.

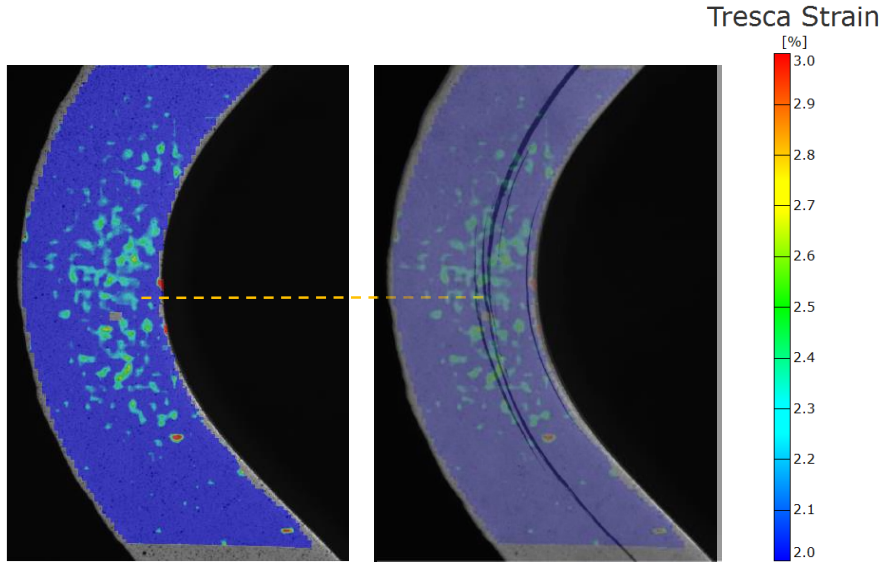


Figure 47. Tresca strain distribution just before the failure and its representation on the specimen picture just after the failure.

4.1.2 Fatigue Tests of UD Curved Laminates

For two $[0]_{30}$ UD specimens cut from the same composite batch, 0t5s3 and s5, fatigue experiments are conducted. Both fatigue experiments are performed under displacement control between 2-4 mm (66% of the critical displacement of the static experiments) and sinusoidal wave type cyclic loading is given at 2 Hz. While the former is terminated at 1,000,000 cycle without failure, the latter is terminated at 40,000 cycles with failure. The load-displacement behavior during the test and the load-displacement parameters as a function of the number of cycles are shown in Figure 48 (a) and (b), respectively. In Figure 48 (c), image of the specimen 0t5s5 after the failure is given. The crack is located at 33% of the thickness from the inner radius as a single major delamination.

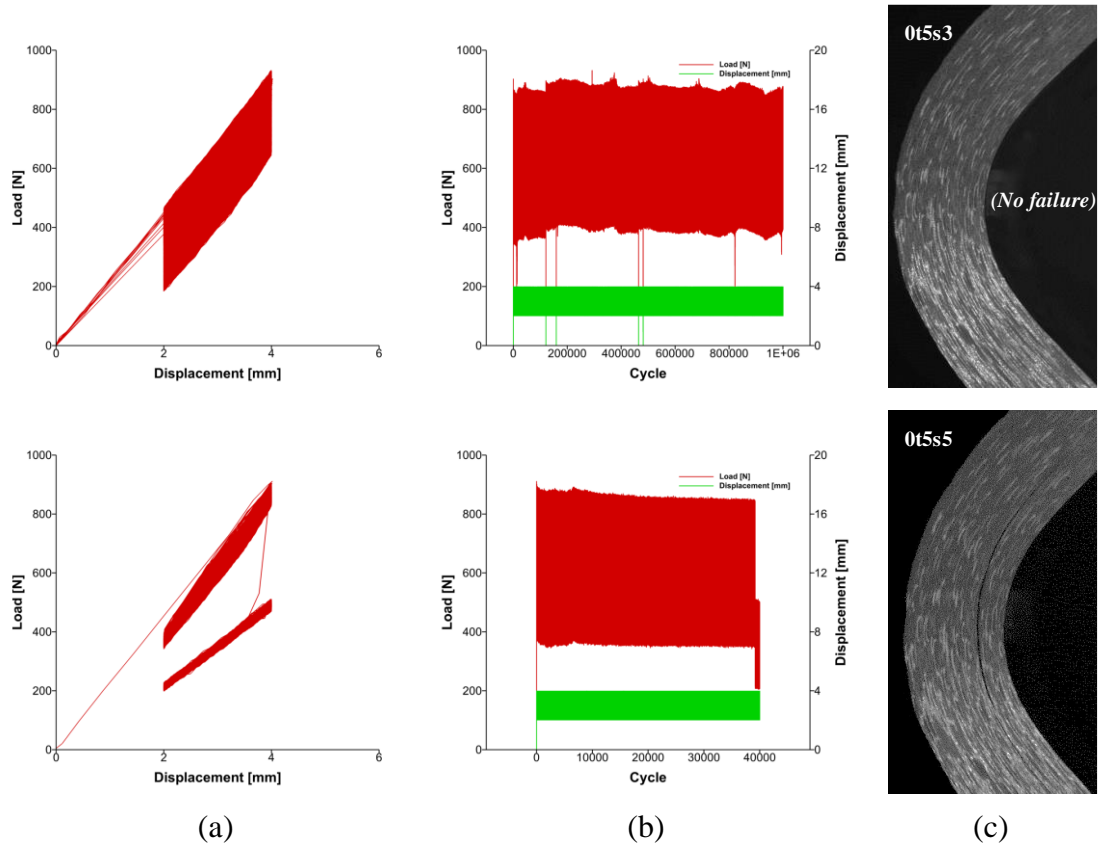


Figure 48. (a) Load-displacement curves, (b) load-cycle-displacement curves and (c) pictures of the specimens after the failure.

In Figure 48, it is observed that the load drops to zero six times during the test for the specimen 0t5s3. This is caused by the power outage that occurred 6 times during the duration of the fatigue experiment. In addition to sharp load drops, there are also visible rises and falls in the maximum and minimum loads. In order to understand whether these rises and falls lead to stiffness degradation in the specimen or not, maximum and minimum loads are separated for each cycle and difference is plotted in Figure 49.

The stiffness graphs of both specimens are plotted in the logarithmic scale by dividing the load difference to displacement difference (2 mm). As clearly seen in Figure 50, stiffness reduction is not observed. The stiffness value is 245 ± 5 N/mm for the intact specimens and it reduced to 180 N/mm for failed specimen.

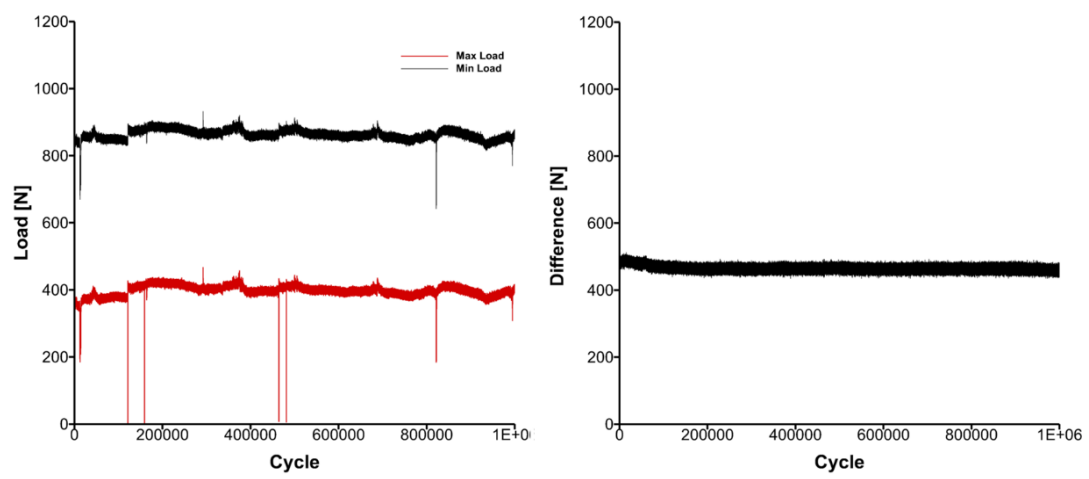


Figure 49. Maximum and minimum loads during the fatigue loading and the differences for specimen 0t5s3.

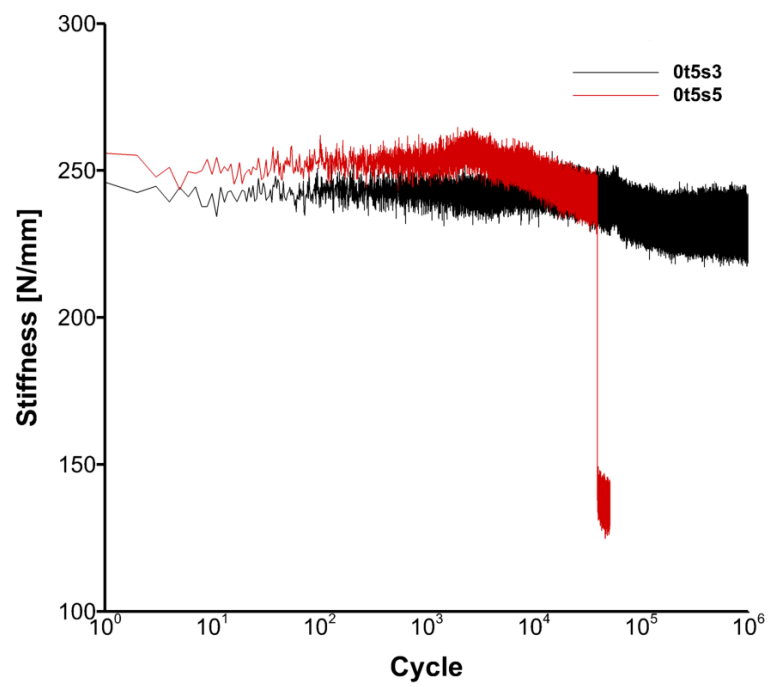


Figure 50. Change in stiffness with cycles.

For the specimen 0t5s5, temperature is also recorded using a digital thermometer during the experiment (details in Appendix-D. USED MACHINES AND FUNCTIONS). The graph of temperature and load change with time is given in Figure 51. Duration of the experiment is approximately 6 hours and temperature data is recorded. In the first hour, there is a clear temperature drop of approximately 2 °C which corresponds to 2.5% increase (approximately 20 N) in the load. This shows that the load is directly sensitive to the temperature change of even 2-4°C, this effect is more pronounced for cross-ply thin specimen in Section 5.1.2.1.

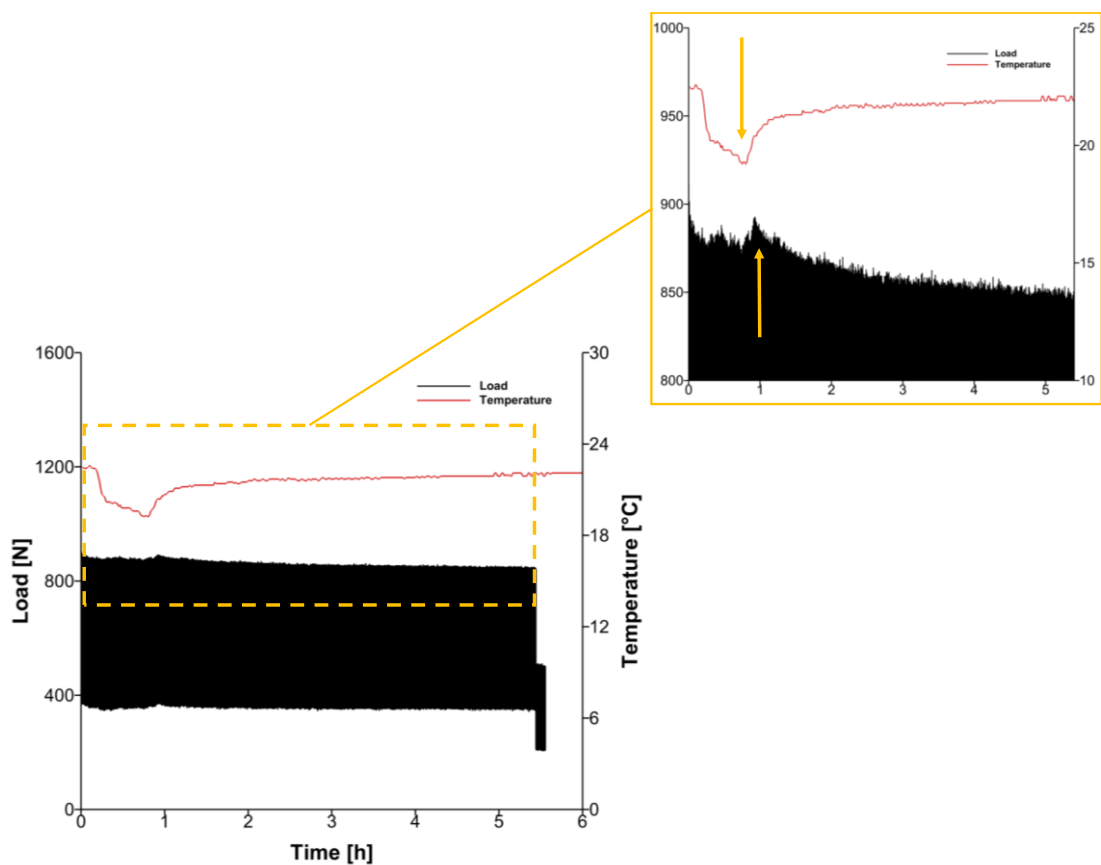


Figure 51. Load and temperature change with time for the specimen 0t5s5 and the close-up view.

4.2 Analytical Results of UD Curved Laminates

To understand the reason of the experimentally observed crack initiation location, analytical calculations are applied to the curved region for $[0]_{30}$ UD specimen. Analytical calculations are performed based on the multilayer curved beam solution explained in the analytical method section and the prescribed force is 1200 N in the vertical direction as in the experimental setup. Stress distributions are examined through the thickness direction at 0° , 15° , 30° and 45° sections of the curve as shown in Figure 52. For these sections radial, tangential and shear stress distributions are compared through the normalized thickness.

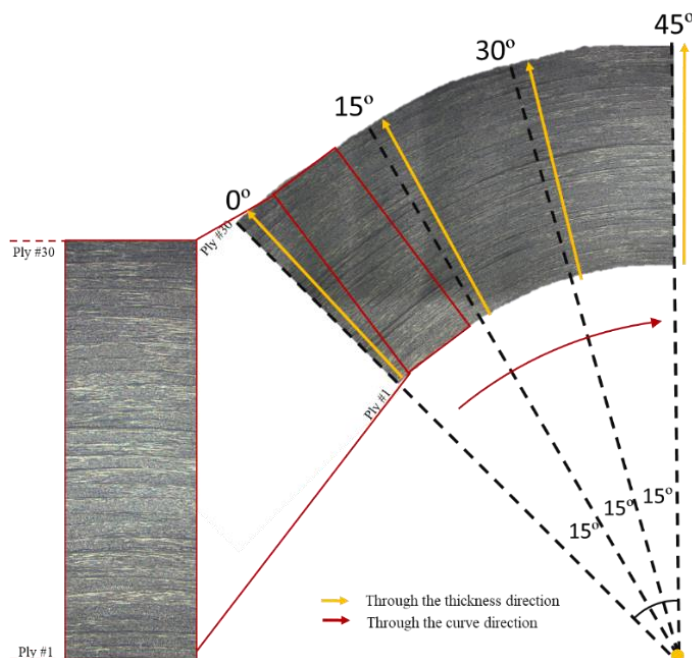


Figure 52. Representation of directions and sections used for stress distribution calculations on $[0]_{30}$ curved specimen.

Comparison of radial, tangential and shear stresses at 0° , 15° , 30° and 45° sections are given in Figure 53. Larger difference as percentage is observed in the shear stress. However, it should be noted that the magnitude of shear stress is much smaller than the radial and tangential stresses.

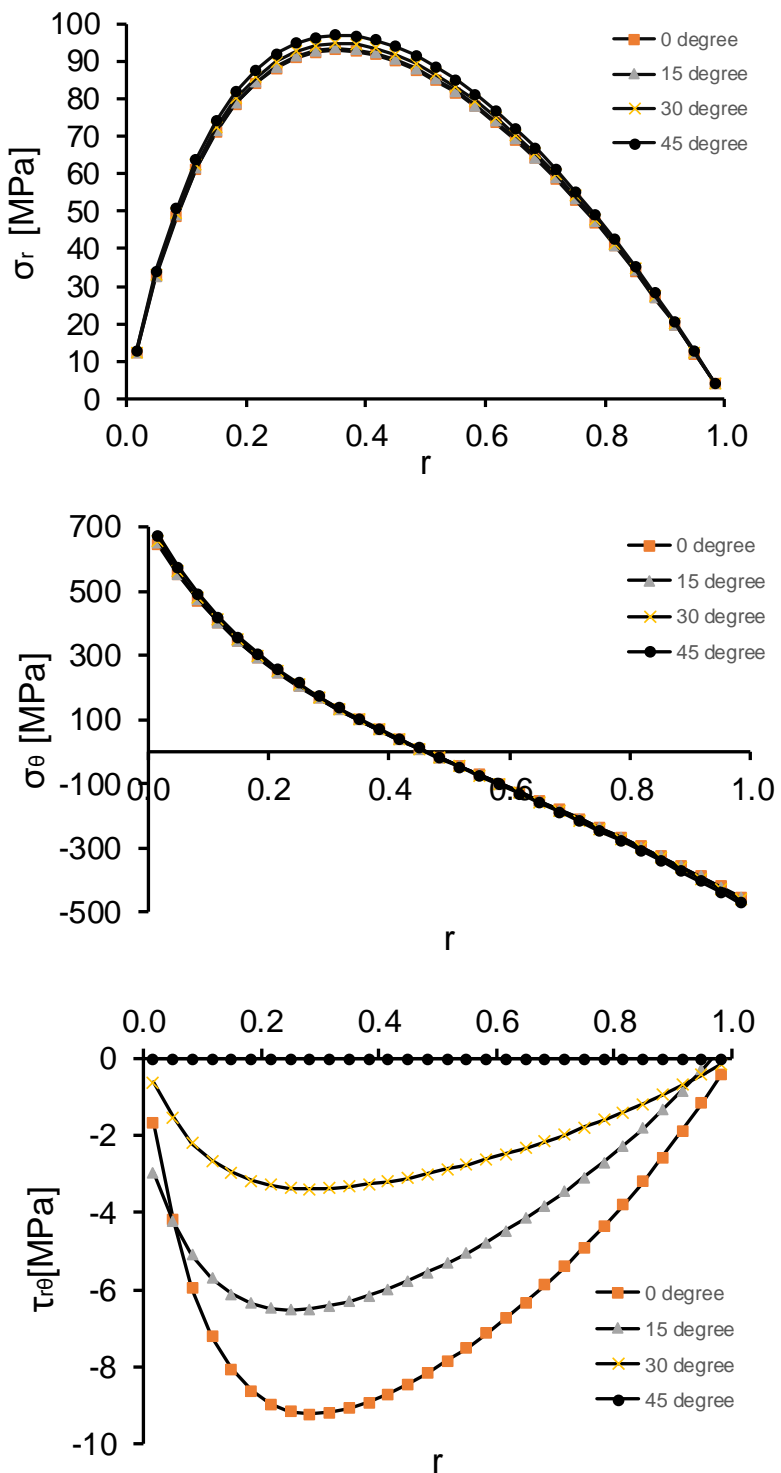


Figure 53. Radial, tangential and shear stress distributions through the thickness direction.

4.3 Finite Element Results of UD Curved Laminates

For $[0]_{30}$ UD specimen, finite element analysis is performed under 1200 N axial loading as described in finite element method section. Stress fields are given below in Figure 54 for radial, tangential and shear stresses in the curved region, respectively. The radial stress is concentrated at approximately 35% of the thickness and the maximum radial stress is observed at 11th layer as 84 MPa. The tangential stress is tensile at the inner radius of the curve while it is compressive at the outer radius of the curve as expected. The shear stress is zero at the center of the curve due to symmetric loading and increases through the arms.

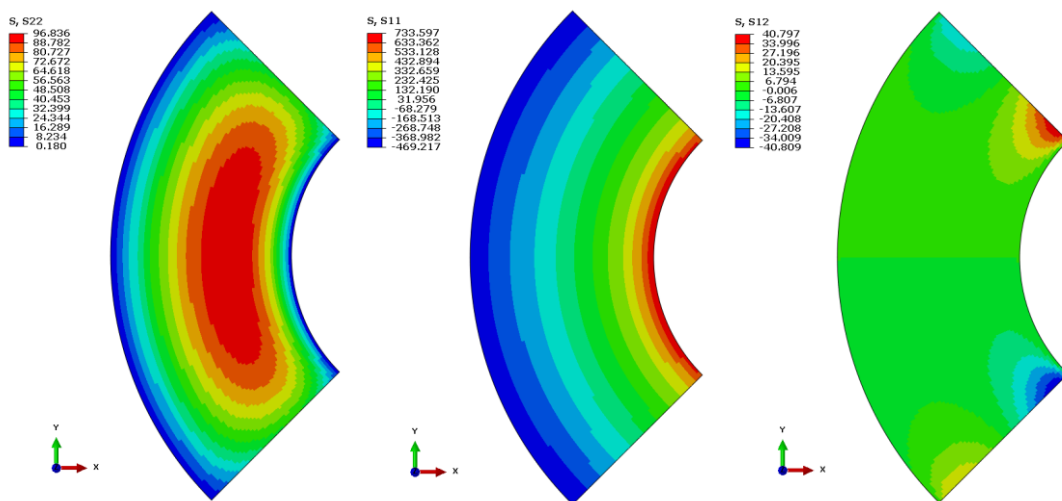


Figure 54. Radial, tangential and shear stress distributions on the curved region respectively for $[0]_{30}$ UD lay-up.

Finite element results are compared with analytical results in order to validate the analytical method. Comparison graphs for radial and tangential stresses at the center of the curve are shown in Figure 55. A slight difference is observed between FEA and analytical solution with an error less than 1% for the radial stress and less than 3% for the tangential stress.

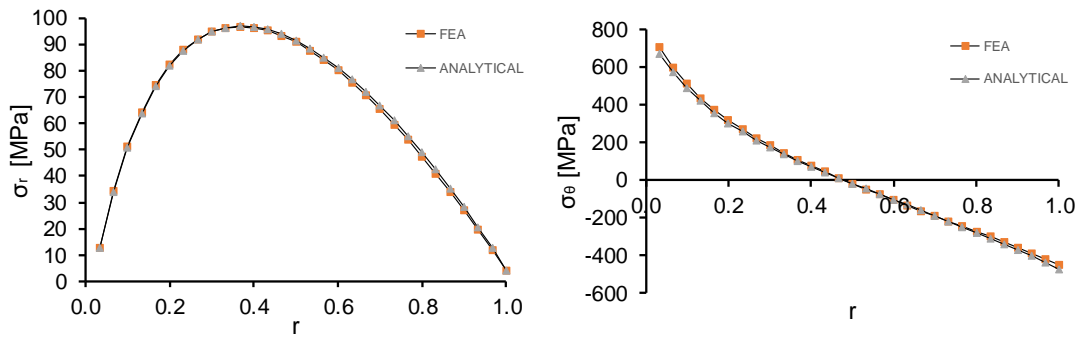


Figure 55. Comparison of FEA and analytical solution for radial and tangential stress distributions through the thickness at the center of the curve for $[0]_{30}$ UD lay-up.

Since the main concern of the FEA is to attain stress values in curved region before the failure, load drop is not simulated for this study. Critical load corresponding to the applied displacement is obtained from experimental results and used as prescribed force value to simulate the same linear load-displacement behavior until failure. Load-displacement curves of the experiments and the non-linear static finite element analysis are consistent up to 4 mm displacement as seen in Figure 56.

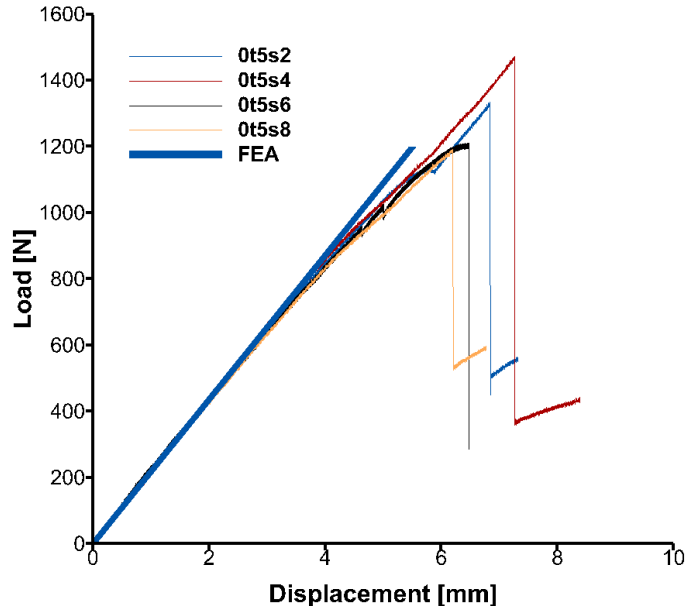


Figure 56. Load-displacement graph for experiments and FEA.

CHAPTER 5

CROSS-PLY LAMINATES

In this chapter, experimental results of thin and thick curved cross-ply laminates under static loading (Section 5.1.1) and fatigue loading (Section 5.1.2) are presented. Experimental results sections are followed by analytical and finite element results sections for thin and thick cross-ply specimens separately. For each case; load-displacement curves including failure, post-failure images and micrographs of the failed specimen are presented. For the static experiments, DIC results showing the strain distributions in the curved region are also presented. For all tests, in order to isolate and clarify the failure mechanisms of the curved CFRP composite specimens, 90° and 0° layers are grouped together to create thicker plies of each orientation.

5.1 Experimental Results of Cross-Ply Curved Laminates

5.1.1 Static Tensile Tests of Cross-Ply Curved Laminates

5.1.1.1 Thin Cross-Ply Curved Laminates

Six thin [0₃/90₃/0₃]_s curved specimens cut from the same composite batch are tested under static loading to failure. One specimen (90t3s2) is used to conduct DIC experiment, one specimen (90t3s7) is used in high speed camera experiment and four specimens (90t3s3, s4, s8 and s10) are used in experiments recorded with a high resolution camera. All specimens are loaded quasi-statically under displacement control at a displacement rate of 1 mm/min and images are captured at 1fps.

Load-displacement curves of six thin [0₃/90₃/0₃]_s specimens are shown in Figure 57 (a). Although the stiffness values and failure loads of each specimen vary slightly, they are very close to each other. Thus, the overall behavior of all specimens are consistent. Failure load is approximately 430±10 N and stiffness is 36±1 N/mm. After the failure,

load is seen to drop to 180 ± 10 N for four specimens and to 90 ± 10 N for two specimens, s8 and s2.

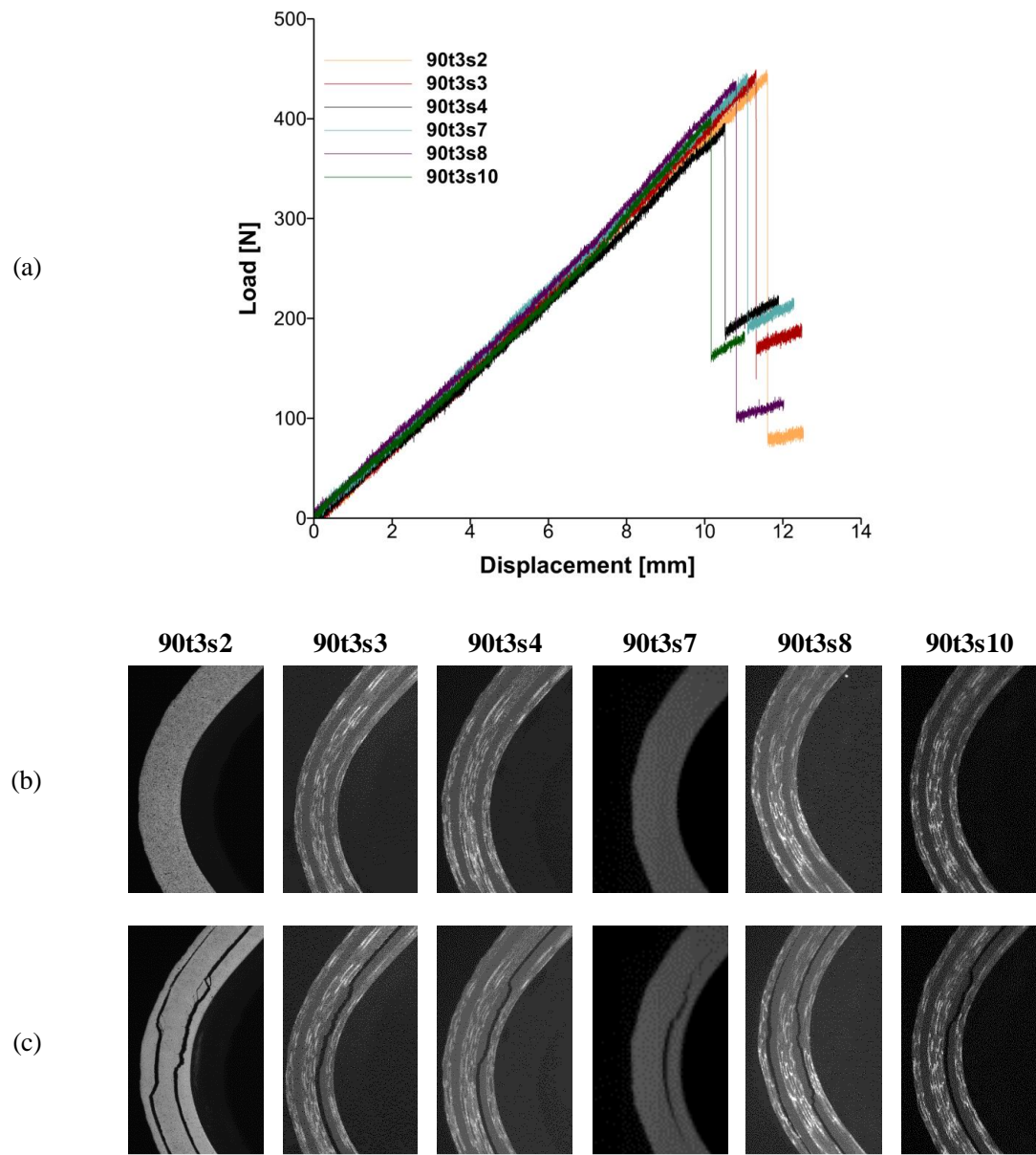


Figure 57. (a) Load-displacement curves, pictures of the specimens (b) before failure and (c) after failure.

Captured pre and post failure images of the specimens are presented in Figure 57 (b) and (c). The failure mechanism is observed to be a single dominant crack in the inner 0/90 interface for the four specimens as seen in post-failure images. However, the failure consists of an outer crack in addition to the inner crack for specimens s8 and s2 causing a larger load drop. The second crack initiated after the first crack [26], [52] and is considered to have secondary effects on the initial failure. The inner crack is observed in all cases and is the governing mechanism leading to loss of load carrying capacity that is the reason why we will concentrate only on the inner crack.

In Table 6, details of static experiments are given such as the number of cracks, location of the major crack, the critical load and displacement values, the stiffness before and after the failure and the residual load and displacement values. Observed crack locations are always the same. Two experiments, 90t3s2 and 90t3s8, are very close to each other in terms of residual load and 2nd stiffness values and the other four experiments are also similar between each other.

Table 6. Summary table for static experiments of thin cross-ply specimens.

Spc Name	# of cracks	Location of crack	P _c (N)	δ _c (mm)	Stiffness (N/mm)	P _r (N)	2 nd stiffness (N/mm)	δ _r at P=0 (mm)
90t3s2	1	0.33R	444	11.6	36	89	9	1.57
90t3s3	1	0.33R	440	11.3	37	171	15	1.57
90t3s4	1	0.33R	393	10.5	36	182	23	0.38
90t3s7	1	0.33R	444	11.1	36	186	19	0.61
90t3s8	1	0.33R	437	10.8	38	104	11	1.07
90t3s10	1	0.33R	400	10.2	35	161	23	1.3

In all post-failure images shown in Figure 57 (c), intralaminar matrix cracks in 90° group of layers and delamination at the interface of 0°and 90° layers are observed

clearly. Matrix cracks are observed to occur unsymmetrically either on the upper or lower side of the curve and continue as delamination through the arms. A more detailed examination of the cracks is carried out by using digital microscope after the failure. To discuss our observations, the curved region is divided into 15° sections shown in Figure 58 on a virgin specimen. 45° section represents the middle section of the curve (the symmetry plane-A). Right and left sections of the curved region are assumed to be symmetric due to applied symmetric loading.

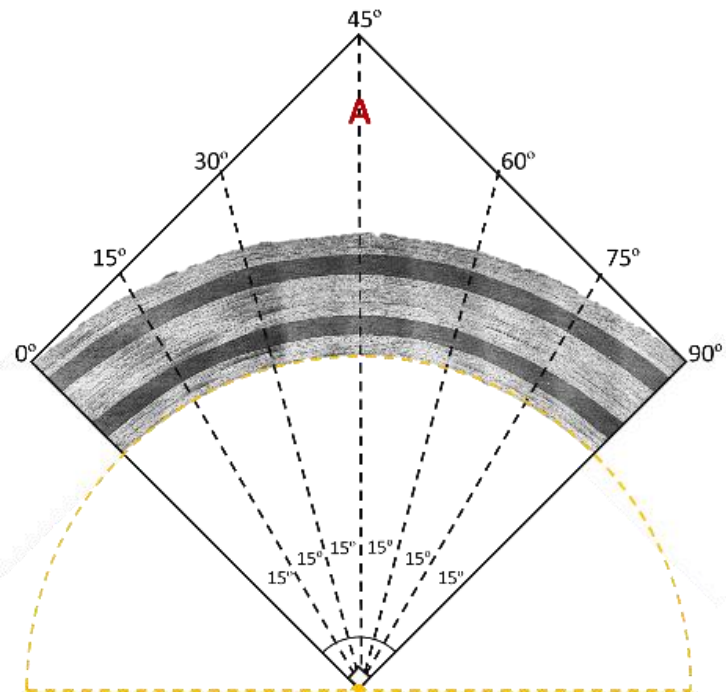


Figure 58. Representation of examination sections on the curved region.

In 90° layers, in addition to major matrix cracks and delamination failures, hairline matrix cracks (secondary matrix cracks) are also observed in the curved region. Micrograph examination of a failed specimen 90t3s4 is shown in Figure 59. Matrix cracking is observed in the 45° – 90° section of the curved region only. Even though the loading is symmetric, symmetry is broken once failure initiates. Secondary cracks are shown by dashed ellipses and marked from 1 to 6. Cracks 1 and 5 are major matrix cracks and they continue as delamination through the arms to the left and right arms, respectively. The other cracks are secondary matrix cracks. As we approach the left

arm from the center, the direction of the secondary cracks in the left become more tilted towards the left. This indicates that the stress field becomes more shear dominated and will be further discussed.

As shown by the analysis in the discussion section, tangential stresses close to the failure strength, cause vertical hairline cracks while the horizontal crack propagates. The angles of the hairline cracks are increasing towards the arms and vertical at the center seen in Figure 59 due to the shear stress which is zero at the center of the curve and increases towards the arms as seen in Figure 82.

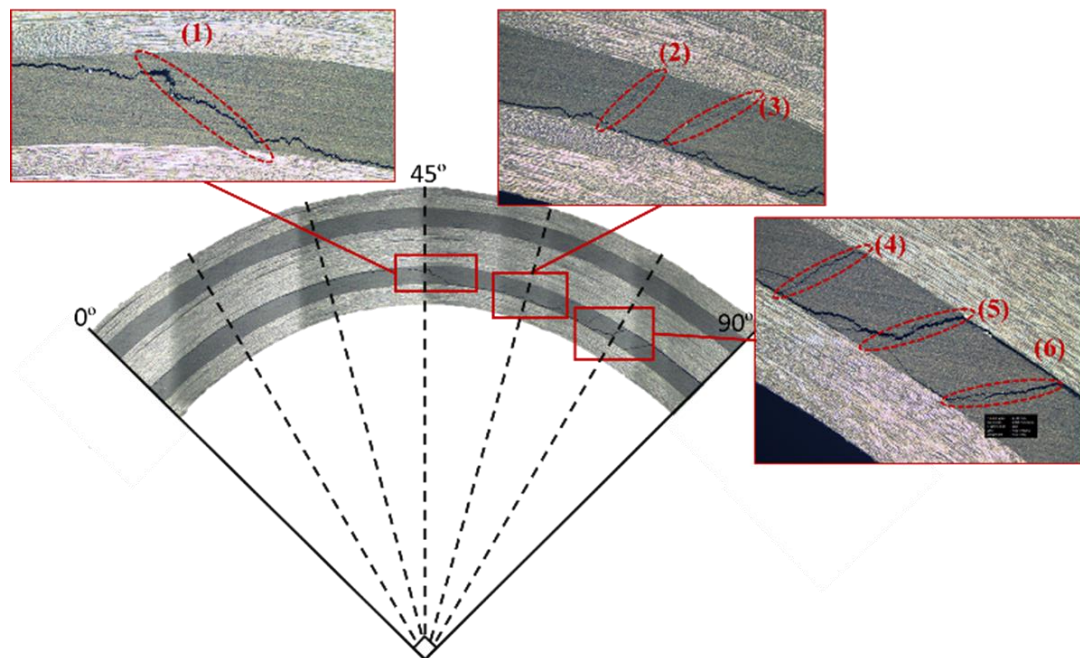


Figure 59. Detailed examination of the failure on micrographs for specimen 90t3s4 tested under static loading.

Another specimen (90t3s2) was painted with a speckle pattern and the images were captured with a camera during the experiment and analyzed with DIC analysis tool ARAMIS to obtain the evolution of the strain distribution in the specimen. Failure occurs at 444 N load which corresponds to 11.6 mm displacement and drops to 89 N after the failure.

In Figure 60, contours of the Tresca strain on the side of the specimen in the curved region are presented at the specific points in the load-displacement curve. After a gradual increase of the strains with loading up to 200 N, concentrated strain regions are observed in the inner 90° layer shown by the red color. Three regions of strain concentrations greater than 1.0% in the inner 90° layer, symmetrically distributed around the symmetry line of the curved region become visible at 200 N. Then as the load increases, the strain concentration also increases, saturating the strain scale. Moreover, final image shows the cracks after the load drop. In Figure 61, the change in Tresca strain field on the curved specimen during the experiment is shown in the images taken every minute of the experiment and last two images are at the cracking instant just before and after the failure.

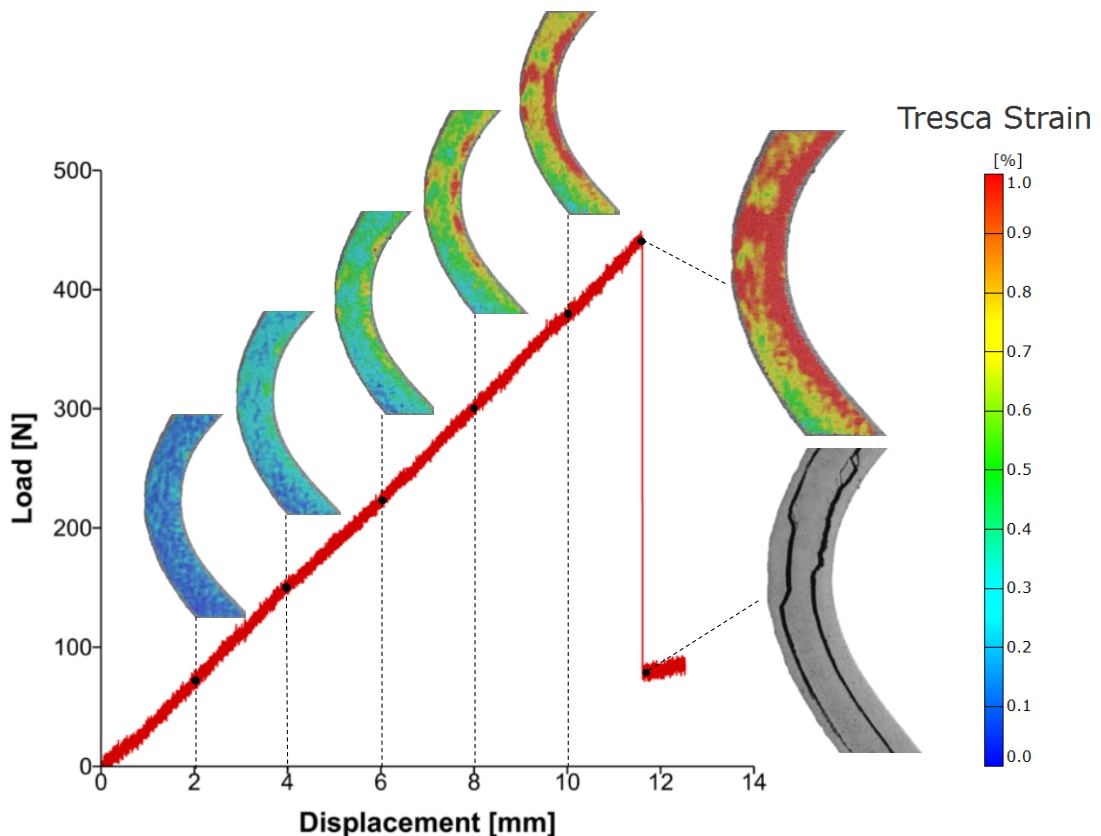


Figure 60. Representation of change in Tresca strain in the specimen (90t3s2) on the load-displacement curve.

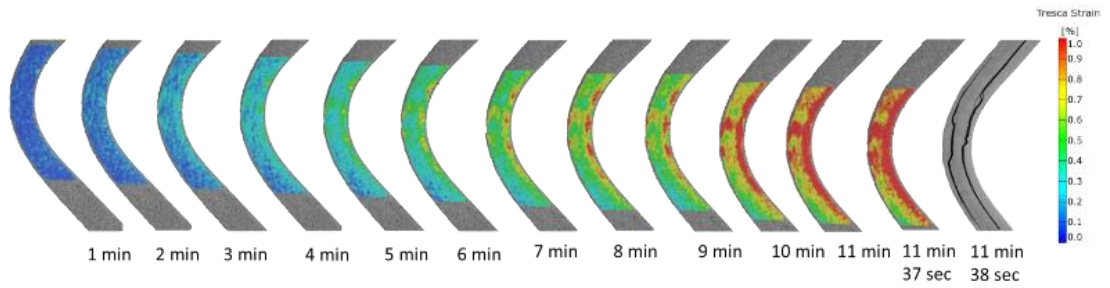


Figure 61. Change of Tresca strain distribution in the specimen (90t3s2) with time up to failure.

Detailed examination of the Tresca strain distribution in the specimen just before the failure shows three important concentrations exactly in the inner group of 90° layers as seen clearly in Figure 62. Strain field is overlaid on the image after the failure at the right hand side of the figure. It shows that strain concentrations accurately indicate that failure pattern follows the maximum Tresca strain locations. If we take a closer look at the Tresca strain field and failure pattern of the specimen, we can see the regions of failure: straight cracks (delamination) region and undulating cracks (matrix cracks) region as in Figure 63. Strain concentrations just before failure looks very symmetric. However, symmetry is broken when the crack initiates at the upper part, which changes the stress distribution and unloads the lower part. After growth of the cracks in the matrix for some distance, the major crack continues as a single delamination on both sides. Symmetry of the stress distribution on the curved region due to symmetric loading is broken after failure due to unloading initiating at the chosen failure location.

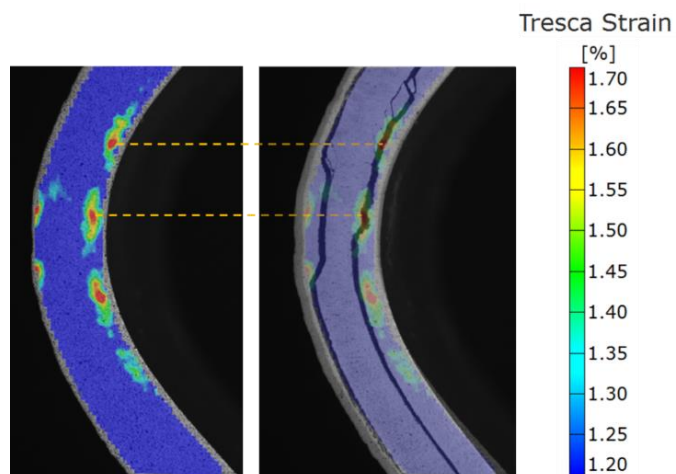


Figure 62. Tresca strain distribution just before the failure and its representation on the specimen image just after the failure.

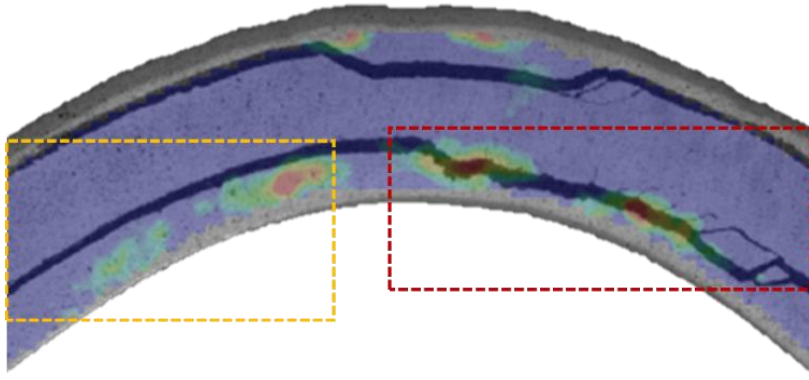


Figure 63. Close-up views of Tresca strain field and failure pattern of the specimen.

Post-failure micrographs of the same curved specimen with the cracks on the surface that was coated for DIC analysis can be seen in Figure 64. Close-up views of the cracks are seen in (b), (d) and (e), for left, center and right cracked regions. We can observe four kinds of damage: brittle coating micro-cracks, matrix hairline cracks, and major matrix cracks in addition to delamination. In Figure 64 (a), the evolution of the cracking can be seen. The cracks start in the center region in the 90° group layer, with the matrix crack growing following a tortuous path in the center of the group. However, 45-50° hairline cracks are also observed emanating from the main crack until one of those cracks become dominant and connect the major matrix crack to the 0/90 interface. Afterwards, the crack grows as a delamination between the 0° and 90° plies towards the arms. A more detailed description is given in the close-up views.

As the delamination progresses towards the arms, micro-cracks in the brittle coating on the delamination path are observed as jagged toothed lines, shown in Figure 64 (b). In Figure 64 (c), the opposite surfaces of the delaminated interface are separated and the common features in the outline of the right crack surface (in red) is matched with the left crack surface when displaced by a distance shown by the black dotted arrows. Both the orientation of the brittle micro-cracking of the coating and the matching of the corresponding features show that there is relative sliding between 0° and 90° plies, and is dominated by shear sliding as the delamination moves to the arms.

Figure 64 (d) and (e) show a close-up view of the center region and the right arm region where hairline cracks in addition to brittle coating cracks can be observed,

respectively. In the figures, the red arrows show the direction of the matching surfaces and the red ellipses show the location and direction of the hairline cracks emanating from the major crack. Near the center, the upper and lower surfaces are displaced from each other only in the opening direction and not in the tangential direction. The hairline cracks are seen to start from the major horizontal matrix crack. At the center, these cracks are oriented vertically to the 0/90 interface and rotated 45-50° in the region near the arms. Finally, one or several of these hairline cracks become dominant and connect the major matrix crack to the interface causing delamination at the upper 0/90 interface as shown in the close-up Figure 64 (e). These hairline cracks are not only on the coating but go through the width of the material inside the 90° group of plies.

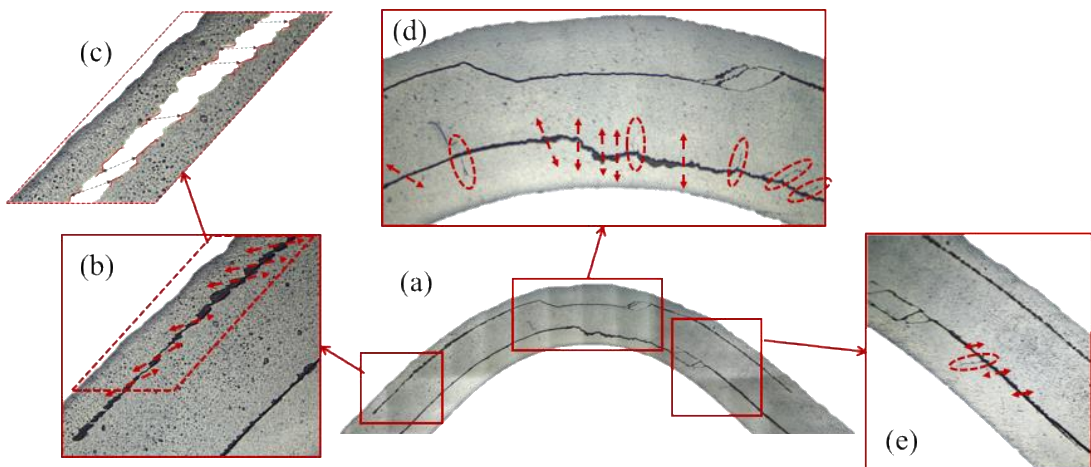


Figure 64. Detailed examination of the failure on micrographs of the thin curved cross-ply specimen tested under static loading using DIC method.

5.1.1.2 Thick Cross-Ply Curved Laminates

Two thick [0₃/90₃/0₃/90₃/0₃]_s curved specimens cut from the same composite batch are tested under static loading to failure. One specimen (90t5s3) is used to conduct DIC experiment and the other (90t5s5) is used in the experiment recorded with a high resolution camera. Both specimens are loaded quasi-statically under displacement control at a displacement rate of 1 mm/min and images are captured at 1fps.

Load-displacement curves of both specimens are shown in Figure 65 (a). Although the stiffness values and failure loads of each specimen vary slightly, they are very close to

each other. Thus, the overall behavior of all specimens are consistent. The stiffness is 150 ± 3 N/mm and the failure load is 875 ± 3 N which drops to 555 ± 5 N after failure.

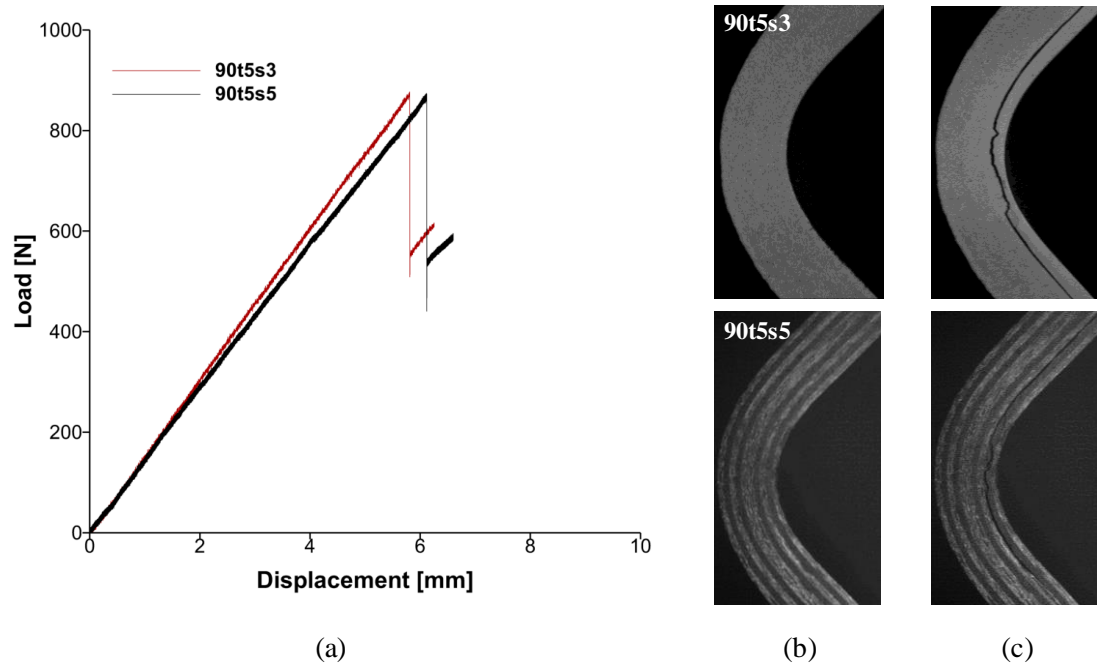


Figure 65. (a) Load-displacement curves, pictures of the specimens (b) before failure and (c) after failure.

In Figure 65 (b) and (c), captured images of the specimens before and after the failure are presented. The failure mechanism is seen to be a single dominant crack in the inner 0/90 interface for both specimens. In both specimens, intralaminar matrix cracks in the inner group of 90° layers and delamination at the interface of 0° and 90° layers are observed clearly from the post failure images. Matrix cracking starts at upper or lower side of the symmetry axis and continues as delamination towards the both arms.

In Table 7, details of static experiments are given such as the number of cracks, the location of the major crack, the critical load and displacement values, the stiffness before and after the failure and the residual load and displacement values. Observed crack locations are always the same.

Table 7. Summary table for static experiments of thick cross-ply specimens.

Spc Name	# of cracks	Location of crack	P_c (N)	δ_c (mm)	Stiffness (N/mm)	P_r (N)	2 nd stiffness (N/mm)	δ_r at $P=0$ (mm)
90t5s3	1	0.2R	877	5.8	153	553	138	0.37
90t5s5	1	0.2R	871	6.11	146	560	134	1.6

Specimen 90t5s3 was painted with a speckle pattern and the images were captured with a camera during the experiment and analyzed with DIC analysis tool ARAMIS to obtain the evolution of the strain distribution in the specimen. Failure occurs at 877 N load which corresponds to 5.8 mm displacement and drops to 553 N after the failure.

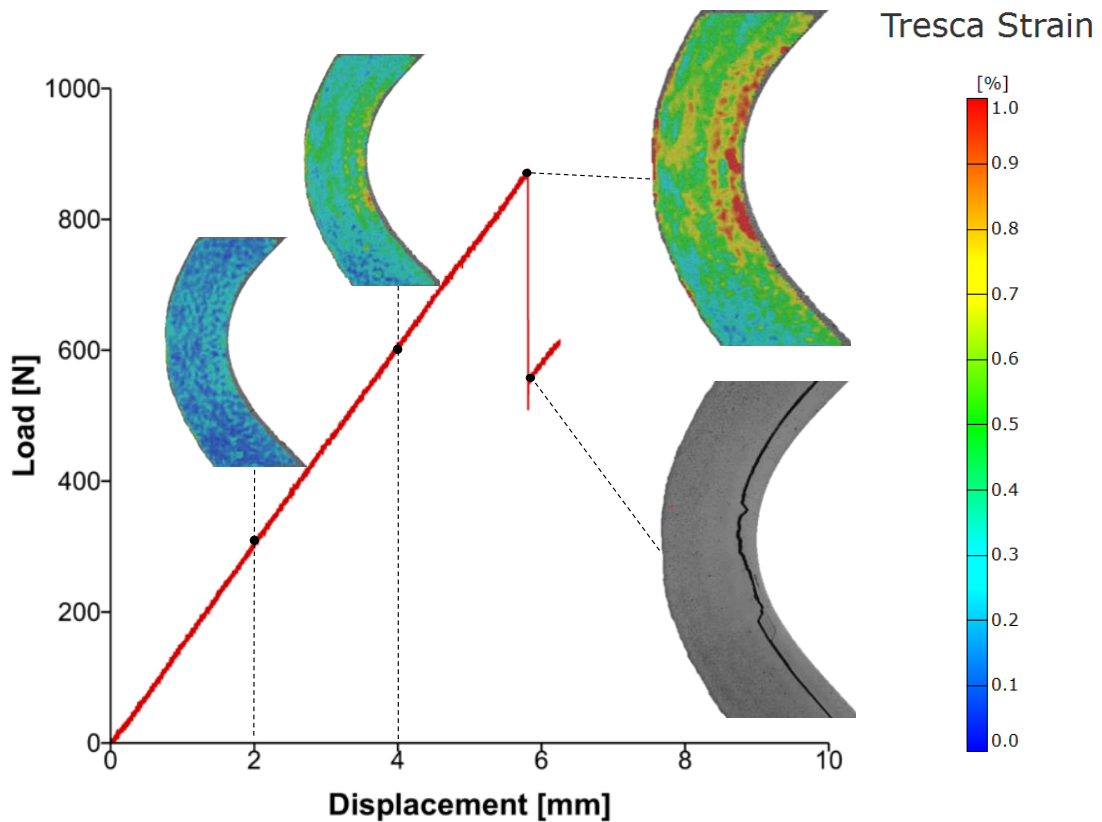


Figure 66. Representation of change in Tresca strain in the specimen (90t5s3) on the load-displacement curve.

In Figure 66, contours of the Tresca strain on the side of the specimen in the curved region are presented at the specific points in the load-displacement curve. With loading, the strain increases homogeneously in the curved geometry. As the failure load is approached, a region of strain concentration greater than 1.0% in the inner group of 90° layers becomes visible as hot-spots, distributed symmetrically around the symmetry line of the curved region. Then as the load increases to the failure load, the strain concentration also increases, saturating the strain scale. Moreover, final image shows the crack after the load drop. In Figure 67, the change in Tresca strain field on the curved specimen during the experiment is shown in the images taken every minute of the experiment and last two images are at the cracking instant just before and after the failure.

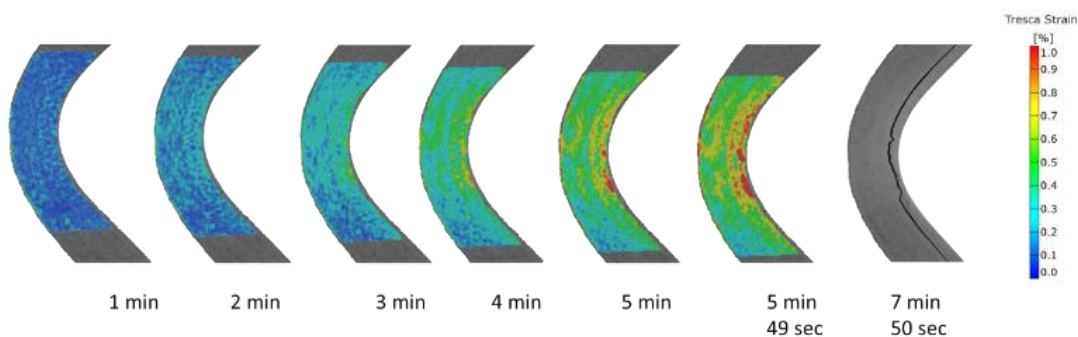


Figure 67. Change of Tresca strain distribution in the specimen (90t5s3) with time up to failure.

Detailed examination of the Tresca strain distribution in the specimen just before the failure shows two discernible hot spots of strain concentration in the inner group of 90° layers as seen in Figure 68. Strain field is overlaid on the image after the failure at the right-hand side of the figure. It shows that strain concentrations accurately indicate that failure pattern follows the maximum Tresca strain locations. In the second group of 90° layers, there are also remarkable strain concentrations. If we take a closer look at the Tresca strain field and failure pattern of the specimen, we can see the regions of failure: straight cracks (delamination) region and undulating cracks (matrix cracks) region as in Figure 69.

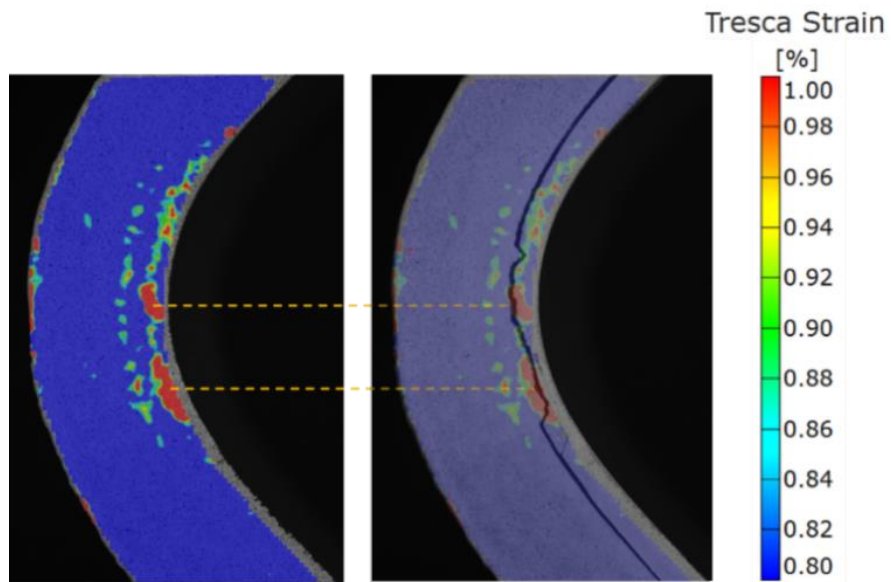


Figure 68. Tresca strain distribution just before the failure and its representation on the specimen picture just after the failure.

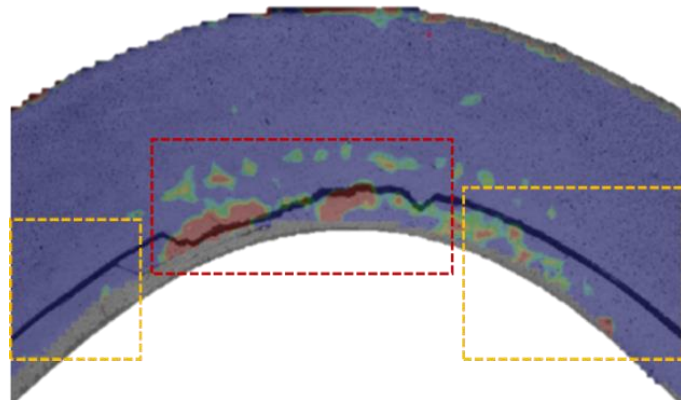


Figure 69. Closer look to Tresca strain field and failure pattern of the specimen.

Post-failure micrographs of the same curved specimen with the cracks on the surface that was coated for DIC analysis can be seen in Figure 70. Close-up views of the cracks are seen in (b) and (c), for left and right cracked regions. We can observe four kinds of damage: brittle coating micro-cracks, matrix hairline cracks, and major matrix cracks in addition to delamination. In Figure 70 (a), the evolution of the cracking can be seen. The cracks start in the center region in the 90° group layer, with the matrix crack growing following a tortuous path in the center of the group. However, 45-50° hairline cracks are also observed emanating from the main crack until one of those cracks become dominant and connect the major matrix crack to the 0/90 interface.

Afterwards, the crack grows as a delamination between the 0° and 90° plies towards the arms. A more detailed description is given in the close-up views.

Figure 70 (b) and (c) show a close-up view of the left center and the right arm region, respectively, where hairline cracks in addition to brittle coating cracks can be observed. In the figures, the red arrows show the direction of the matching surfaces and the red ellipses show the location and direction of the hairline cracks emanating from the major crack. Near the center, the upper and lower surfaces are displaced from each other only in the opening direction and not in the tangential direction. The hairline cracks are seen to start from the major horizontal matrix crack. At the center, these cracks are oriented vertically to the $0/90$ interface and rotated $45\text{--}50^\circ$ in the region near the arms. Finally, one or several of these hairline cracks become dominant and connect the major matrix crack to the interface causing delamination at the upper $0/90$ interface as shown in the close-up Figure 70 (c). These hairline cracks are not only on the coating but go through the width of the material inside the 90° group of plies.

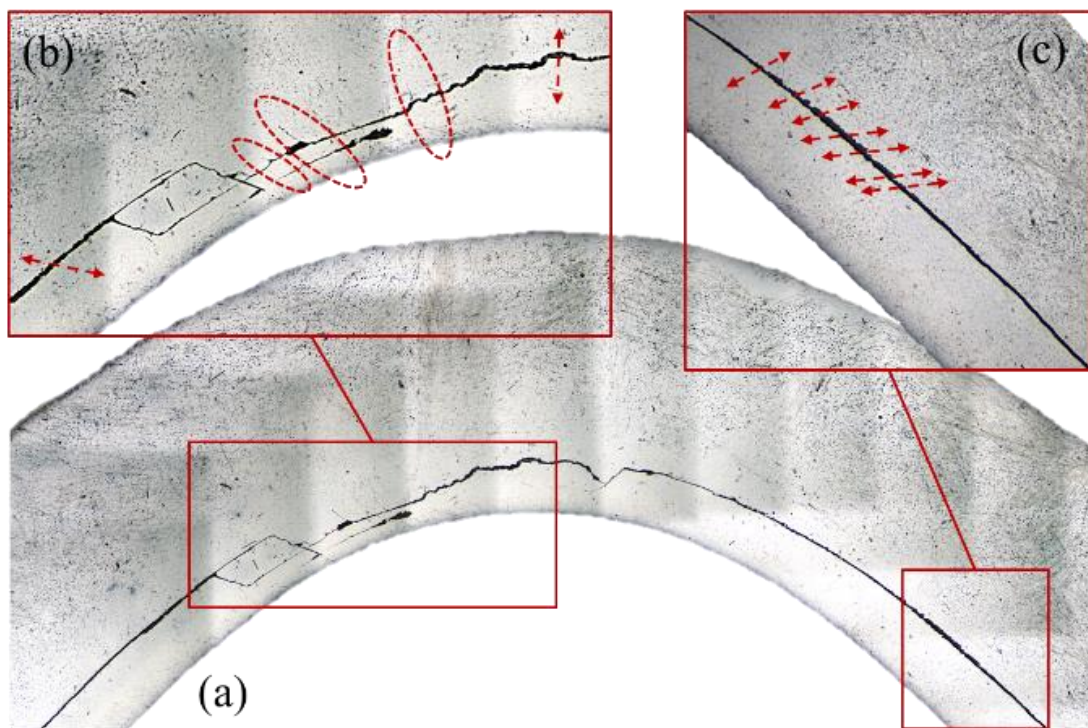


Figure 70. Detailed examination of the failure on micrographs of the thick curved cross-ply specimen tested under static loading and using DIC method.

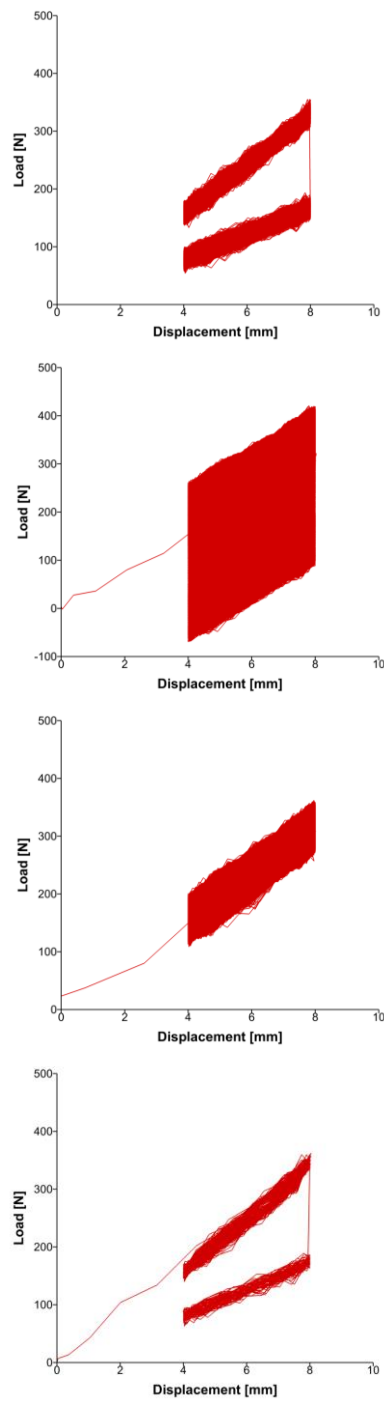
5.1.2 Fatigue Tests of Cross-Ply Curved Laminates

5.1.2.1 Thin Cross-Ply Curved Laminates

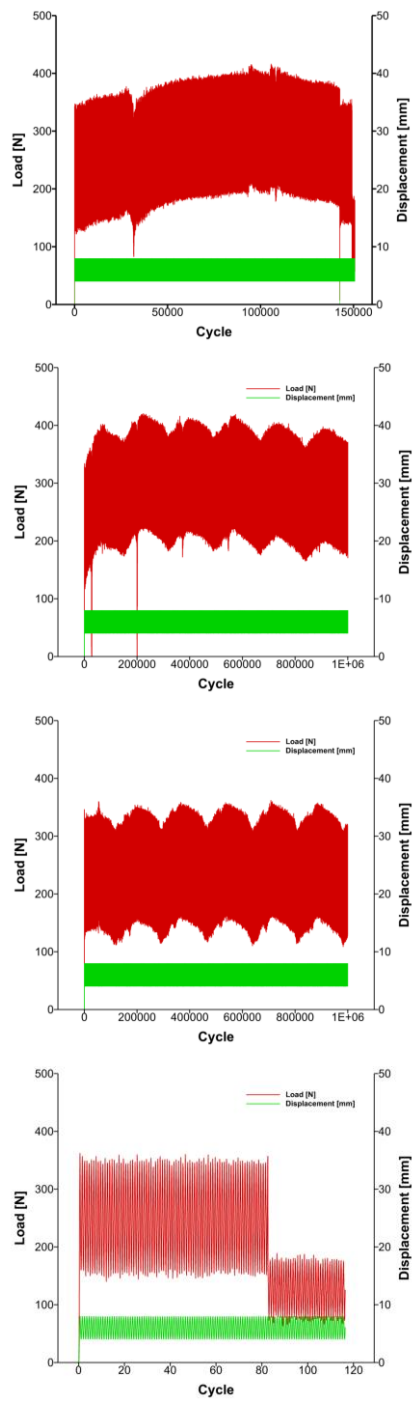
Four thin [0₃/90₃/0₃]_s curved specimens cut from the same composite batch are tested under fatigue loading to the failure under displacement control with a displacement range of 4-8 mm (66% of the critical displacement of the static experiments) at a frequency of 2 Hz. Two of the specimens (90t3s6 and s8) did not fail at 1,000,000 cycles at that point the tests were stopped with no visible damage observed. Two specimens (90t3s5 and s9) failed, one at 150,000 cycles and the other at 80 cycles. The load-displacement behavior during the experiment and load-displacement parameters as a function of number of cycles are shown in Figure 71 (a) and (b). Two failed specimens surprisingly exhibit the same damage behavior (Figure 71 (c)) despite the fact that they failed at very different number of cycles. A single dominant crack is observed in the inner 0/90 interface for both specimens as seen in the images in Figure 71 (c).

In Figure 71, there are 6 visible rises and falls in the maximum and minimum loads in the load-cycle curves of 90t3s6 and s8. It is presumed that, these rises and falls caused by temperature change in one day of six day-long 1 million cycle fatigue experiment. In order to understand whether these rises and falls lead to stiffness degradation in the specimen or not, maximum and minimum loads are separated for each cycle and the difference is plotted in Figure 72. The straight difference line in the graph shows that there is no stiffness degradation in the specimen.

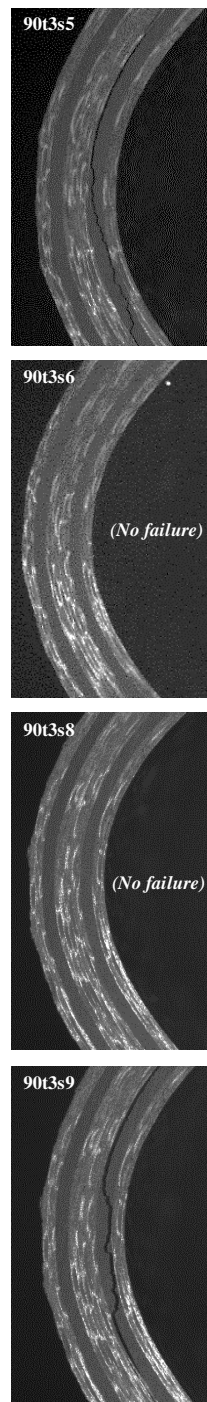
The stiffness graph is plotted for all specimens in the logarithmic scale by dividing the load difference to displacement difference (4 mm). As clearly seen in Figure 73, stiffness reduction is not observed up to failure. The stiffness values before the failure is 40 ± 4 N/mm and reduced to 25 ± 5 N/mm after the failure.



(a)



(b)



(c)

Figure 71. (a) Load-displacement curves, (b) load-cycle-displacement curves and (c) pictures of the specimens after the failure

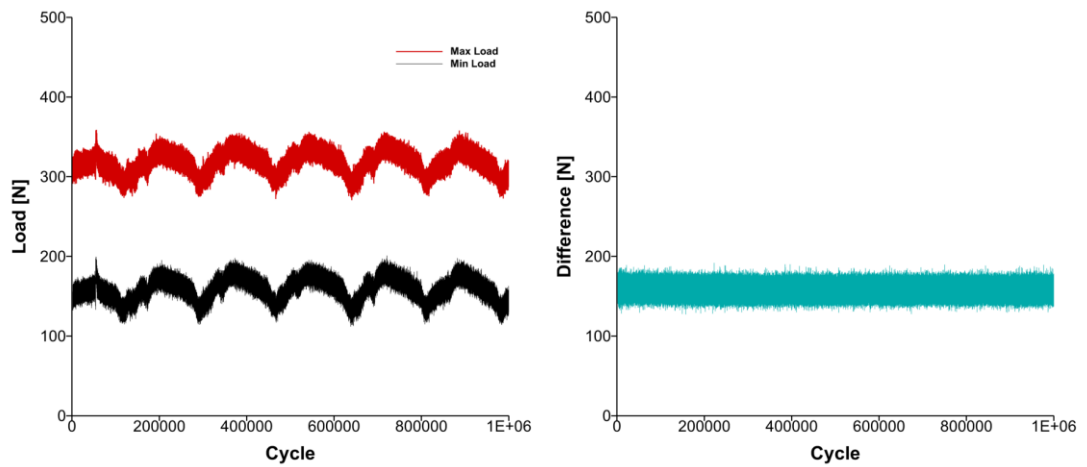


Figure 72. Maximum and minimum loads during the fatigue loading and the differences (stiffness) for specimen 90t3s8.

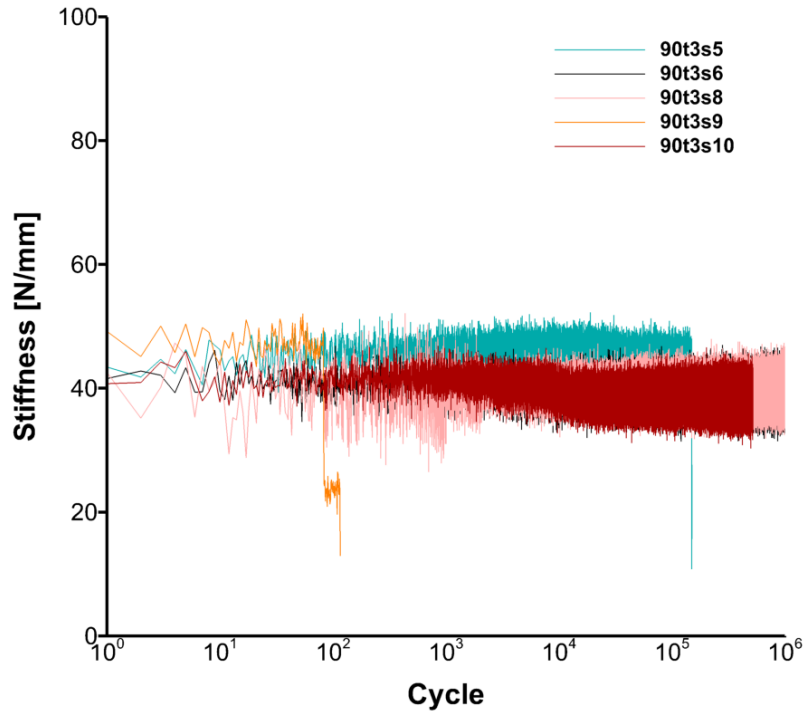


Figure 73. Change in stiffness with cycles.

To ensure whether these rises and falls caused by temperature change or not, one more experiment is conducted up to 500,000 cycle (3 days) by measuring the temperature by a digital thermometer. Change in load and the temperature with time during the 3 day-long experiment is given in Figure 74. Three peaks are visible in the graph as expected for three day-long experiment.

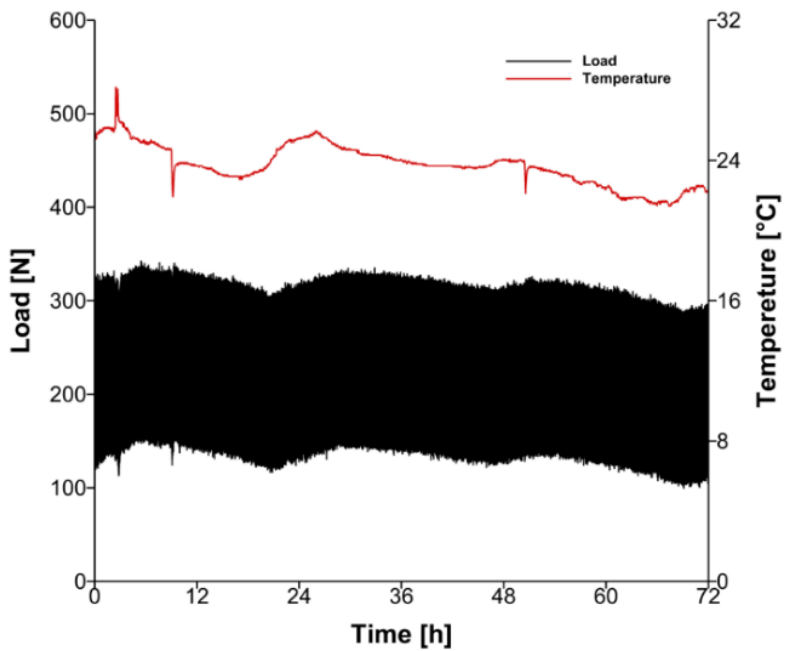


Figure 74. Load-displacement change in load and temperature for specimen 90t3s10.

In Figure 75, maximum and minimum loads are separated for each cycle and the difference is plotted. The straight difference line in the graph shows that there is no stiffness reduction in the specimen. The load increase due to change in temperature is calculated according to analytical method explained in Section 3.2.2. By extracting the thermal load, absolute max and min loads for each cycle are plotted on the same graph. The absolute max and min loads are roughly straight and this behavior proves that the peaks for each day are caused by the change in temperature.

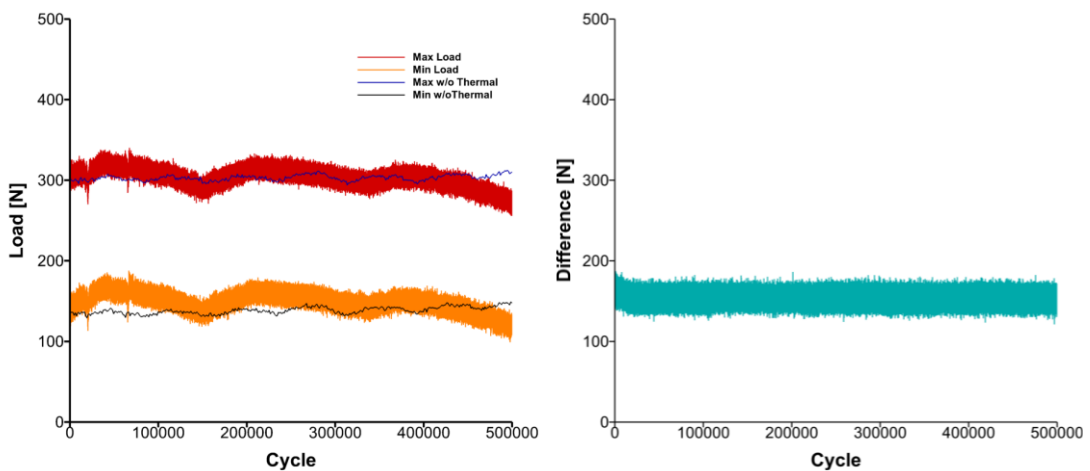


Figure 75. Maximum and minimum experimental loads and the thermal effect free loads during the fatigue loading and the difference graph for specimen 90t3s10.

In 90° layers, in addition to major matrix cracks and delamination failures, hairline matrix cracks (secondary matrix cracks) are also observed in the curved region. Micrograph examination of a failed specimen 90t3s5 is shown in Figure 76. Matrix cracking is observed in the 0°–45° section of the curved region only. Even though the loading is symmetric, symmetry is broken once failure initiates. Secondary cracks are shown by dashed ellipses and marked from 1 to 6. The secondary cracks near the symmetry plane are perpendicular to the interface. As we approach to the left arm from the center, the direction of the secondary cracks in the left become more tilted towards the left. This indicates that the stress field becomes more shear dominated and will be further discussed.

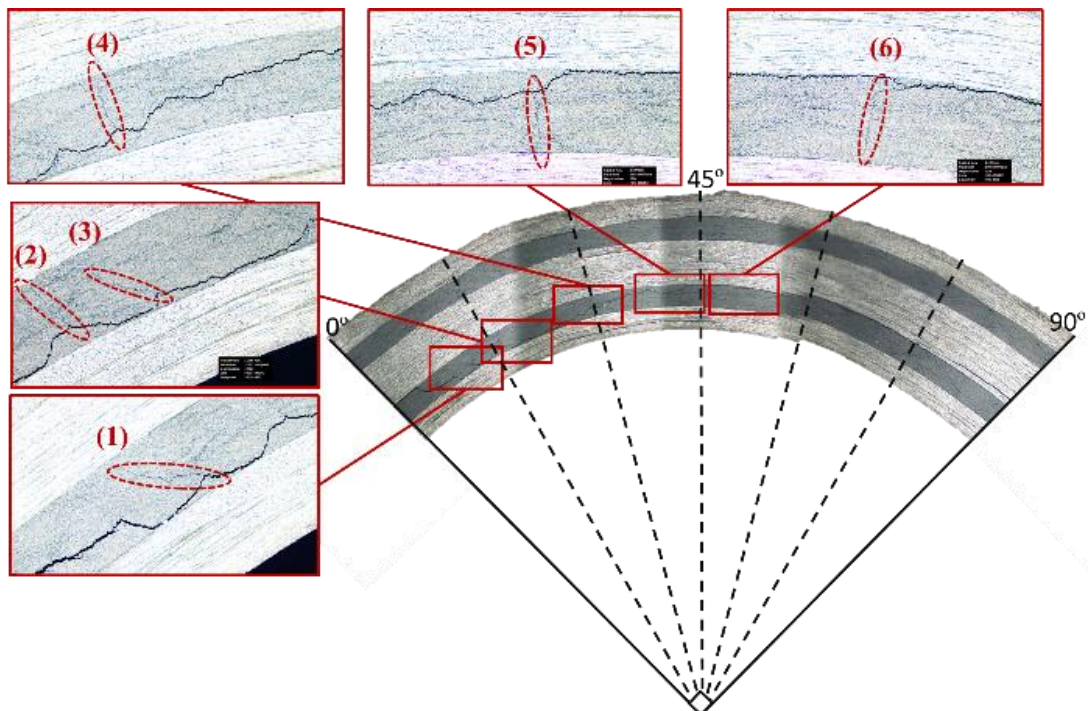


Figure 76. Detailed examination of the failure on micrographs of specimen 90t3s5 tested under fatigue loading.

5.1.2.2 Thick Cross-Ply Curved Laminates

Three thick $[0_3/90_3/0_3/90_3/0_3]_s$ curved specimens cut from the same composite batch are tested under fatigue loading to the failure under displacement control with a displacement range of 2– 4 mm (66% of the critical displacement of the static experiments) at a frequency of 2 Hz. But there is only one exception, the specimen 90t5s10 is tested with a displacement range 1-3mm. The specimens (90t5s7, s8, s9 and s10) failed at 38,000, 58,000, 2 and 3,000 cycles respectively. The load-displacement behavior during the experiment and load-displacement parameters as a function of number of cycles are shown in Figure 77 (a) and (b). Four specimens surprisingly exhibit the same behavior despite the fact that they failed at very different number of cycles as shown in Figure 77 (c). A single dominant crack is observed in the second 0/90 interface for all specimens as seen in the images.

There are obvious drops in the maximum and minimum loads for the specimens s7 and s10. In order to understand whether these load drops lead to stiffness degradation in the specimen or not, maximum and minimum loads are separated for each cycle and difference of them is plotted in Figure 78. The straight difference line in the graph shows that there is no stiffness degradation in the specimen. As mentioned in the previous section and presented in Figure 75, these load drops are presumed to occur due to temperature change. These sharp load drops seen in the experimental results of the specimens s7 and 10 are due to solar light on the specimen surface. It is realized at the load drop instant and for the other experiments an obstacle is located in front of the test setup to prevent temperature effect.

The stiffness graph is plotted for all specimens in the logarithmic scale by dividing the load difference to displacement difference (2 mm). As clearly seen in Figure 79, stiffness reduction is not observed up to failure. The stiffness values before the failure is 160 ± 5 N/mm and reduced to 85 ± 10 N/mm after the failure.

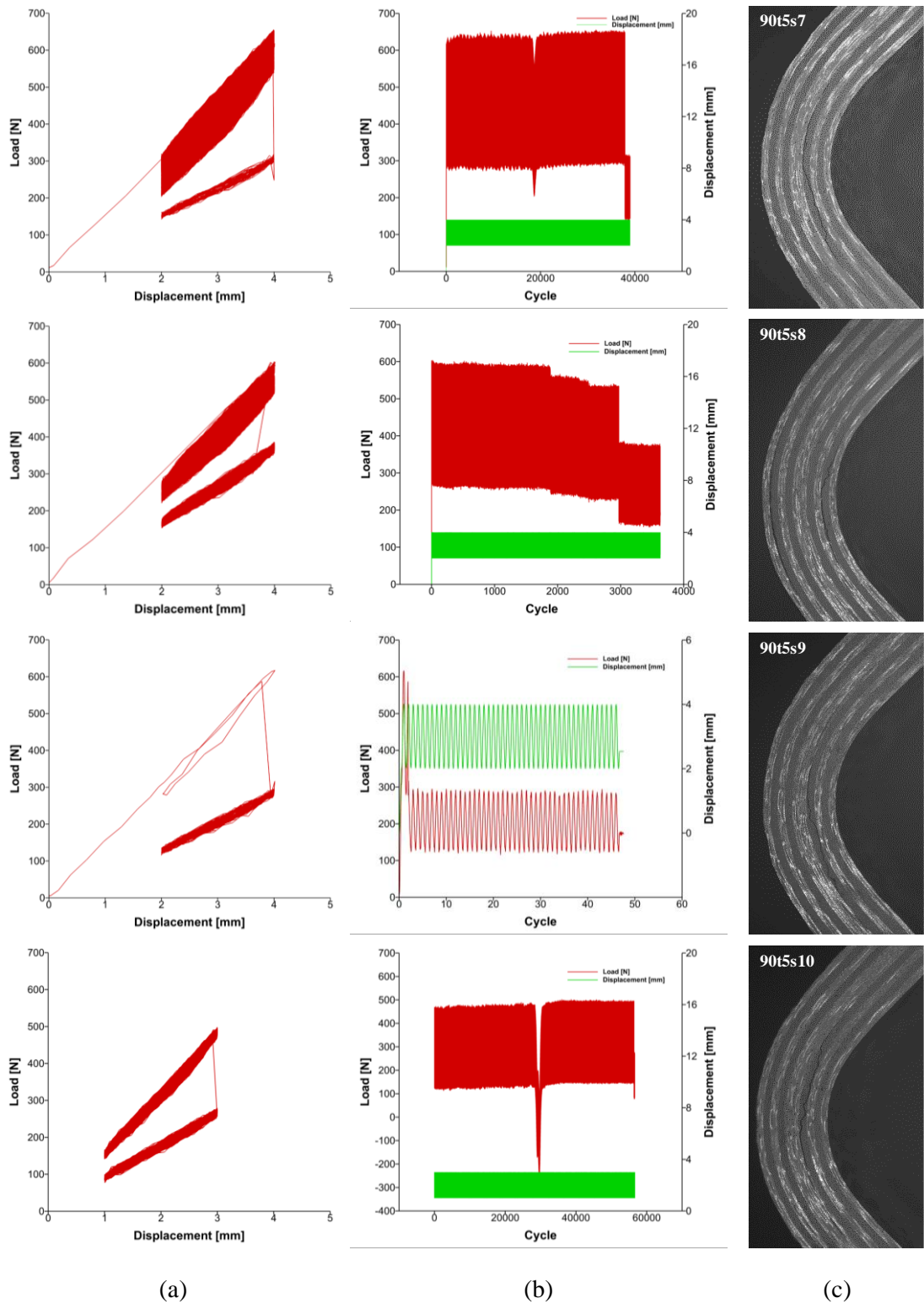


Figure 77. (a) Load-displacement curves, (b) load-cycle-displacement curves and (c) images of the specimens after the failure.

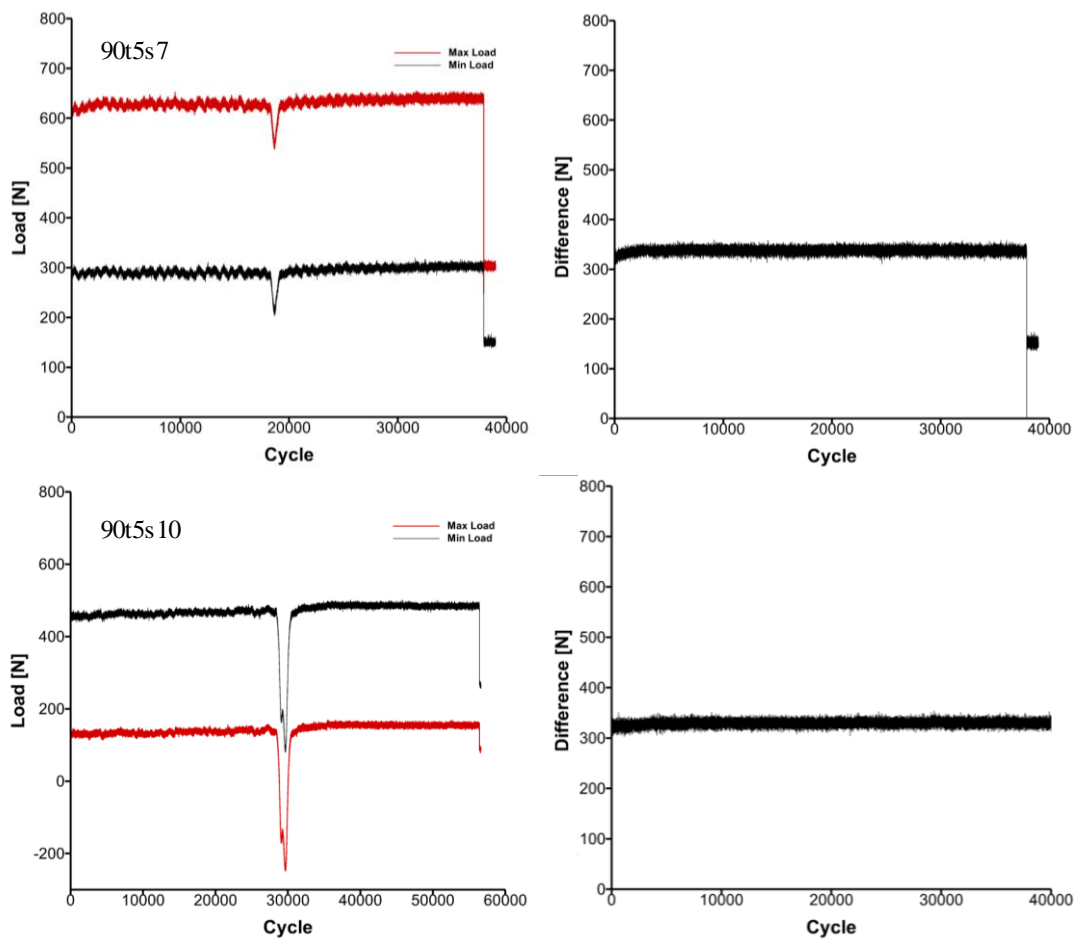


Figure 78. Maximum and minimum loads during the fatigue loading and the differences for specimen 90t5s7 and 90t5s10.

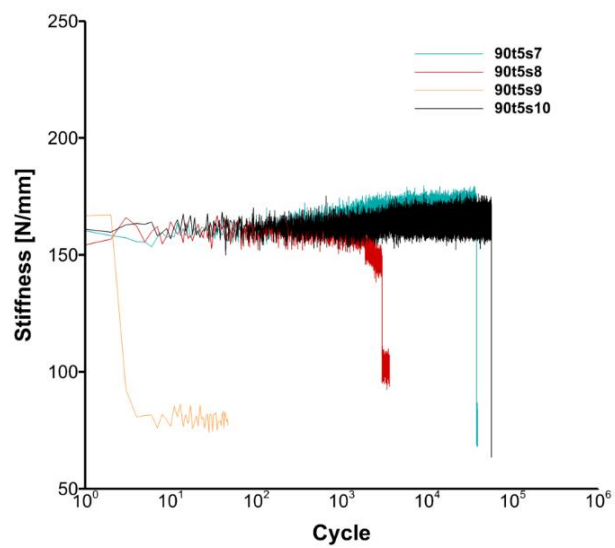


Figure 79. Change in stiffness with cycles.

5.2 Analytical Results of Cross-Ply Curved Laminates

5.2.1 Thin Cross-Ply Curved Laminates

To understand the reason of the experimentally observed crack initiation location, analytical calculations are applied to the curved region for thin [0₃/90₃/0₃]_s cross-ply specimen. Analytical calculations are performed based on the multilayer curved beam solution explained in the analytical method section and the prescribed force is 400 N in the vertical direction as in the experimental setup. Stress distributions are examined in the direction of the thickness and in the direction of the curve. Examinations are performed at 0°, 15°, 30° and 45° sections of the curve as shown in Figure 80 for both directions. In addition for the direction of the curve, inner group of 90° plies (4th, 5th and 6th layers) are investigated in detail as shown in Figure 81. Average of each 90° plies are also calculated and presented for the comparison.

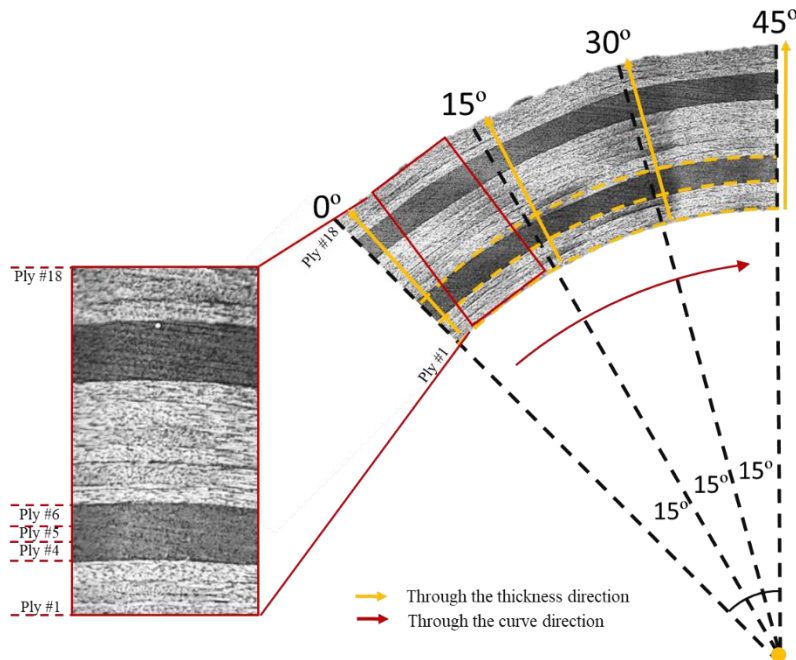


Figure 80. Representation of directions and sections used for stress distribution calculations on thin cross-ply curved specimen.

For the case of radial and tangential stresses in direction of the curve, there are minor changes between the 0°, 15°, 30° and 45° sections. However, the shear stress decreases

from 5 MPa to 0 at mid (45°) section of the curve. Larger amount of change is observed in shear stress from 0° section to mid (45°) section.

Radial, tangential and shear stresses in the direction of the thickness are compared through the normalized thickness for the 0° , 15° , 30° and 45° sections and given in Figure 82. Larger difference as percentage is observed for the shear stress. However, it should be noted that the magnitude of the shear stress is much smaller than the radial and tangential stresses.

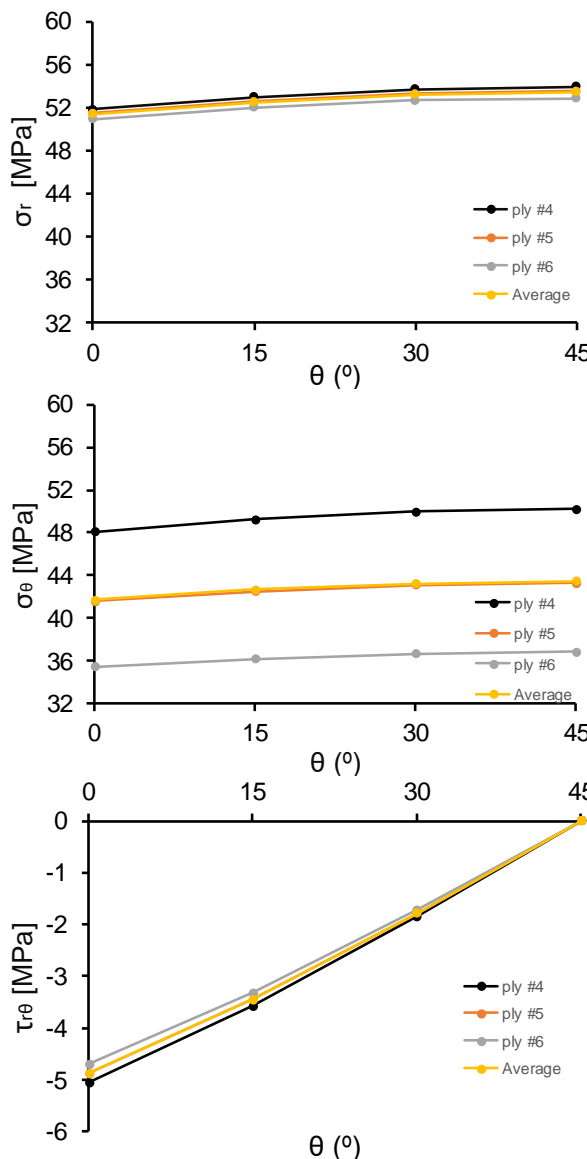


Figure 81. Radial, tangential and shear stress distribution through the curve direction.

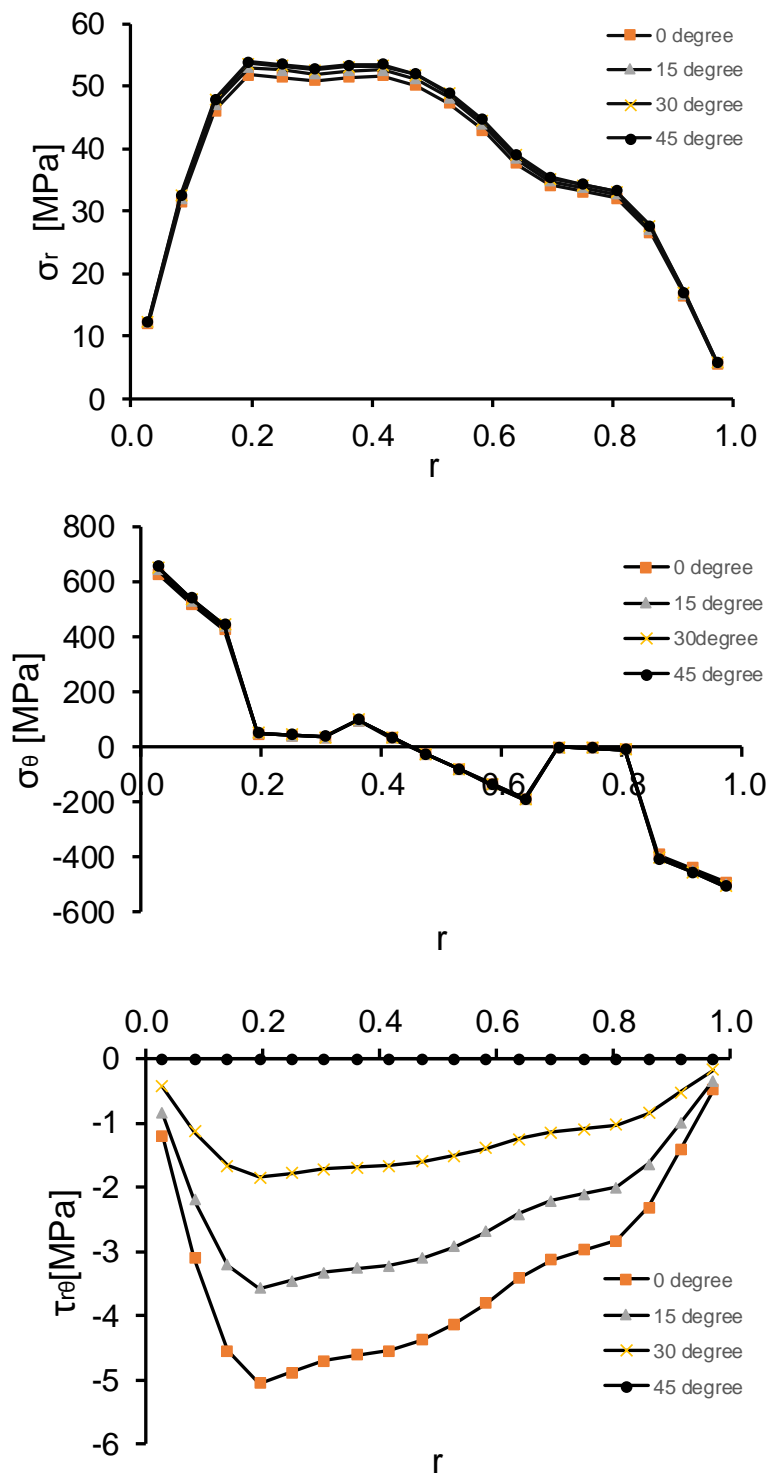


Figure 82. Radial, tangential and shear stress distributions through the thickness direction.

5.2.2 Thick Cross-Ply Curved Laminates

To understand the reason of the experimentally observed crack initiation location, analytical calculations are applied to the curved region for thick [0₃/90₃/0₃/90₃/0₃]_s cross-ply specimen. Analytical calculations are performed based on the multilayer curved beam solution explained in the analytical method section and prescribed force is 800 N in the vertical direction as in the experimental setup. Stress distributions are examined in the direction of the thickness and in the direction of the curve. Examinations are performed at 0°, 15°, 30° and 45° sections of the curve as shown in Figure 83 for both directions. In addition for the direction of the curve examinations, first group of 90° plies (4th, 5th and 6th layers) and second group of 90° plies (10th, 11th and 12th layers) are investigated in details as seen in Figure 84. Average of each 90° plies are also calculated and presented for the comparison.

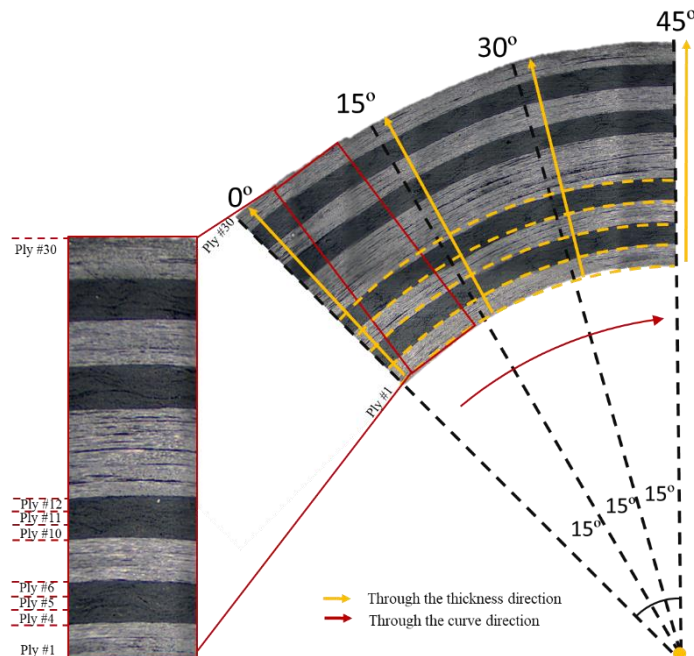


Figure 83. Representation of directions and sections used for stress distribution calculations on thick cross-ply curved specimen.

For the case of radial and tangential stresses in direction of the curve, there are no major changes between the 0° , 15° , 30° and 45° sections. However, the shear stress reaches to zero at the mid (45°) section of the curve. Larger amount of change is observed in shear stress from 0° section to mid (45°) section.

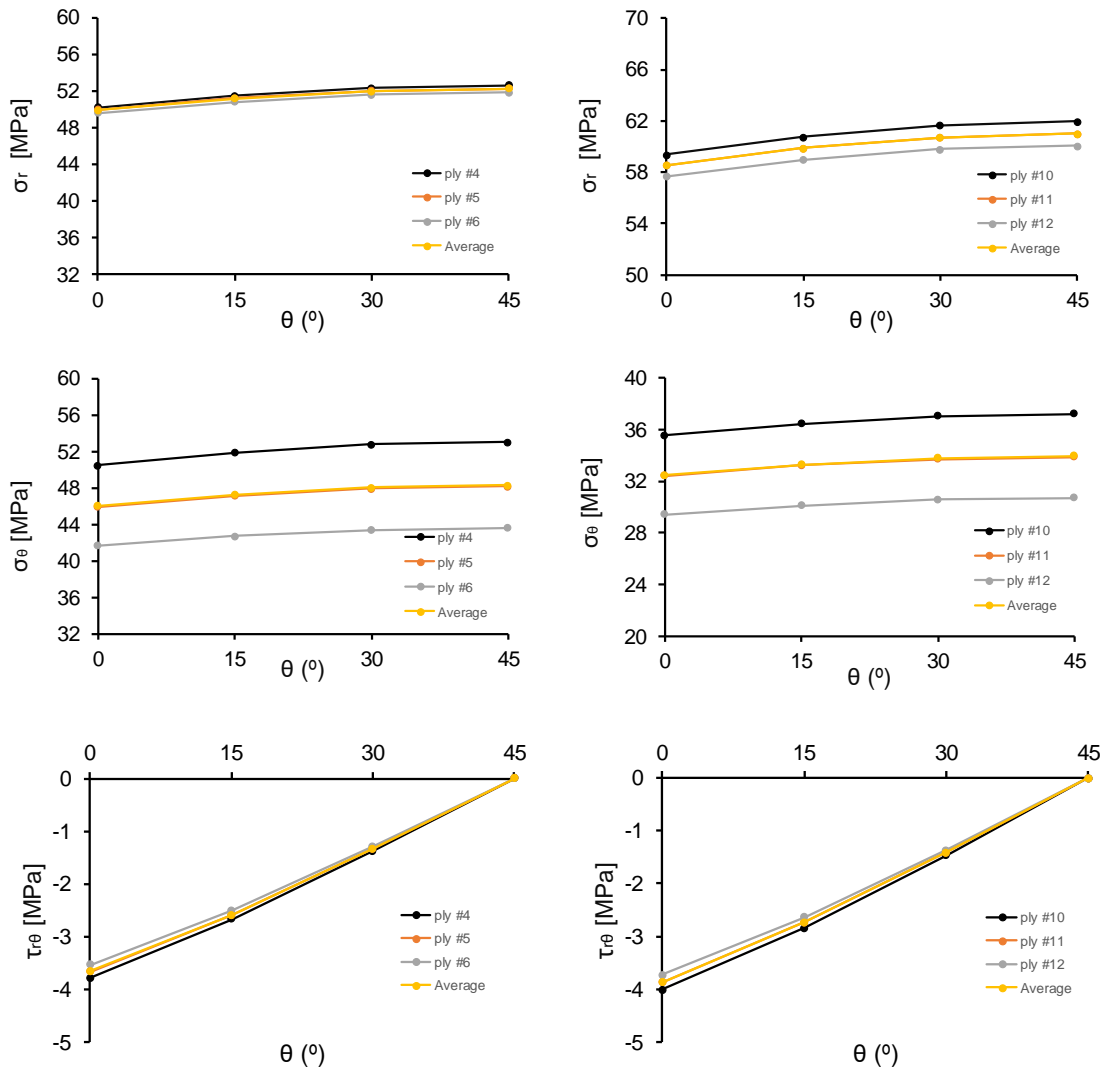


Figure 84. Radial, tangential and shear stress distributions through the curve direction at 4th, 5th, 6th and 10th, 11th, 12th layers.

Radial, tangential and shear stress distributions in the direction of the thickness are compared through the normalized thickness for the 0° , 15° , 30° and 45° sections and given in Figure 85. Larger difference as percentage is observed for shear stress. However, it should be noted that magnitude of the shear stress is much smaller than the radial and tangential stresses.

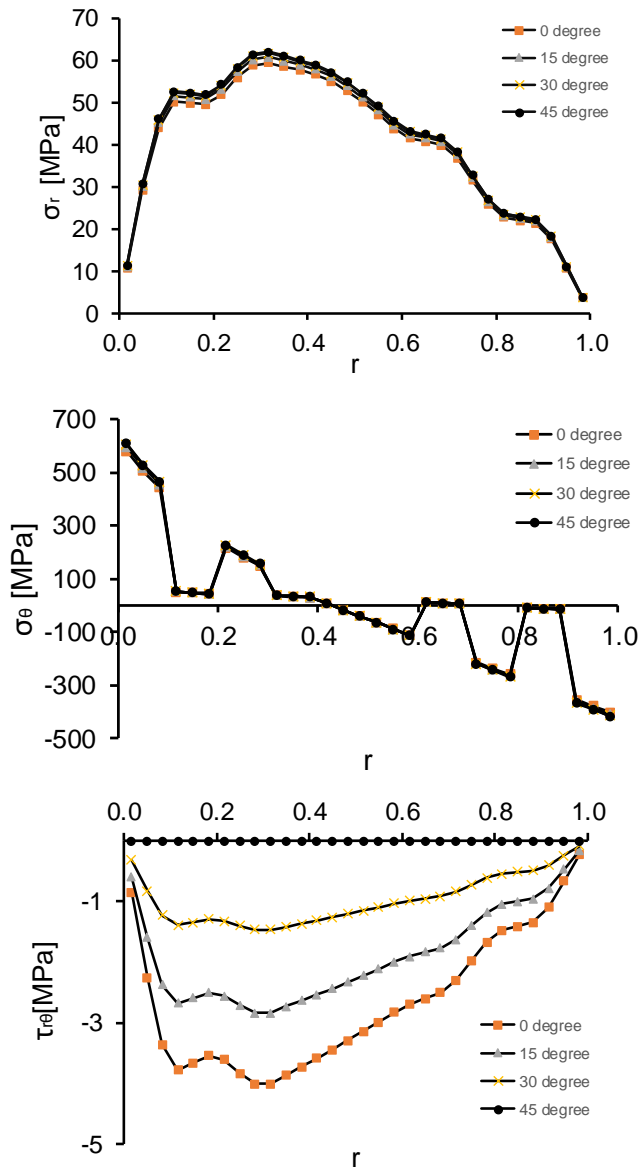


Figure 85. Radial, tangential and shear stress distributions through the thickness direction.

5.3 Finite Element Results of Cross-Ply Curved Laminates

5.3.1 Thin Cross-Ply Curved Laminates

For thin cross-ply specimen, finite element analysis is performed under 400 N axial loading as described in finite element method section. Stress fields are given in Figure 86 for radial, tangential and shear stresses in the curved region, respectively. The radial stress is concentrated at approximately 22% of the thickness and the maximum radial stress is observed at 4th layer (1st group of 90° layers) as 55 MPa. The tangential stress is tensile at the inner radius of the curve while it is compressive at the outer radius of the curve as expected. The shear stress is zero at the center of the curve due to symmetric loading and increases through the arms.

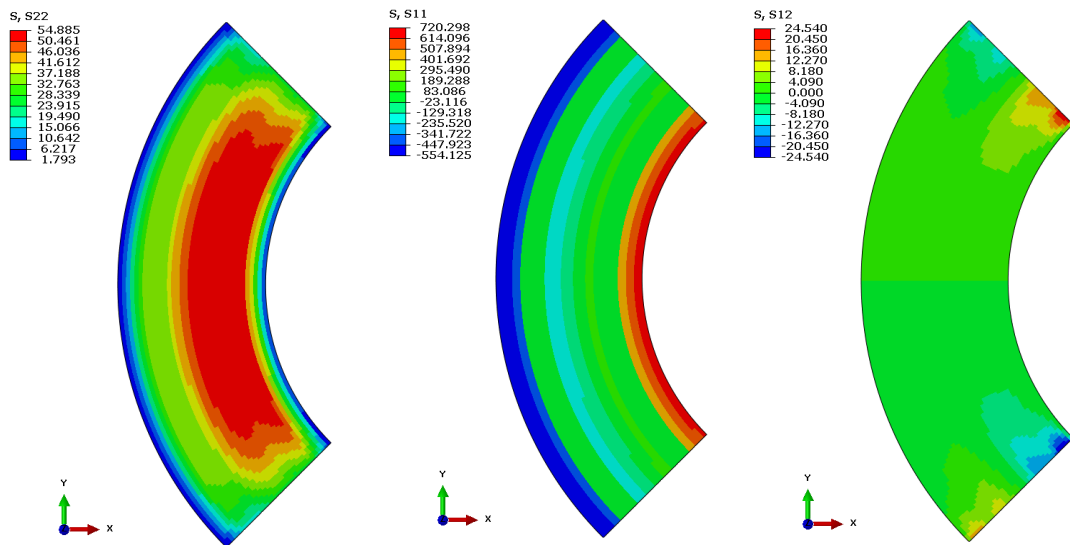


Figure 86. Radial, tangential and shear stress distributions on the curved region respectively for thin cross-ply lay-up.

Finite element results are compared with analytical results in order to validate the analytical method. Comparison graphs for radial and tangential stresses at the center of the curve are shown in Figure 87. There is a slight difference between FEA and analytical solution with an error less than 3% for the radial stress and less than 6% for the tangential stress.

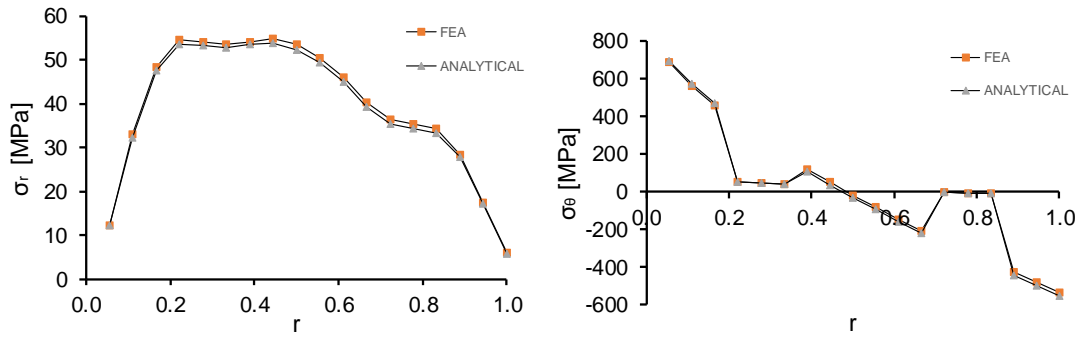


Figure 87. Comparison of FEA and analytical solution for radial and tangential stress distributions through the thickness at the center of the curve for thin cross-ply lay-up.

Since the main concern of the FEA is to obtain stress values in curved region before the failure, load drop is not simulated for this study. Critical load corresponding to the applied displacement is obtained from experimental results and used as prescribed force value to simulate the same linear load-displacement behavior until failure. Load-displacement curves of the experiments and the non-linear static finite element analysis are consistent as seen in Figure 88.

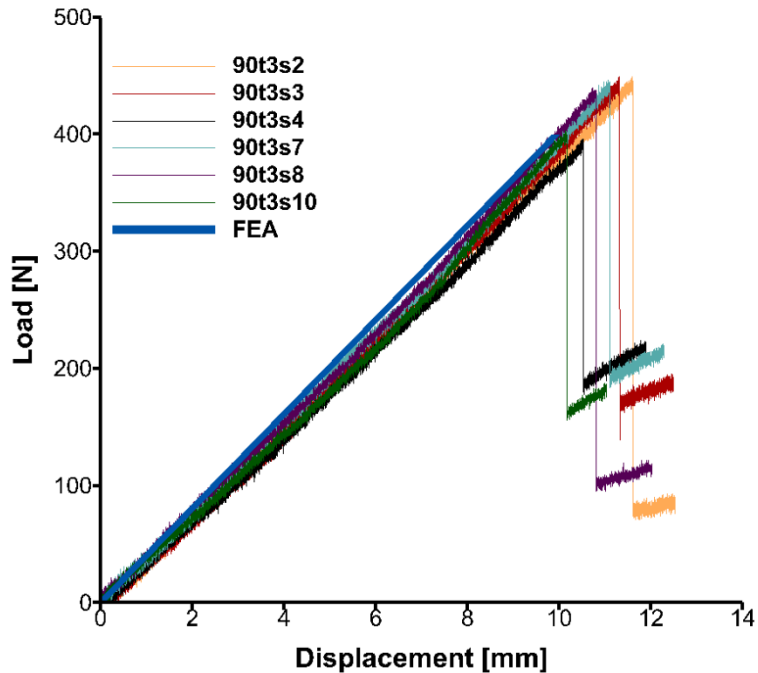


Figure 88. Load-displacement curve for thin cross-ply lay-up

5.3.2 Thick Cross-Ply Curved Laminates

For thick cross-ply specimen, finite element analysis is performed under 800 N axial loading as described in finite element method section. Stress fields are given in Figure 89 for radial, tangential and shear stresses in the curved region, respectively. The radial stress is concentrated at approximately 33% of the thickness and the maximum radial stress is observed at 10th layer (2nd group of 90° layers) as 64 MPa. The tangential stress is tensile at the inner radius of the curve while it is compressive at the outer radius of the curve as expected. The shear stress is zero at the center of the curve due to symmetric loading and increases through the arms.

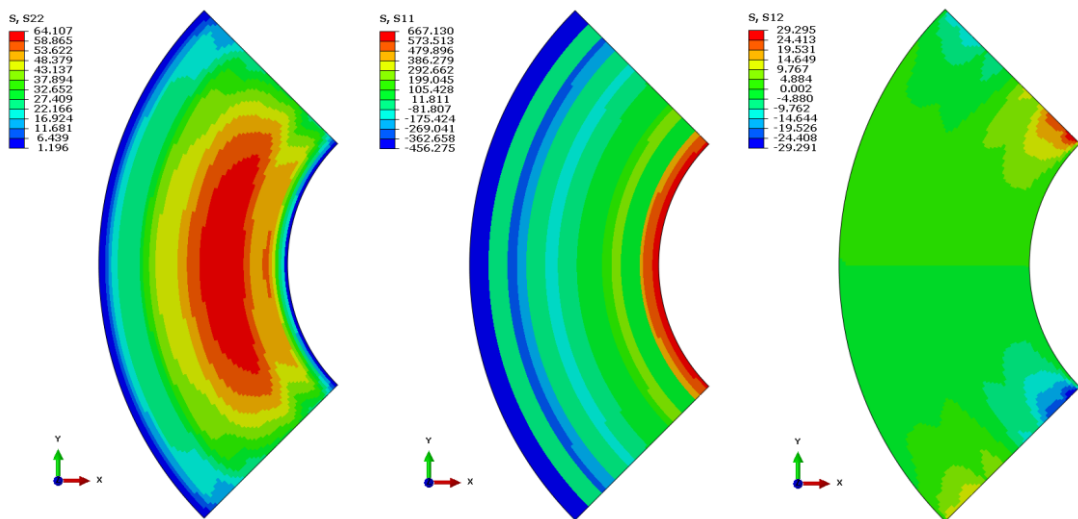


Figure 89. Radial, tangential and shear stress distributions on the curved region respectively for thick cross-ply lay-up.

Finite element results are compared with analytical results in order to validate the analytical method. Comparison graphs for radial and tangential stresses at the center of the curve are shown in Figure 90. There is a slight difference between FEA and analytical solution with an error less than 2% for the radial stress and less than 4% for the tangential stress.

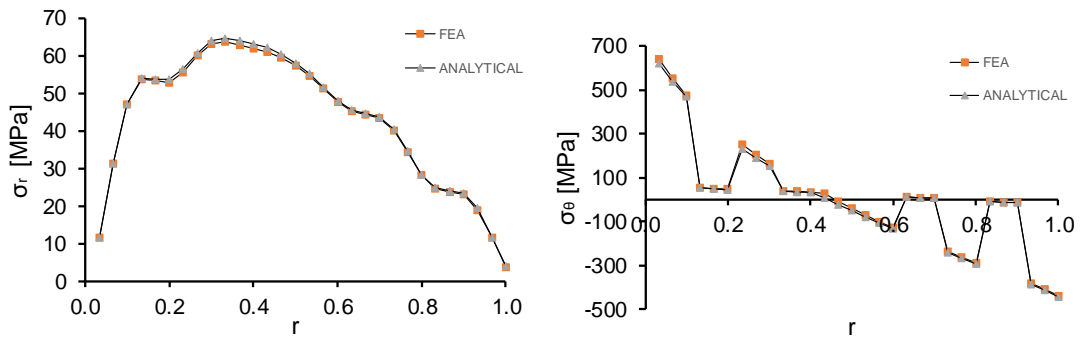


Figure 90. Comparison of FEA and analytical solution for radial and tangential stress distributions through the thickness at the center of the curve for thick cross-ply lay-up.

Since the main concern of the FEA is to obtain stress values in curved region before the failure, load drop is not simulated for this study. Critical load corresponding to the applied displacement is obtained from experimental results and used as prescribed force value to simulate the same linear load-displacement behavior until failure. Load-displacement curves of the experiments and the non-linear static finite element analysis are consistent as seen in Figure 91.

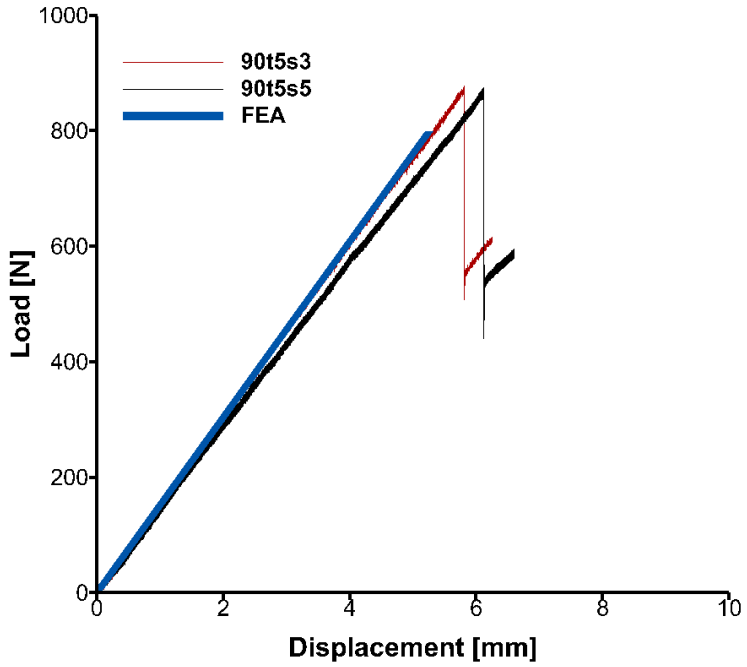


Figure 91. Load-displacement curve for thick cross-ply lay-up.

CHAPTER 6

FABRIC LAMINATES

In this chapter, experimental results of curved fabric laminates under static loading (Section 6.1.1) and under fatigue loading (Section 6.1.2) are presented. Experimental results sections are followed by analytical and finite element results sections. For each case, load-displacement curves including failure, post-failure images and micrographs of the failed specimen are presented. For the static experiments, DIC results showing the strain distributions in the curved region are also presented.

6.1 Experimental Results of Fabric Curved Laminates

6.1.1 Static Tensile Tests of Fabric Curved Laminates

For three $[(45/0)_7, 45/45/0/45]$ fabric specimens cut from the same composite batch, static experiments are conducted. One specimen (ft5s2) is used to conduct DIC experiment and two specimens (ft5s3 and s4) are used in experiments recorded with a high resolution camera. All specimens are loaded quasi-statically under displacement control at a displacement rate of 1 mm/min and images are captured at 1fps.

Load-displacement curves of three $[(45/0)_7, 45/45/0/45]$ fabric specimens under static loading are shown in Figure 92 (a). Slopes of the curves are very close to each other approximately up to 6 mm displacement. In Figure 92 (b) and (c) captured images of the specimens before and after the failure are presented. Multiple cracks are observed at similar locations for all specimens. In Table 8, details of the experiments are listed; the number of cracks, the location of the major crack, the critical load and displacement, the stiffness before and after the failure, the residual load and displacement. The stiffness values are very close to each other in elastic region.

Stiffness values before and after the failure are also very close. Critical and residual loads are consistent and critical displacements are similar.

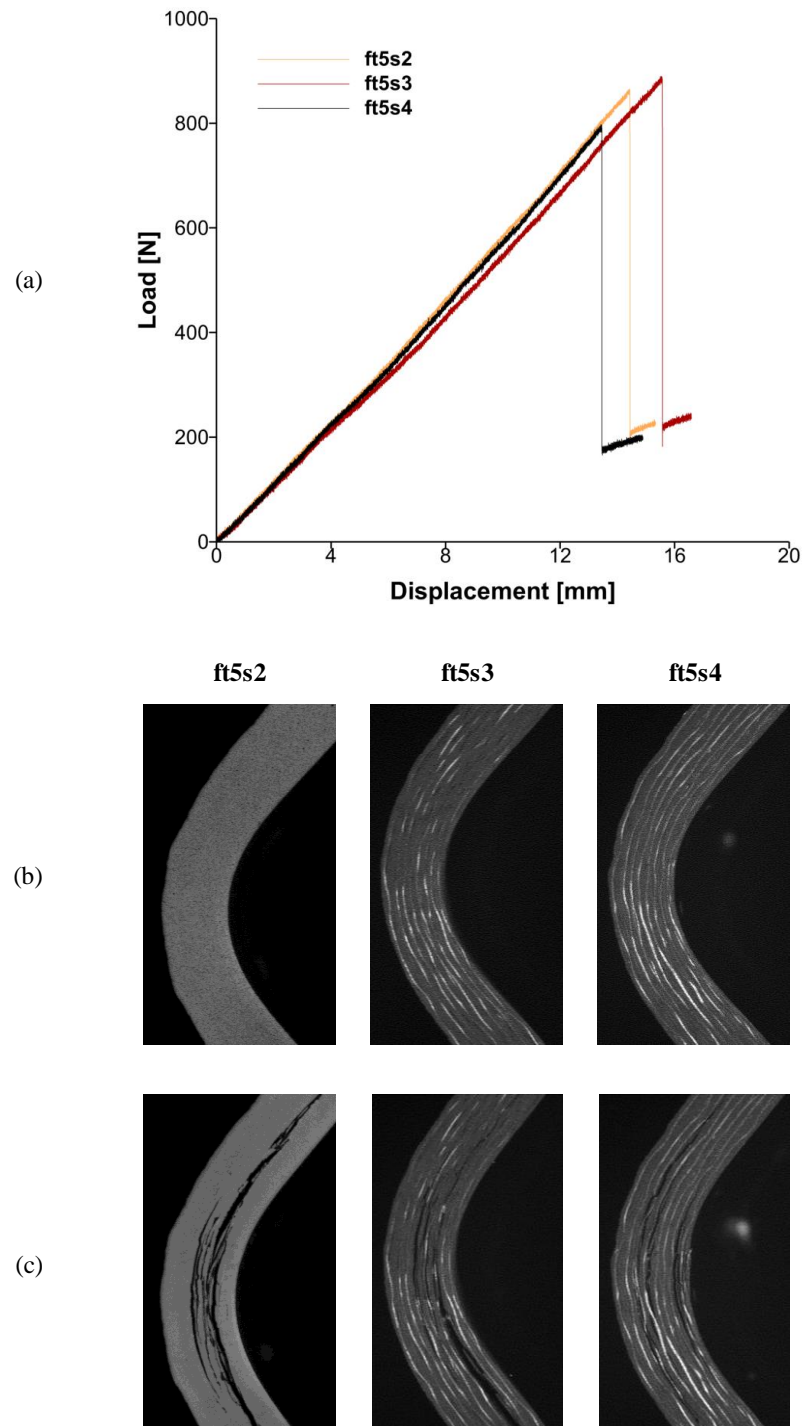


Figure 92. (a) Load-displacement curves, pictures of the specimens (b) before failure and (c) after failure.

Table 8. Summary table for static experiments of fabric specimens.

Spc Name	# of cracks	P _c (N)	δ _c (mm)	Stiffness (N/mm)	P _r (N)	2 nd stiffness (N/mm)	δ _r at P=0 (mm)
ft5s2	multiple	863	14.4	56	205	21	2.07
ft5s3	multiple	880	15.6	54	216	20	2.02
ft5s4	multiple	804	13.5	56	184	17	1.99

DIC method is used to obtain stress distribution of the specimen, ft5s2, just before the failure. The specimen is loaded at a rate of 1mm/min. As seen in Figure 92 (a), the failure occurs at 14.4 mm displacement which corresponds to a load of 863 N. The failure occurs as multiple diffused cracks at approximately in the region between 30% and 70% of the thickness from the inner radius as seen in Figure 92 (c) and leads to a 75% significant load drop to 205 N.

According to DIC analysis, the Tresca strain distribution in the curved specimen just before the failure is shown in Figure 93. The pre-failure strain field is fitted on the post-failure image at the right hand side of the figure. For fabric layup, damage at the curve region cannot be predicted by DIC strain concentrations. Concentrations are observed in the inner and outer radius while damage occurs between 30% and 60% of the thickness from the inner radius.

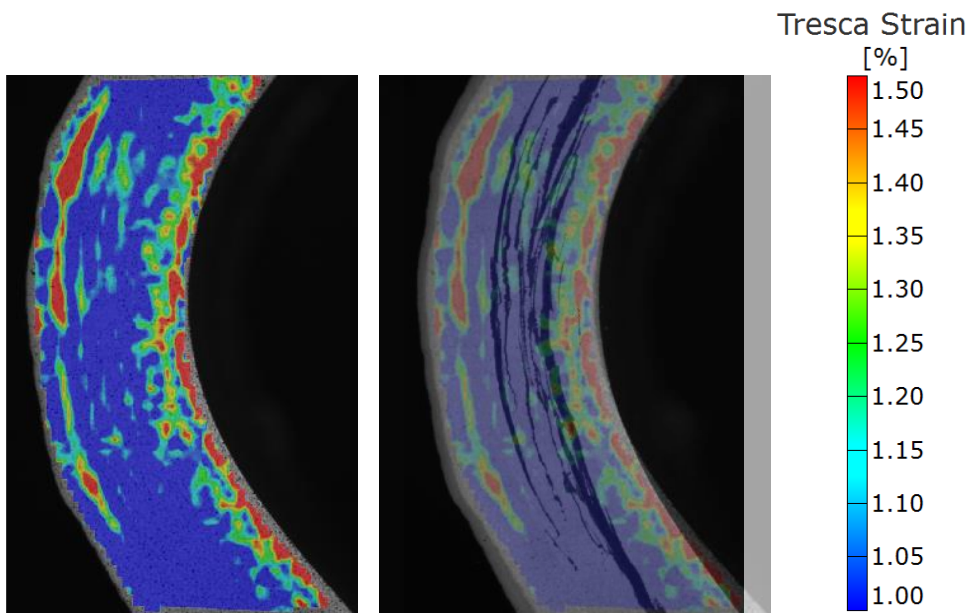


Figure 93. Tresca strain distribution just before the failure and its representation on the specimen picture just after the failure.

6.1.2 Fatigue Tests of Fabric Curved Laminates

For two $[(45/0)_7, 45/45/0/45]$ fabric specimens cut from the same composite batch, ft5s6 and s7, fatigue experiments are conducted. Both fatigue experiments are performed under displacement control between 5-10 mm (66% of the critical displacement of the static experiments) and sinusoidal wave type cyclic loading is given at 2 Hz. While the former failed at 30,000 cycle, the latter failed at 95,900 cycles. The load-displacement behavior during the test and the load-displacement parameters as a function of the number of cycles are shown in Figure 94 (a) and (b), respectively. In Figure 94 (c), images of the specimens after the failure are given. There is one outer unexpected crack which is probably caused by a manufacturing defect in the specimen ft5s7 but the main cracks are located at approximately 33% of the thickness from the inner radius as a single major delamination and they are consistent for both specimens.

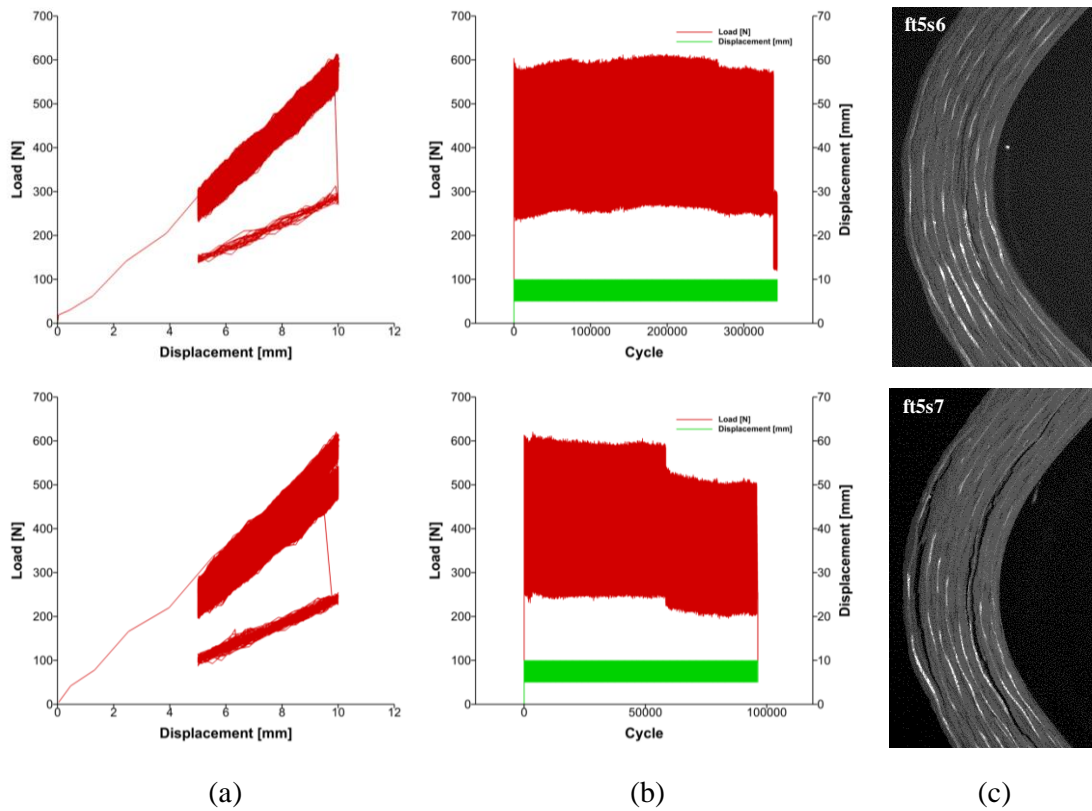


Figure 94. (a) Load-displacement curves, (b) load-cycle-displacement curves and (c) pictures of the specimens after the failure.

Change in stiffness with cycles of the fatigue experiments are presented in Figure 95. The stiffness value is 65 ± 5 N/mm for the intact specimens and it reduced to 36 ± 15 N/mm for failed specimens.

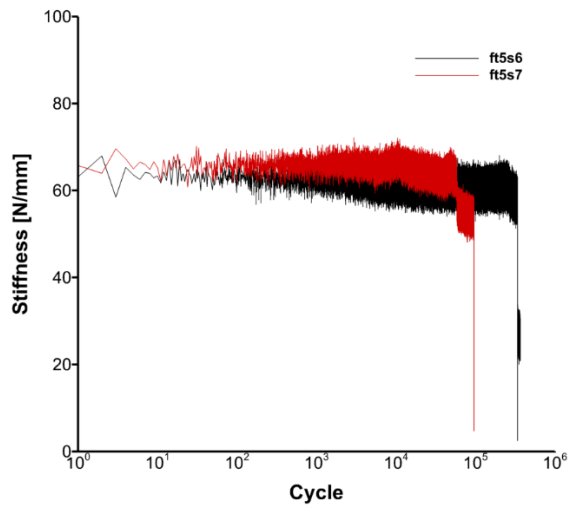


Figure 95. Change in stiffness with cycles.

6.2 Analytical Results of Fabric Curved Laminates

To understand the reason of the experimentally observed crack initiation location, analytical calculations are applied to the curved region for $[(45/0)_7, 45/45/0/45]$ fabric specimen. Analytical calculations are performed based on multilayer curved beam solution explained in the analytical method section and prescribed force is 800 N in the vertical direction as in the experimental setup. Stress distributions are examined through the thickness direction at 0° , 15° , 30° and 45° sections of the curve as shown in Figure 96. For these sections radial, tangential and shear stress distributions are compared through the normalized thickness.

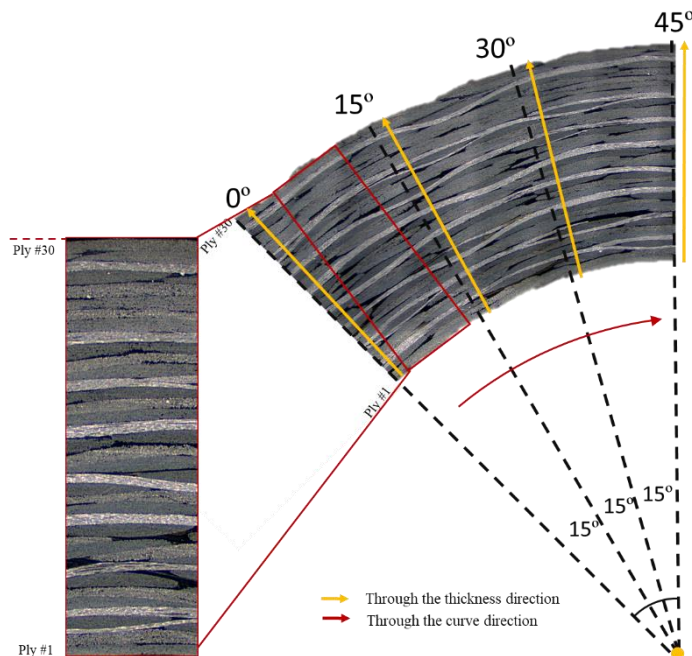


Figure 96. Representation of directions and sections used for stress distribution calculations on fabric curved specimen.

Comparison of radial, tangential and shear stresses at 0° , 15° , 30° and 45° sections are given in Figure 97. Larger difference as percentage is observed in the shear stress. However, it should be noted that the magnitude of the shear stress is much smaller than the radial and tangential stresses.

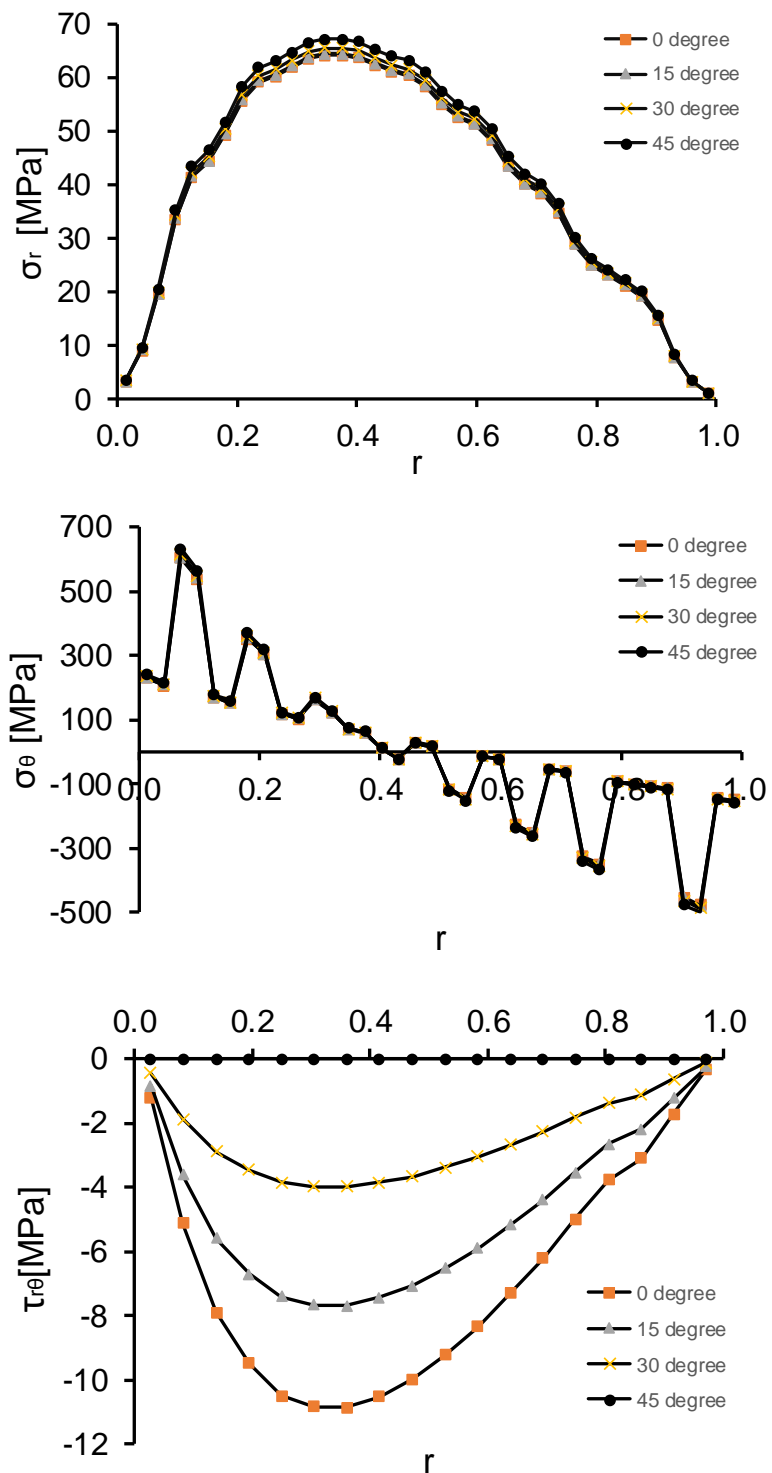


Figure 97. Radial, tangential and shear stress distributions through the thickness direction.

6.3 Finite Element Results of Fabric Curved Laminates

For [(45/0)₇,45/45/0/45] fabric specimen, finite element analysis is performed under 800 N axial loading as described in finite element method section. Stress fields are as given in Figure 98 for radial, tangential and shear stresses in the curved region respectively. The radial stress is concentrated at approximately 35% of the thickness and the maximum radial stress is observed at 6th layer as 65 MPa. The tangential stress is tensile at the inner radius of the curve while it is compressive at the outer radius of the curve as expected. The shear stress is zero at the center of the curve due to symmetric loading and increases through the arms.

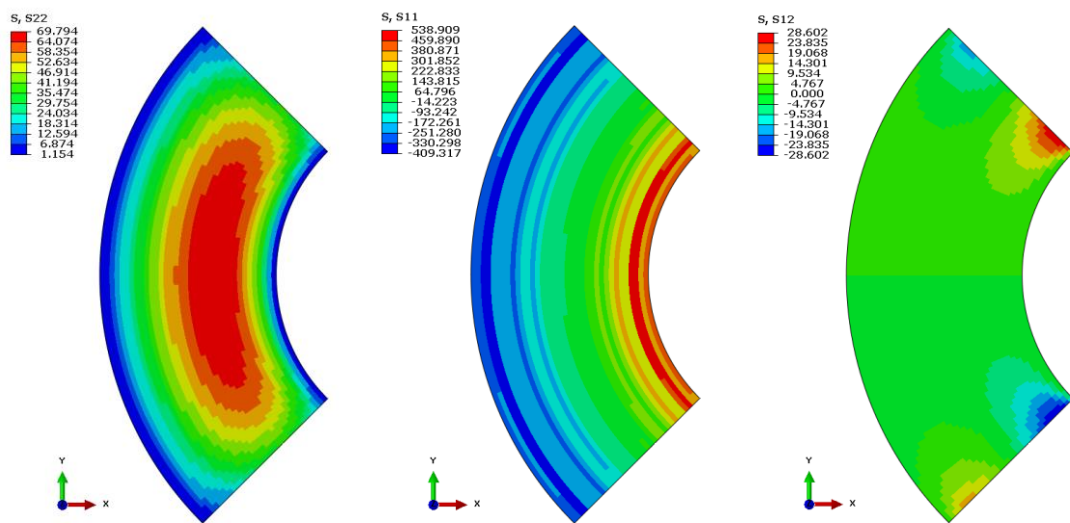


Figure 98. Radial, tangential and shear stress distributions on the curved region respectively for fabric lay-up.

Finite element results are compared with analytical results in order to validate the analytical method. Comparison graphs for radial and tangential stresses at the center of the curve are shown in Figure 99. A slight difference is observed between FEA and analytical solution with an error less than 5% for the radial stress. However, there is higher error percentage for the tangential stress and it is approximately 25% for 45° layers.

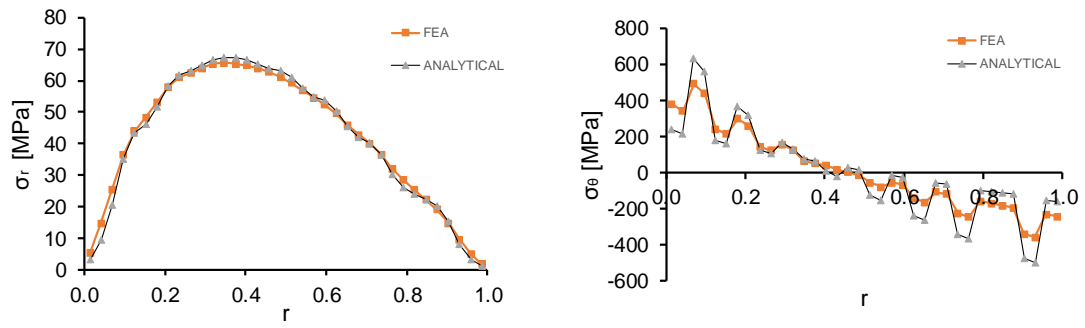


Figure 99. Comparison of FEA and analytical solution for radial and tangential stress distributions through the thickness at the center of the curve for fabric lay-up.

Since the main concern of the FEA is to obtain stress values in curved region before the failure, load drop is not simulated for this study. Critical load corresponding to the applied displacement is obtained from experimental results and used as prescribed force value to simulate the same linear load-displacement behavior until failure. Load-displacement curves of the experiments and the non-linear static finite element analysis are consistent as seen in Figure 100.

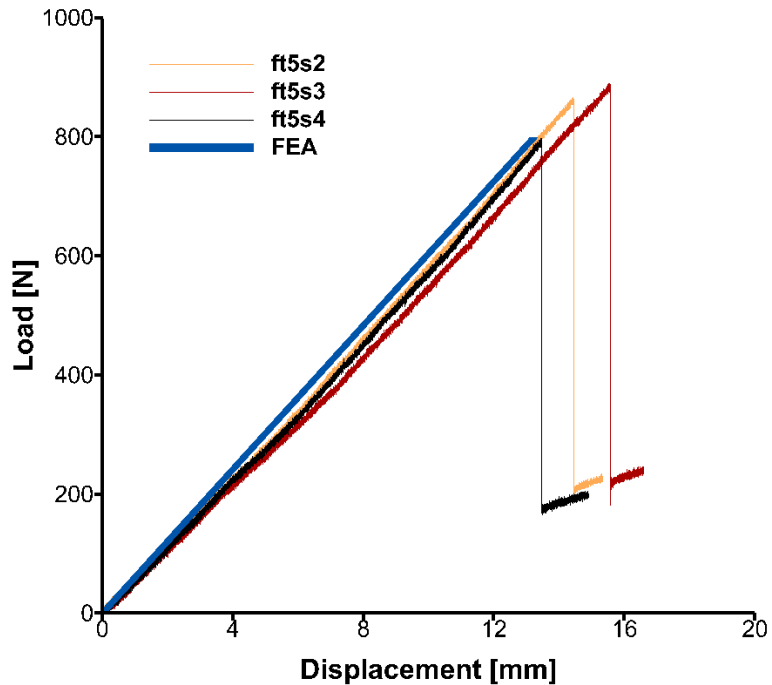


Figure 100. Load-displacement curve for fabric lay-up.

CHAPTER 7

DISCUSSION

In this chapter, experimental observations supported by analytical calculations are discussed in two main titles as comparison of UD and fabric laminates and cross-ply laminates with two different thicknesses.

7.1 Damage Mechanisms in UD and Fabric Curved Composite Laminates under Static and Fatigue Loading

The difference between the observed failure mechanisms for static and fatigue failure of $[0]_{30}$ UD and $[(45/0)_7, 45/45/0/45]$ fabric composite laminates are discussed in this section. Explanation of failure mechanisms are reviewed separately for UD and fabric specimens.

Comparison of static and fatigue failure mechanisms in UD specimens

For both static and fatigue loading of $[0]_{30}$ UD curved specimens, failure was observed to occur at 33% of the thickness from inner radius as a single major delamination as seen in Figure 101.

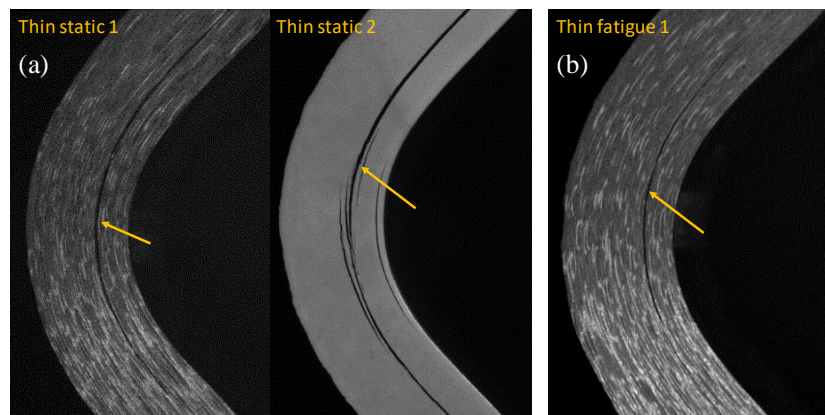


Figure 101. (a) Static and (b) fatigue failure images for $[0]_{30}$ specimens.

We explain the observed crack initiation and growth mechanisms in the experiments by discussing the stress state. The stress state is analytically calculated in the curved region using the multilayer curved beam solution as explained in Section 3.2.1 and Section 4.2.

Radial, tangential and shear stress distributions are calculated through the thickness in 0° , 15° , 30° and 45° sections for an axial load of 1200 N (from the failure load observed in the experiments) given in Figure 102. The radial stress reaches its maximum value of 83 MPa in the 10th ply whereas the tangential stress reaches the maximum value of 580 MPa in the most inner ply. Both of these stress components change slightly only with different section angles away from the center. The shear stress increases with section angle and reaches its maximum at the 0° section (the farthest away from the center) of the 10th ply. As mentioned in the literature, if failure can be assumed to take place due to opening radial stresses, the failure is predicted to occur as a delamination in the 10th layer (33% of the thickness). As expected, crack initiation is observed in the 33% of the thickness from inner radius in the experiments. Thus, for the case of [0]₃₀ UD specimens, failure mechanism seems to be explained satisfactorily by the stress distribution for both static and fatigue loading.

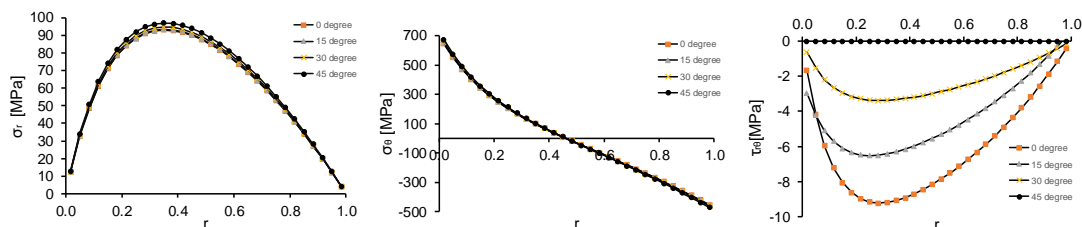


Figure 102. Radial, tangential and shear stress distributions through the thickness direction.

Comparison of static and fatigue failure mechanisms in fabric specimens

Images taken just after the load drop of the fabric [(45/0)₇,45/45/0/45] specimens from static and fatigue experiments are shown in Figure 103. For the static experiments, failure occurs spontaneously in the form of multiple diffuse cracks (Figure 103 a) whereas under fatigue loading, the crack initiates and propagates as a single major delamination crack (Figure 103 b).

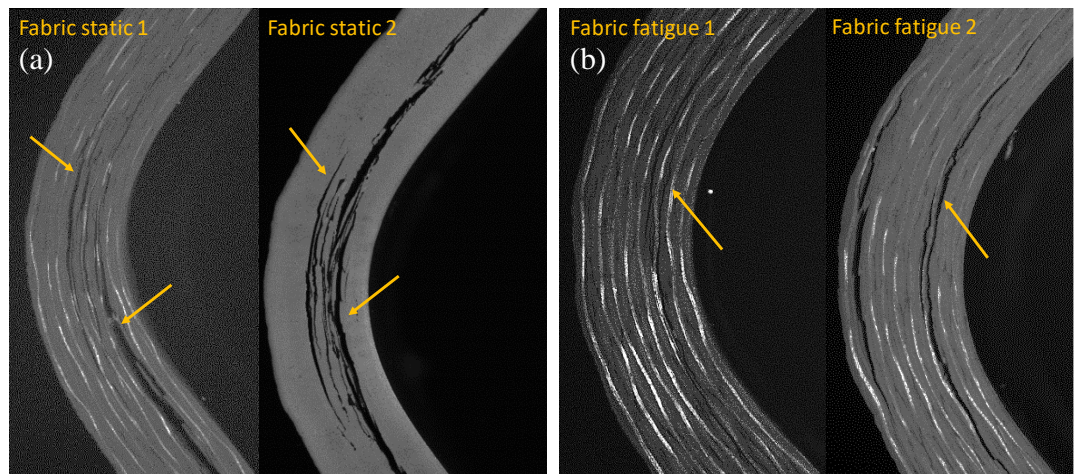


Figure 103. (a) Static and (b) fatigue failure images for fabric specimens.

Radial, tangential and shear stress distributions are calculated through the thickness in 0° , 15° , 30° and 45° sections for an axial load of 800 N (failure load observed in the experiments) given in Figure 104 with the section angles and ply numbers through the thickness defined for fabric laminates in Figure 96. The radial stress reaches its maximum value of 67 MPa in the 6th ply and it is observed that the tangential stresses reach their maximum values in the 45° plies. Both radial and tangential stress components change very slightly with different section locations away from the center. The shear stress changes with section angle and reaches its maximum value of 10.8 MPa in the 6th layer at the 0° section. In light of these results, maximum radial stress would predict the failure to occur in the 33% of the thickness from inner radius approximately, where it reaches its maximum value. This is in agreement with our experiments under fatigue and static loading where failure is observed to occur approximately in the 33% of the thickness from inner radius. Although the failure location of static and fatigue experiments are almost the same, the number of cracks formed during failure is different. For the static case, failure occurs spontaneously in the form of multiple diffused cracks whereas under fatigue loading, the crack initiates and propagates as a single major delamination crack.

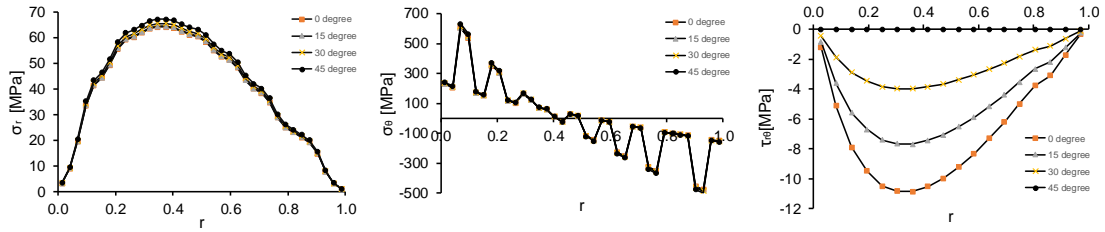


Figure 104. Radial, tangential and shear stress distributions through the thickness direction.

Summary

Summarizing the observations for UD and fabric curved laminates, failure of the UD laminates by a single major delamination at the maximum radial stress location is a common characteristic for both static and fatigue loadings. However, failure of fabric laminates is observed to be different under static and fatigue loading conditions. Static failure of the curved fabric laminate occurs as diffused cracks at the maximum radial stress locations while fatigue failure occurs as a single major delamination at the maximum radial stress location.

7.2 Damage Mechanisms in Cross-ply Curved Composite Laminates under Static and Fatigue Loading

The difference between the observed failure mechanisms for static and fatigue failure of cross-ply thin $[0_3/90_3/0_3]_s$ and thick $[0_3/90_3/0_3/90_3/0_3]_s$ curved composite laminates are discussed in this section. Explanation of different failure mechanisms are reviewed separately for thin and thick specimens.

Comparison of static and fatigue failure mechanisms in thin cross-ply specimens

For both static and fatigue loading of thin curved $[0_3/90_3/0_3]_s$ specimens, failure was observed to occur in the inner (first) group of 90° plies as seen in Figure 105 with failure initiating as a matrix crack on one side of the symmetry axis. In the static loading case, the matrix crack grows in the curved region of the specimen parallel to the first $0/90$ interface and jumps to the upper $0/90$ interface by an abrupt $40\text{--}50^\circ$ shear crack at the end of the curved section as seen in Figure 105(a) outlined with red dashed ellipses. On the other hand, for the fatigue loading case, the matrix crack is observed to propagate from the first to the second $0/90$ interface gradually and is presumed to

propagate by coalescence of matrix cracks and defects in the group of 90° layers. After coalescence, the major matrix crack reaches the 0/90 interface in a meandering path at a shallow angle to the interface as seen in Figure 105(b) outlined with red dashed ellipses.

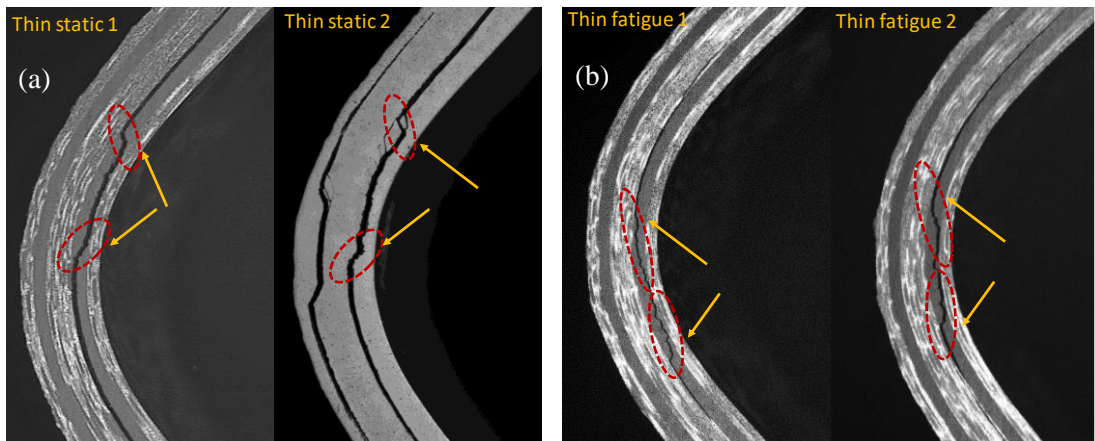


Figure 105. (a) Static and (b) fatigue failure differences for thin specimens.

We explain the observed crack initiation and growth mechanisms in the experiments by discussing the stress state and failure criteria. The stress state is analytically calculated in the curved region using the multilayer curved beam solution as explained in Section 3.2.1 and Section 5.2.1.

Radial, tangential and shear stress distributions are calculated through the thickness in 0°, 15°, 30° and 45° sections for an axial load of 400 N (from the failure load observed in the experiments) given in Figure 106. The radial stress reaches its maximum value of 55 MPa in the 4th ply whereas the tangential stresses in the 90° plies reach the maximum value of 51 MPa in the 4th ply. Both of these stress components change slightly only with different section angles away from the center. The shear stress increases with section angle and reaches its maximum at the 0° section (the farthest away from the center) of the 4th ply. The radial stresses are larger than tangential stresses in the first group of 90° layers of thin specimens as seen in Figure 106 for all sections. As mentioned in the literature, if failure can be assumed to take place due to opening radial stresses, the failure is predicted to occur as horizontal (parallel to the

0/90 interface) cracks in the first group of 90° layers. As predicted, crack initiation is observed in the 4th ply in the experiments.

Thus, for the case of thin specimens, failure mechanism seems to be explained satisfactorily by the stress distributions for both static and fatigue loading. However, for the case of thick specimens, stress distributions will not give consistent results with experiments as will be shown in the next section. Tsai-Wu failure criterion is applied for one step further analysis for both thin and thick specimens.

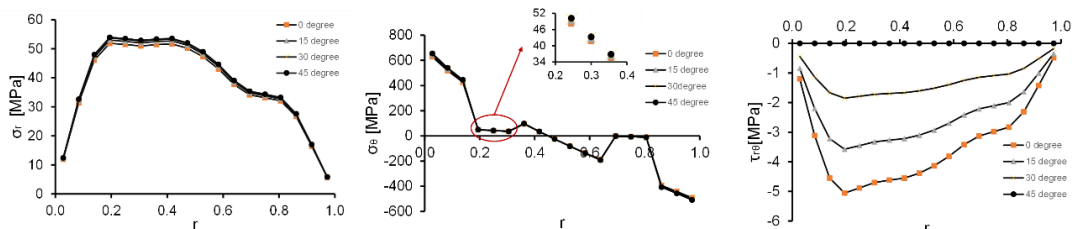


Figure 106. Radial, tangential and shear stress distributions through the thickness direction.

Tsai-Wu failure criterion, a 3-D quadratic stress-based criterion that identifies failure, is used here to determine the failure initiation location [53]. The criterion employs the failure function proposed in Appendix-B. TSAI-WU FAILURE CRITERIA for orthotropic materials in their material axes. Failure index (FI) is calculated using analytically obtained stresses through the thickness for each ply by neglecting stresses in the width direction and is shown in Figure 107. At the failure load of 400 N, maximum failure index greater than 1 is observed in the 4th layer according to Tsai-Wu Criterion. Failure is observed to initiate at the same location as a matrix crack parallel to the 0/90 interface.

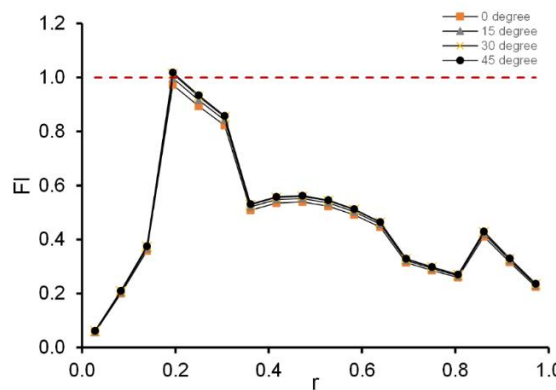


Figure 107. Failure index distribution through the thickness using Tsai-Wu failure criterion.

Comparison of static and fatigue failure mechanisms in thick cross-ply specimens

Images taken just after the load drop of the thick $[0_3/90_3/0_3/90_3/0_3]_s$ specimens from static and fatigue experiments are shown in Figure 108. For the static experiments, failure is observed in the first group of 90° layers (Figure 108 a) whereas for the fatigue experiments failure is observed in the second group of 90° layers (Figure 108 b). Thus, a difference is observed in the location of the failure between the static and fatigue experiments which was not observed for the thin specimens. In addition, similar to thin specimens, a difference in the matrix crack path before reaching the arms to create a delamination is observed between the static and fatigue loading.

For the static loading case, it is observed that failure starts as matrix cracks in the curved region of the 4th ply (first group of 90° layers). Then, it propagates parallel to the lower 0/90 interface and jumps to the upper 0/90 interface by an abrupt $40-50^\circ$ shear crack near the arms as shown in Figure 108 (a) by the red circles. However, damage occurs by nucleation of matrix cracking in the 2nd group of 90° layers in the curved region for the fatigue loading case. Then the observed crack propagates towards the arms by meandering in the 2nd group 90° layers and reaches to the upper 0/90 interface as shown in Figure 108 (b) by the red circles.

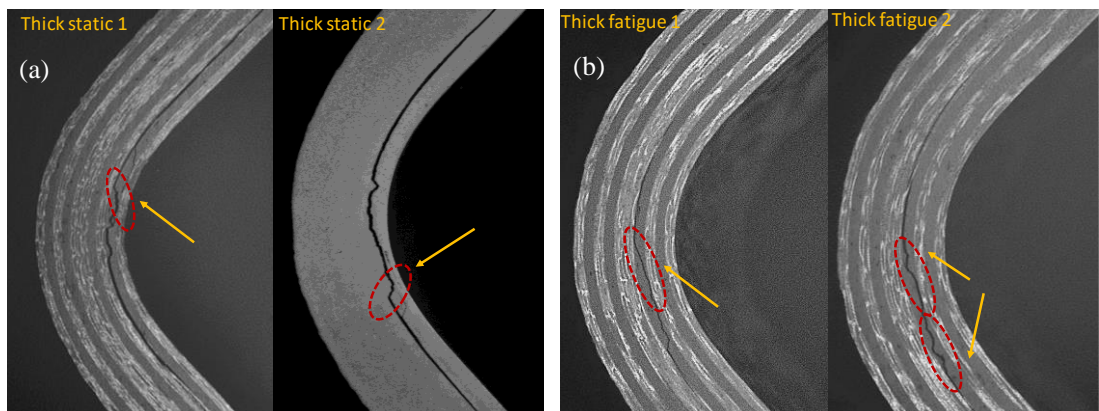


Figure 108. (a) Static and (b) fatigue failure differences for thick specimens.

Radial, tangential and shear stress distributions are calculated through the thickness in 0° , 15° , 30° and 45° sections for an axial load of 800 N (failure load observed in the experiments) in Figure 109 with the section angles and ply numbers through the

thickness defined for thick laminates in Figure 83. The tangential stresses are found to reach a maximum value of 600 MPa in the 0° plies but are much lower than the tensile failure strength of 0° plies (2207 MPa) so these stresses do not determine failure. Amongst the 90° plies, the radial stresses attain their maximum value of 62 MPa in the 10th ply (2nd group of 90° plies), whereas the tangential stresses attain their maximum value of 53 MPa in the 4th ply (1st group of 90° plies). Both of these stress components change very slightly with different section locations away from the center. The shear stress varies with thickness and section angle reaching its maximum value of 4 MPa in the 2nd group of 90° plies at the 0° section which is farthest away from the center. In light of these results, maximum radial stress would predict the failure to occur in the 2nd group of 90 plies, where it reaches the maximum value. This is in agreement with our experiments under fatigue loading where failure is observed to be in the 2nd group of layers, however, in disagreement to our experiments under static loading where failure is observed to occur in the 1st group of 90° plies.

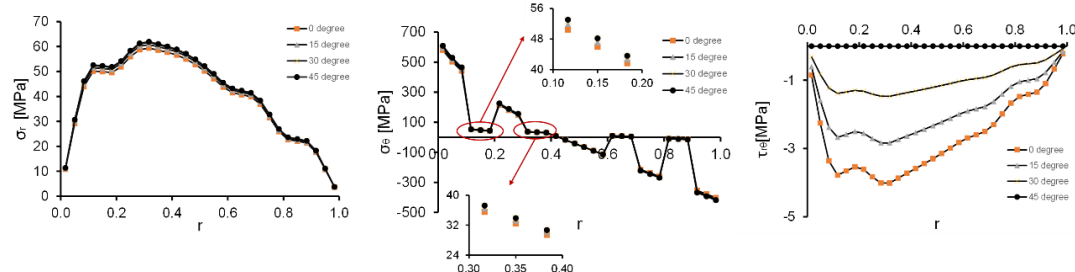


Figure 109. Radial, tangential and shear stress distributions through the thickness direction in thick composite at 800 N.

A better prediction of the failure location for static loading is given by the Tsai-Wu failure criterion. Failure index using Tsai-Wu criterion (Appendix B. TSAI-WU FAILURE CRITERIA) is calculated using analytically obtained stresses through the thickness for each ply by neglecting stresses in the width direction and is shown in Figure 110. At the failure load of 800 N, maximum failure index greater than 1 is observed in the 4th layer (1st group of 90° layers) according to Tsai-Wu Criterion. This predicts precisely the results of our static experiments where failure is observed to initiate in the 4th layer as a matrix crack parallel to the $0/90$ interface (in contrast to

using the maximum radial stress criterion which predicts failure in the 10th layer, 2nd group of 90° layers).

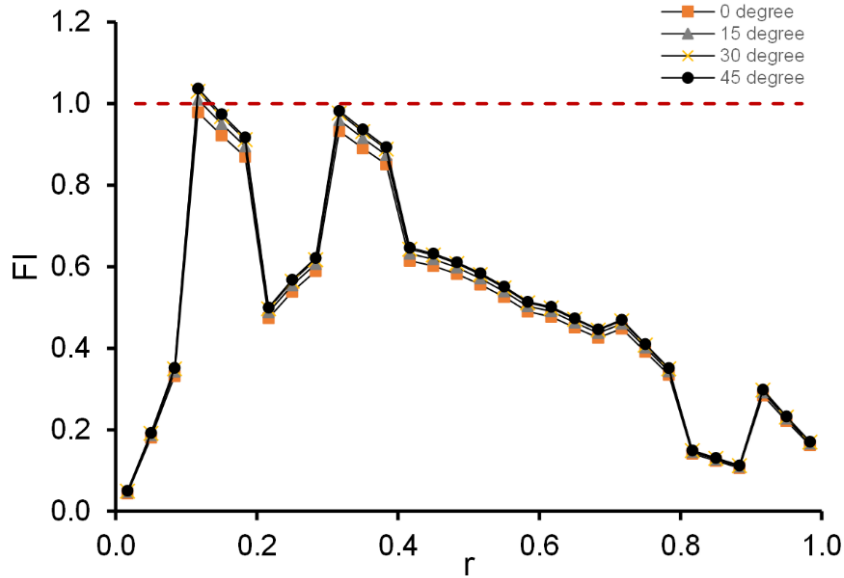


Figure 110. Failure index distribution through the thickness for thick specimen using Tsai-Wu failure criterion.

In light of our results for thick composites, we postulate different failure mechanisms for fatigue and static loading. During cyclic loading for thick composites, the existent manufacturing defects in the first and second 90° groups of layers grow perpendicular to the direction of the largest principal stress component which in this case is the radial stress. The growth of defects and forming of micro-cracks decrease the material residual strength in the direction of the radial stresses [54], [55]. Hence, when the material residual strength falls below the maximum radial stress which occurs in the 2nd group of 90 plies, matrix cracks coalesce and grow. At the failure instant, the major matrix crack propagates following a meandering path uniting the small matrix cracks inside the group of 90° layers (Figure 111) before reaching to 0/90 interface seen in Figure 108.

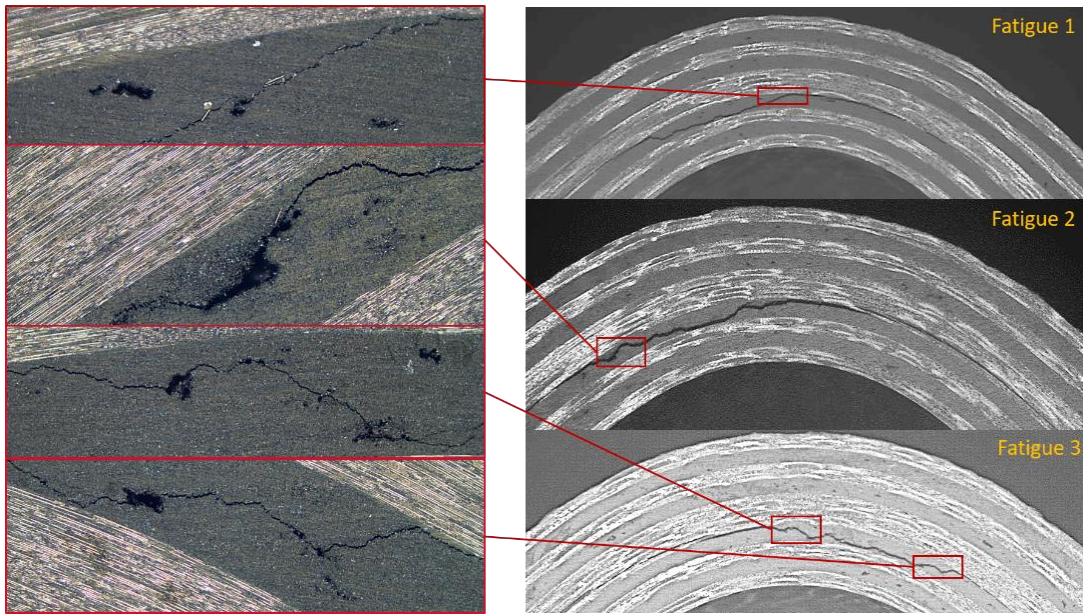


Figure 111. Defect sensitivity of fatigue experiments by micrographs.

In static experiments, failure occurs suddenly under quasi-static loading at the inner (first) group of 90° layers. Tsai-Wu [53] failure criteria predicts the static failure in the 1st group of 90° layers for the calculated stress states as observed in the experiments. The crack initiates at the inner ply of the 1st group of 90° layers and quickly reaches the 0/90 interface as the shear stresses increase and drive the crack to the interface. Therefore, meandering cracking path is not observed in the static case.

Failure mechanisms for static and fatigue

Summarizing the observations for thin and thick cross-ply curved laminates, failure of the laminate by matrix cracking in the group of 90° plies followed by delamination at the interface of 0° and 90° plies is a common characteristic for both static and fatigue loading. The difference between the two loadings is revealed in the location of the failure (not apparent in the thin specimen) and the sudden or gradual transition of the matrix cracking to interface delamination (for both thicknesses). From our experimental observations and analyses, the proposed mechanisms for failure under fatigue and static loading of thin and thick composite specimens can be summarized as follows:

- *Under fatigue loading*, radial stresses nucleate micro-cracks or enlarge the existent manufacturing defects in 90° group of layers cyclicly. This process decreases the residual strength of the material with number of cycles. When the material residual strength falls below the radial stresses in the 90° group of layers, macroscopic matrix cracks initiate and propagate by the coalescence of these cracks at the ply location where the radial stresses are maximum. As a result, the major matrix crack follows a path uniting the stress nucleated micro-matrix cracks inside the group of 90° layers (Figure 111), reaching the $0/90$ interface due to the increasing shear stresses towards the arms as seen in Figure 106. In thin specimens, the maximum radial stresses occur in the first group of 90° plies, whereas in thick specimens, the maximum radial stresses occur in the second group of 90° plies which is precisely concluded as a result of the experiments supported by analytical solution.
- *Under static loading*, crack initiation and propagation occur dynamically following the Tsai-Wu failure criterion. In both thin and thick specimens, the crack initiates inside the group of 90° layers where the failure index reaches unity, propagating towards the arms parallel and adjacent to the 1st $0/90$ interface in agreement with experimental observations. As the major matrix crack approaches the arms, it jumps to the 2nd $0/90$ interface by an abrupt 40° - 50° shear crack instead of a meandering crack path.

CHAPTER 8

CONCLUSIONS

8.1 Conclusions on Damage Mechanisms in UD and Fabric Curved Composite Laminates under Static and Fatigue Loading

In this thesis, UD and fabric curved composite laminates are examined experimentally under both static and fatigue loading. The observations of the experiments are supported by analytical calculations.

Novelties of the present research:

- A distinct difference in the failure is shown between static and fatigue loading cases which has not been observed in the past for fabric layup.

Based on the obtained results, the main contributions of the present research:

- While failure occurs by a single major delamination for UD lay-up in both static and fatigue loading cases, failure occurs differently under static and fatigue loadings for fabric lay-up.

8.2 Conclusions on Damage Mechanisms in Cross-ply Curved Composite Laminates under Static and Fatigue Loading

In this thesis, cross-ply curved composite laminates are examined experimentally under static and fatigue loading. The observations of the experiments are supported by analytical calculations.

Novelties of the present research:

- Detailed matrix crack examinations are performed for curved laminated CFRP composites experimentally using in-situ microscopy and digital image correlation technique. Analytical model is used to explain observations of failure.
- Evidence of defect sensitivity of fatigue failure is provided by micrographs for curved laminated composites.

- A distinct difference in the failure is shown between static and fatigue loading cases which has not been observed in the past.

Based on obtained results, the main contributions of the present research:

- Although failure occurs by matrix cracking followed by delamination of the 0/90 interface in both static and fatigue loading cases, damage initiation and progress is observed to be different. This difference has not been noted in the literature for composites.
- For the case of static loading, failure initiates as a matrix crack in the group of 90° layers and jumps to the upper 0/90 interface by an abrupt 40-50° angle and propagates as a delamination. On the other hand, for fatigue loading, damage initiates by nucleation of matrix cracks in the group of 90° layers. These cracks coalesce into one major matrix crack which reaches the 0/90 interface gradually which then continues to propagate as a delamination.
- On the other hand, fatigue failure takes place at the maximum radial stress location since radial stresses are effective on growth of the existent manufacturing defects under cyclic loading. Under fatigue loading, failure can be accurately predicted by taking into account strength degradation in the radial direction.
- For static loading, failure occurs due to combination of the stresses and the Tsai-Wu failure criteria successfully predicts the failure location.

REFERENCES

- [1] A. P. Vassilopoulos, “Fatigue Life Prediction of Composites and Composite Structures”, Woodhead Publishing Limited, 2010.
- [2] S. S. Manson and G. R. Halford, “Fatigue and Durability of Structural Materials”, ASM International, 2006.
- [3] R. C. Rice, B. N. Leis, and D. Nelson, “Fatigue Design Handbook”, Society of Automotive Engineers, 1988.
- [4] N. E. Frost, K. J. Marsh, and L. P. Pook, “Metal Fatigue”, Oxford: Clarendon Press, 1974.
- [5] R. Talreja, “Fatigue of Composite Materials: Damage Mechanisms and Fatigue-Life Diagrams”, Proc. R. Soc. Lond., vol. 378, pp. 461–475, 1981.
- [6] H. Bryan, “Fatigue in Composites”, Woodhead Publishing Limited, 2003.
- [7] P. T. Curtis, “The Fatigue Behaviour of Fibrous Composite Materials”, J. Strain Anal. Eng. Des., vol. 24, no. 4, pp. 235–244, 1989.
- [8] P. D. Mangalgiri, “Composite Materials for Aerospace Applications”, Bull. Mater. Sci., vol. 22, no. 3, pp. 657–664, 1999.
- [9] B. Roeseler, B. Sarh, and M. Kismarton, “Composite Structures – The First 100 Years”, Boeing 787 Progr. Compos. Des. Tutor., pp. 1–41, 2007.
- [10] C. W. Kensche, “Fatigue of Composites for Wind Turbines”, Int. J. Fatigue, vol. 28, no. 10 SPEC. ISS., pp. 1363–1374, 2006.
- [11] R. P. L. Nijssen, “Fatigue Life Prediction and Strength Degradation of Wind Turbine Rotor Blade Composites”, KC-WMC, 2006.

- [12] P. S. Veers et al., “Trends in the Design, Manufacture and Evaluation of Wind Turbine Blades”, *Wind Energy*, vol. 6, pp. 245–259, 2003.
- [13] D. A. Griffin, “Blade System Design Studies Volume II : Preliminary Blade Designs and Recommended Test Matrix”, SAND2004-0073, vol. II, no. June, pp. 3–75, 2004.
- [14] C. C. Ciang, J.-R. Lee, and H.-J. Bang, “Structural Health Monitoring for a Wind Turbine System: A Review of Damage Detection Methods”, *Meas. Sci. Technol.*, vol. 19, p. 20, 2008.
- [15] Federal Aviation Administration, “Aircraft Structures”, vol. 2. 2012.
- [16] C. T. Sun and S. R. Kelly, “Failure in Composite Angle Structures Part I: Initial Failure”, *J. Reinf. Plast. Compos.*, vol. 7, pp. 220–232, 1988.
- [17] A.-H. M. Ziadoon and Z. Chwei, “Effect The Stacking Sequences of Composite Laminates under Low Velocity Impact on Failure Modes by Using Carbon Fiber Reinforced Polymer”, *Int. J. Eng. Sci.*, no. 1, pp. 2319–1813, 2016.
- [18] S. M. J, “Fatigue of Composites”, *ASTM STP 497*, no. July, pp. 143–169, 1972.
- [19] K. H. Boller, “Fatigue Fundamentals for Composite Materials”, *Compos. Mater. Test. Des. ASTM STP 460*, Am. Soc. Test. Mater., pp. 217–235, 1969.
- [20] H. T. Hahn, “Fatigue Behavior and Life Prediction of Composite Laminates”, *ASTM STP 674*, pp. 383–417, 1979.
- [21] J. R. Hancock and G. D. Swanson, “Toughness of Filamentary Boron / Aluminum Composites”, *Compos. Mater. Test. Des. ASTM STP 497*, pp. 299–310, 1972.
- [22] F. K. Chang and G. S. Springer, “The Strengths of Fiber Reinforced Composite Bends”, *J. Compos. Mater.*, vol. 20, pp. 30–45, 1986.

- [23] B. Gozluklu and D. Coker, “Modeling of the Dynamic Delamination Behavior of L-shaped Composite Laminate Beams”, pp. 1–3, 2011.
- [24] B. Gozluklu, I. Uyar, and D. Coker, “Investigation of Intersonic Fracture in Highly Curved Composite Laminates under Quasi-Static Loading”, 11th World Congr. Comput. Mech. WCCM 2014, 5th Eur. Conf. Comput. Mech. ECCM 2014 6th Eur. Conf. Comput. Fluid Dyn. ECFD 2014, no. Wccm Xi, 2014.
- [25] B. Gozluklu and D. Coker, “Modeling of The Dynamic Delamination of L-Shaped Unidirectional Laminated Composites”, *Compos. Struct.*, vol. 94, no. 4, pp. 1430–1442, 2012.
- [26] B. Gozluklu, I. Uyar, and D. Coker, “Intersonic Delamination in Curved Thick Composite Laminates under Quasi-Static Loading”, *Mech. Mater.*, vol. 80, no. PB, pp. 163–182, 2015.
- [27] I. Uyar, B. Tasdemir, D. Yavas, and D. Coker, “Role of Laminate Thickness on Sequential Dynamic Delamination of Curved [90/0] CFRP Composite Laminates”, vol. 8, pp. 43–48, 2016.
- [28] B. Gozluklu and D. Coker, “Modeling of Dynamic Crack Propagation Using Rate Dependent Interface Model”, *Theor. Appl. Fract. Mech.*, vol. 85, pp. 191–206, 2016.
- [29] R. H. Martin and W. C. Jackson, “Damage Prediction in Cross-Plied Curved Composite Laminates”, *ASTM Spec. Tech. Publ.*, no. 1156, pp. 105–126, 1993.
- [30] L. Figiel and M. Kaminski, “Mechanical and Thermal Fatigue Delamination of Curved Layered Composites”, *Comput. Struct.*, vol. 81, pp. 1865–1873, 2003.
- [31] J. P. Blanchfield and G. Allegri, “Delamination Initiation due to Interlaminar Tension in Fibre Reinforced Plastics”, 19th Int. Conf. Compos. Mater., pp. 1–9, 2013.

- [32] W. Cui, T. Liu, J. Len, and R. Ruo, “Interlaminar Tensile Strength (ILTS) Measurement of Woven Glass/Polyester Laminates Using Four-Point Curved Beam Specimen”, Compos. Part A Appl. Sci. Manuf., vol. 27, pp. 1097–1105, 1996.
- [33] A. Harris and O. Orringer, “Investigation of Angle-Ply Delamination Specimen for Interlaminar Strength Test”, J. Compos. Mater., pp. 285–299, 1978.
- [34] J. Bird and R. C. Allen, “The Determination of Interlaminar Tensile Strength of Ship Type Laminates”, 7th Int. Conf. Exp. Stress Anal., 1982.
- [35] P. A. Lagace and D. B. Weems, “A Through the Thickness Strength Specimen for Composites”, Test Methods Des. Allow. Fibrous Compos., vol. 2, pp. 197–207, 1989.
- [36] K. T. Kedward, R. S. Wilson, and S. K. McLean, “Flexure of Simply Curved Composite Shapes”, Composites, vol. 20, no. 6, pp. 527–536, 1989.
- [37] C. C. Hiel, M. Sumich, and D. P. Chappell, “A Curved Beam Test Specimen for Determining the Interlaminar Tensile Strength of a Laminated Composite”, J. Compos. Mater., vol. 25, pp. 854–868, 1991.
- [38] K. N. Shivakumar, H. G. Allen, and V. S. Avva, “Interlaminar Tension Strength of Graphite/Epoxy Composite Laminates”, AIAA J., vol. 32, no. 7, pp. 1478–1484, 1994.
- [39] S. G. Lekhnitskii, “Anisotropic Plates”, p. 477, 1969.
- [40] W. Jackson and R. Martin, “An Interlaminar Tensile Strength Specimen”, Compos. Mater. Test. Des. ASTM STP 1206, vol. 11, pp. 333–354, 1993.
- [41] W. C. Jackson and P. G. Ifju, “Through-the-Thickness Tensile Strength of Textile Composites”, Compos. Mater. Test. Des. ASTM STP 1274, vol. 20, pp. 218–238, 1996.

- [42] R. H. Martin, “Delamination Failure in a Unidirectional Curved Composite Laminate”, *Compos. Mater. Test. Des.*, pp. 365–383, 1992.
- [43] R. M. Jones, “Mechanics of Composite Materials”, 2nd Ed. Taylor & Francis, 1999.
- [44] C. S. Lopes, P. P. Camanho, Z. Gürdal, P. Maimí, and E. V. González, “Low-Velocity Impact Damage on Dispersed Stacking Sequence Laminates. Part II: Numerical simulations”, *Compos. Sci. Technol.*, vol. 69, no. 7–8, pp. 937–947, 2009.
- [45] Hexcel, “HexPly 8552 Prod. Data Sheet”, pp. 1–6, 2016.
- [46] B. Gözlüklü, “Modelling of Intersonic Delamination in Curved-Thick Composite Laminates under Quasi-Static Loading”, Middle East Technical University, 2014.
- [47] A. T. Nettles, “Basic Mechanics of Laminated Composite Plates”, NASA Ref. Publ. 1351, 1994.
- [48] E. Üstün, “Experimental Investigation of Fatigue Behavior of Curved Composite Laminates”, Universitat Politècnica de Catalunya, 2016.
- [49] G. Gu, “A comparative Study of Random Speckle Pattern Simulation Models in Digital Image Correlation”, *Optik*, vol. 126, no. 23, pp. 3713–3716, 2015.
- [50] Gom, ARAMIS v6.1, User Manual, 2009.
- [51] W. Ko and R. Jackson, “Multilayer Theory for Delamination Analysis of a Composite Curved Bar Subjected to End Forces and End Moments”, NASA, Tm-4139. 1989.
- [52] I. Uyar, “Experimental Investigation of Dynamic Delamination in Curved Composite Laminates”, Middle East Technical University, 2014.

- [53] S. W. Tsai and E. M. Wu, “A General Theory of Strength for Anisotropic Materials”, *J. Compos. Mater.*, vol. 5, no. 1, pp. 58–80, 1971.
- [54] Z. Hashin, “Cumulative Damage Theory for Composite Materials: Residual Life and Residual Strength Methods”, *Compos. Sci. Technol.*, vol. 23, no. 1, pp. 1–19, 1985.
- [55] H. Krüger and R. Rolfes, “A Physically Based Fatigue Damage Model for Fibre-Reinforced Plastics under Plane Loading”, *Int. J. Fatigue*, vol. 70, pp. 241–251, 2014.

APPENDIX A

A. BEAM BENDING FEA

To examine the effect of matrix cracking and delamination on stiffness degradation, finite element models are created for straight and curved beams. Exaggerated horizontal (delamination) and vertical (matrix crack) cracks are created on the beams and stiffnesses are calculated and compared.

Straight Beam

Baseline design has the dimensions of 50 m length, 5 m height and 2 m width. The beam is encastre at one end and the 4000 N load is applied in y direction in the other end. Seven different finite element models are analyzed. All models have the same dimensions and the same boundary conditions. The only difference between the models is the crack dimensions and positions. There are horizontal cracks and vertical cracks in different dimensions and the final model consists of two separate beams but the total dimension is also same as the baseline model. All dimension details are tabulated in Table A. 1. From FEA results, stiffness values of the beams are calculated and compared with each other.

In Figure A. 1, it is observed that horizontal cracks leads to significant stiffness reductions while the vertical crack almost not affect the stiffness.

Table A. 1 Details of FEA analysis.

Name	Details	Drawing	δ (mm) (FEA)	Stiffness (N/mm) (FEA)
Baseline	Length=50m Height=5m Width=2m		0.122	32.8
Vertical cracks (size 0.5x2.5m)	3 vertical cracks		0.126	31.7
	3 vertical cracks near the center		0.125	32.0
	9 vertical cracks		0.130	30.8
Horizontal cracks	3 cracks each (5x0.5m)		0.122	32.8
	1 crack at the center (20x0.5m)		0.132	30.3
	1 Long crack at the center (45x0.2m)		0.209	19.13
Two separate beams	2x(Height=2.5m)		0.521	3.84

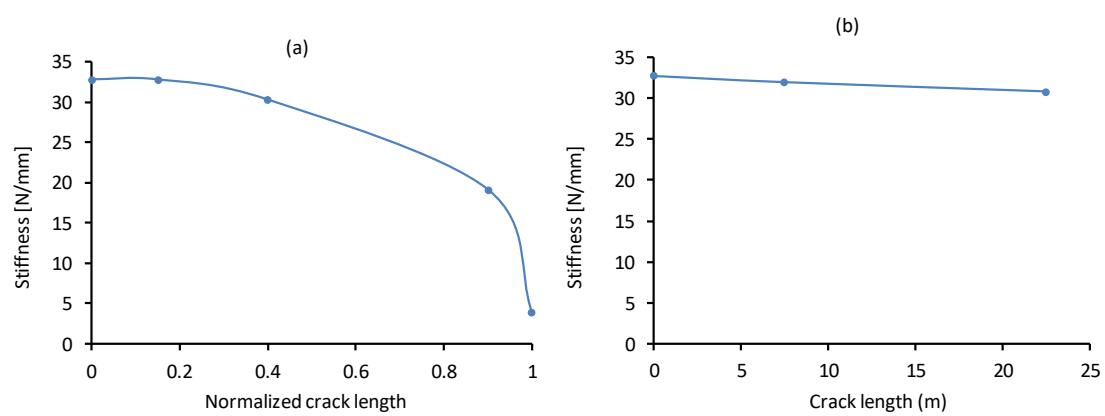


Figure A. 1. Change in stiffness for (a) horizontal and (b) vertical crack cases

Curved Beam

Baseline design has the dimensions of 90mm arm lengths, 5 mm curve inner radius, 5mm thickness and 25 mm width. The beam is fixed at the lower arm in the 40mm length region and 1000 N/mm² pressure is applied to 5mm length region at the upper arm 40mm away from the edge as seen in Figure A. 2. One more boundary condition is also applied at the lower surface of the load region. At this area displacement at y direction is equated to zero.

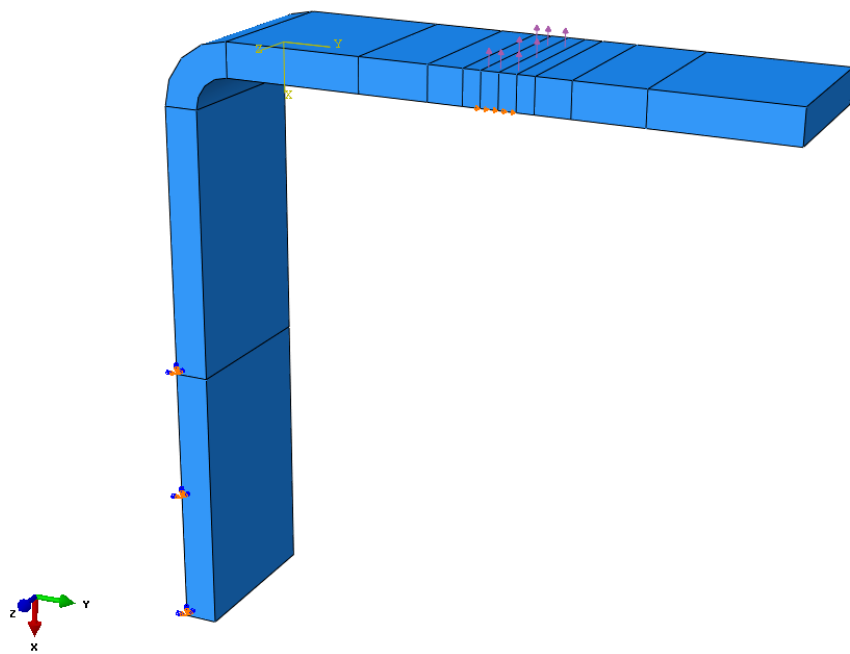


Figure A. 2. Boundary conditions of L-beam model.

Seven different finite element models are analyzed. All models have the same dimensions and boundary conditions. The only difference between the models is the crack dimensions and positions. There are horizontal cracks and vertical cracks in different dimensions. All dimensions details are tabulated in Table A. 2.

In Figure A. 3, it is observed that horizontal cracks leads to significant stiffness reductions while the vertical crack almost not affect the stiffness as in straight beam case. This explains that, delamination failure leads to a significant load drop while matrix cracks do not lead to any load drop.

Table A. 2. Details of L-beam FEA modelling.

Name	Details	Drawing	δ (mm) (FEA)	Stiffness (N/mm) (FEA)
Baseline	Arm lengths=90mm Curve radius=5mm Thickness=5mm Width=25mm		934.19	133.81
Vertical cracks (size 0.2x2mm)	1 vertical crack		975.59	128.13
	3 vertical cracks		983.60	127.08
	5 vertical cracks		993.77	125.78
Horizontal cracks (thickness 0.2mm)	30 degree		952.32	131.26
	60 degree		1063.92	117.49
	90 degree		1325.78	94.28
	90degree+20mm		3552.13	35.19

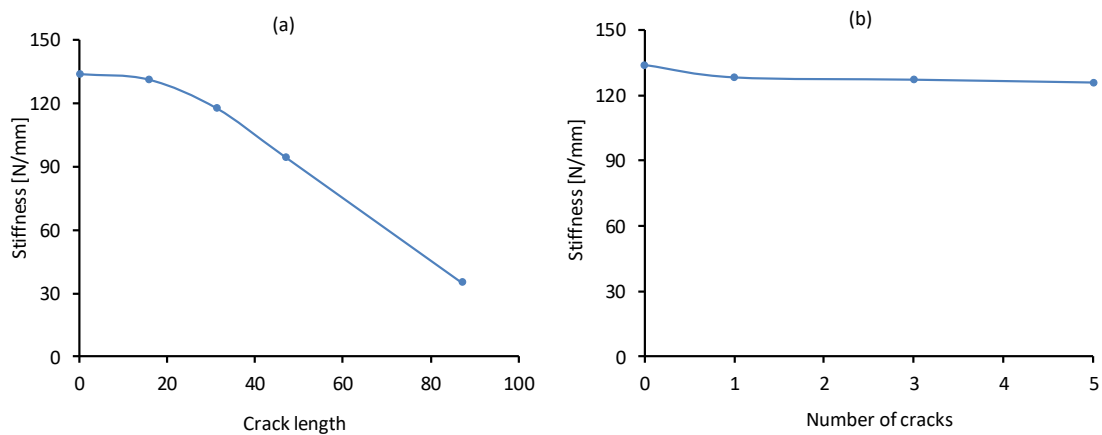


Figure A. 3. Change in stiffness plots for horizontal and vertical crack cases.

APPENDIX B

B. TSAI-WU FAILURE CRITERIA

Tsai-Wu failure criterion, a quadratic stress-based criterion that identifies failure, employs the following failure function for orthotropic materials in their material axes [53]:

$$FI = F_1\sigma_{11} + F_2\sigma_{22} + F_3\sigma_{33} + F_{11}\sigma_{11}^2 + F_{22}\sigma_{22}^2 + F_{33}\sigma_{33}^2 + 2F_{12}\sigma_{11}\sigma_{22} \\ + 2F_{13}\sigma_{11}\sigma_{33} + 2F_{23}\sigma_{22}\sigma_{33} + F_{44}\sigma_{23}^2 + F_{55}\sigma_{13}^2 + F_{66}\sigma_{12}^2$$

For transversely anisotropic UD composites following assumptions are usually used due to random distribution of fibers in the cross-section.

$$F_{33} = F_{22}, \quad F_{13} = F_{12}, \quad F_3 = F_2, \quad F_{55} = F_{66}$$

The Tsai-Wu failure criterion can be reduced to following form:

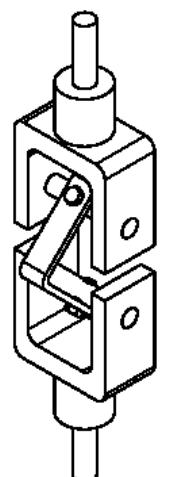
$$FI = F_{11}\sigma_{11}^2 + F_{22}(\sigma_{22}^2 + \sigma_{33}^2) + (2F_{22} - F_{44})\sigma_{22}\sigma_{33} + 2F_{12}\sigma_{11}(\sigma_{33} + \sigma_{22}) \\ + F_1\sigma_{11} + F_2(\sigma_{22} + \sigma_{33}) + F_{44}\sigma_{23}^2 + F_{66}(\sigma_{13}^2 + \sigma_{12}^2)$$

where; FI is the failure index and:

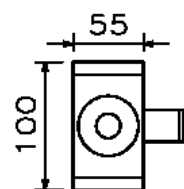
$$F_1 = \frac{1}{S_{11}^t} + \frac{1}{S_{11}^c} \quad F_2 = \frac{1}{S_{22}^t} + \frac{1}{S_{22}^c} \\ F_{11} = -\frac{1}{S_{11}^t S_{11}^c} \quad F_{22} = -\frac{1}{S_{22}^t S_{22}^c} \\ F_{44} = \frac{1}{S_{23}^2} \quad F_{66} = \frac{1}{S_{12}^2} \\ F_{12} = \frac{1}{2} \sqrt{F_{11}F_{22}}$$

APPENDIX C

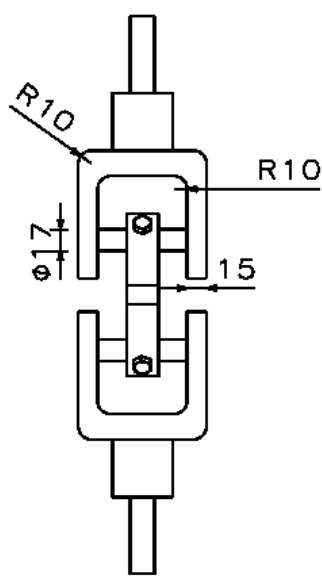
C. TECHNICAL DRAWING OF THE TEST FIXTURE



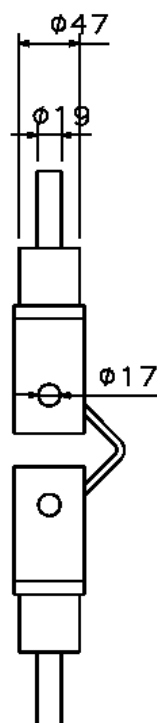
Isometric view
Scale: 1:4



Bottom view
Scale: 1:4



Right view
Scale: 1:4



Front view
Scale: 1:4

APPENDIX D

D. USED MACHINES AND FUNCTIONS

MTS 250 kN Fatigue/Static Axial Test Machine

Machine

Specifications

- Servo-hydraulic Static/Fatigue Testing Machine (30 Hz)
- Tension-Compression Static/Fatigue
- Brand: MTS
- Capacity: 250 kN
- Operating Temperature: -40 – 177 °C
- Axial testing machine is used for tension-compression static and fatigue testing in coupon and component level.



Figure D. 1. MTS 250 kN fatigue/static axial test machine.

HUVITZ HDS-5800 Digital

Microscope

Specifications

- Optical Magnification
0.89x-103.111x
- Total Magnification 50x-5800x
- Field view 9.9mm-0.085mm
- Working Distance 100mm

Applications:

- Surface inspection of the specimen before the test to avoid initial failure.
- Evaluation of surface fractures of the specimen after the test.

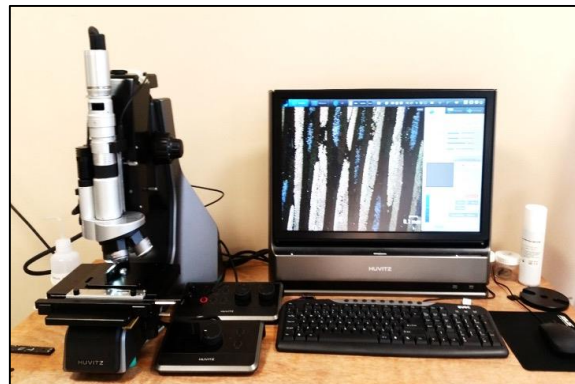


Figure D. 2. HUVITZ HDS-5800 digital microscope.

Digital Image Correlation (DIC) System

GOM-Aramis/Pontos

Specifications

- 3D imaging and measurement
- 4MP resolution
- Up to 480 fps imaging

Applications:

- Component testing and analysis
- Surface strain measurement
- Measurement of 3D displacements

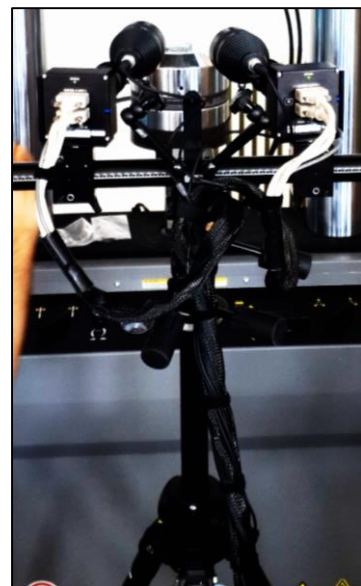


Figure D. 3. Digital Image Correlation (DIC) system GOM-Aramis/Pontos

High Speed Imaging System PHOTRON SA-5X

Specifications

- 7,000- 1,000,000 fps imaging
- Full 1,024 H x 1,024 V (1MP) pixel resolution at 7,000 frames per second (fps)
- Reduced resolution to 1,000,000 fps
- 20-50-100 mm camera lenses

Applications:

- High speed crack growth imaging of components
- High speed strain observations

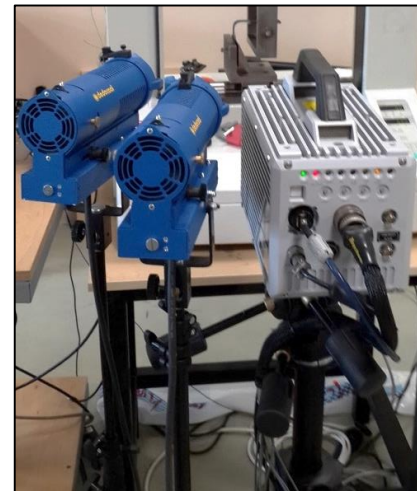


Figure D. 4. High speed imaging system PHOTRON SA-5X.

PRESI Minitech 233 Grinding and Polishing Machine

Specifications

- Platens 200 or 250mm
- 1 polishing station
- Weight 52 kg

Applications:

- Polishing of the specimen side surface to provide clear micrographs.



Figure D. 5. PRESI Minitech 233 grinding and polishing machine.

Digital Thermometer 8808 Temp.& RH%

Logger-LCD

Specifications

- Temperature measurement
- IAQ (Indoor Air Quality) monitoring and control

Applications:

- Temperature changes are observed during long fatigue experiments



Figure D. 6. Digital thermometer 8808 Temp.& RH% Logger-LCD

Checkline DTW-1200i Electronic

Torque Wrench

Specifications

- Capacity 1200 in-lb / 145 N-m,
- Drive Size 3/8 in

Applications:

- Specimen mounting to fixture at a fix torque



Figure D. 7. Checkline DTW-1200i electronic torque wrench.